**Title**
Upper ocean processes observed by underwater gliders in the California Current System

**Author**
Todd, Robert E.

**Publication Date**
2011

UNIVERSITY OF CALIFORNIA, SAN DIEGO

# Upper ocean processes observed by underwater gliders in the California Current System

A dissertation submitted in partial satisfaction of the
requirements for the degree
Doctor of Philosophy

in

Oceanography

by

Robert E. Todd

Committee in charge:

Daniel L. Rudnick, Chair
Bruce D. Cornuelle
Peter J. S. Franks
Stefan G. Llewellyn Smith
Clinton D. Winant

2011

The dissertation of Robert E. Todd is approved, and it is acceptable in quality and form for publication on microfilm and electronically:

Chair

University of California, San Diego

2011

# EPIGRAPH

*Sail away from the safe harbor.*
*Catch the trade winds in your sails.*
*Explore.*
*Dream.*
*Discover.*
—Mark Twain

## TABLE OF CONTENTS

## LIST OF FIGURES

# LIST OF TABLES

# ACKNOWLEDGEMENTS

I have been fortunate to have an excellent advisor in Dan Rudnick. He has let me follow my own interests along the way without letting me wander too far from a productive path. With his help I have learned the intricacies of data processing and analysis, become a better writer, and gained insights into the workings of the scientific world.

I would like to thank my other committee members, Bruce Cornuelle, Peter Franks, Stefan Llewellyn Smith, and Clint Winant, for their help along the way. Bruce was particularly helpful as I delved into the world of numerical modeling for the work in Chapters 3 and 5.

None of the work I have done would have been possible without the work by Russ Davis, Jeff Sherman, Brent Jones, David Black, Kyle Grindley, David Manley, and the rest of the Instrument Development Group at SIO. They designed, built, and operated the Spray gliders that were the primary observational tool used in this dissertation. Matt Mazloff setup and ran the numerical simulation that I used in Chapters 3 and 5, and he graciously let me be the first to use it.

I have made many great friends at SIO. Ben Reineman has been a great officemate and friend for the last four and a half years. Peter Sutherland was my roommate for two and half years. Along with Lisa Munger, Anaïs Orsi, Dian Putrasahan, Marc and Lauren Rafelski, Yvonne Firing, Gordy Stephenson, and others, they have made my time at SIO particularly fun.

My parents have always supported me, and for that I am thankful. They've been there for me through something like 22 years of school. With the submission of this dissertation, I think I can finally tell them that I'm done with school, but saying that I'm off to get a job in the 'real world' might be a stretch.

I was lucky enough to meet my wife, Sylvia, at SIO. She always makes me smile.

This work was funded by the California Coastal Conservancy's Coastal Ocean Current Mapping Program (COCMP), the Gordon and Betty Moore Foundation, NSF through the California Current Ecosystem LTER site, and NOAA

through the Consortium on the Ocean's Role in Climate (CORC) and the Southern California Coastal Ocean Observing System (SCCOOS). I was also supported by a National Defense Science and Engineering Graduate (NDSEG) Fellowship funded by the Office of Naval Research; a UCSD Chancellor's Fellowship; an Achievement Rewards for College Scientists (ARCS), Los Angeles Chapter, scholarship; and a Phi Kappa Phi Graduate Fellowship.

Chapter 2, in full, is a reproduction of the material as it appears in *Todd, Rudnick, and Davis* [2009], *J. Geophys. Res., 114*, C06001. The dissertation author was the primary investigator and author of this work. I thank the American Geophysical Union for granting permission to include it in this dissertation.

Chapter 3, in full, is a reproduction of the material as it appears in *Todd, Rudnick, Mazloff, Davis, and Cornuelle* [2011a], *J. Geophys. Res., 116*, C02026. The dissertation author was the primary investigator and author of this work. I thank the American Geophysical Union for granting permission to include it in this dissertation.

Chapter 4, in full, is a reproduction of the material as it appears *Todd, Rudnick, Davis, and Ohman* [2011b], *Geophys. Res. Lett., 38*, L03609. The dissertation author was the primary investigator and author of this work. I thank the American Geophysical Union for granting permission to include it in this dissertation.

Chapter 5 is currently being prepared for submission for publication of the material. Todd, Robert E.; Rudnick, Daniel L.; Mazloff, Matthew R.; Cornuelle, Bruce D.; Davis, Russ E. The dissertation author was the primary investigator and author of this material.

# VITA

| | |
|---|---|
| 2005 | B.S. in Marine Science, Physics, and Applied Mathematics<br>*Summa cum laude*<br>North Carolina State University |
| 2005–2011 | Graduate Student Researcher<br>Scripps Institution of Oceanography<br>University of California, San Diego |
| 2006 | M.S. in Oceanography, University of California, San Diego |
| 2011 | Ph.D. in Oceanography, University of California, San Diego |

# PUBLICATIONS

Johnston, T. M. S., D. L. Rudnick, G. S. Carter, R. E. Todd, and S. T. Cole (2011), Internal tidal beams and mixing near Monterey Bay, *J. Geophys. Res., 116*, C03017, doi:10.1029/2010JC006592.

Todd, R. E., D. L. Rudnick, M. R. Mazloff, R. E. Davis, and B. D. Cornuelle (2011), Poleward flows in the southern California Current System: Glider observations and numerical simulation, *J. Geophys. Res., 116*, C02026, doi:10.1029/2010JC006536.

Todd, R. E., D. L. Rudnick, R. E. Davis, and M. D. Ohman (2011), Underwater gliders reveal rapid arrival of El Niño effects off California's coast, *Geophys. Res. Lett., 38*, L03609, doi:10.1029/2010GL046376.

Todd, R. E., D. L. Rudnick, and R. E. Davis (2009), Monitoring the greater San Pedro Bay region using autonomous underwater gliders during fall of 2006, *J. Geophys. Res., 114*, C06001, doi:10.1029/2008JC005086.

# FIELDS OF STUDY

Major Field: Physical Oceanography

Studies in Descriptive Physical Oceanography
Professor D. H. Roemmich

Studies in Data Analysis
Professors S. T. Gille, R. Pinkel, and D. L. Rudnick

Studies in Fluid Dynamics and Turbulence
Professors S. Sarkar and C. D. Winant

Studies in Geophysical Fluid Dynamics
Professors P. Cessi and R. Salmon

Studies in Linear and Nonlinear Waves
Professors R. T. Guza, M. C. Hendershott, and W. K. Melville

Studies in Applied Mathematics
Professors G. R. Ierley, D. M. Tartakovsky, and W. R. Young

Studies in Biological Oceanography
Professor P. J. S. Franks

Studies in Oceanographic Instrumentation
Professor U. Send

ABSTRACT OF THE DISSERTATION

# Upper ocean processes observed by underwater gliders in the California Current System

by

Robert E. Todd

Doctor of Philosophy in Oceanography

University of California, San Diego, 2011

Daniel L. Rudnick, Chair

Spray glider surveys in the California Current System (CCS) resolve upper ocean processes at scales from a few kilometers to a few hundred kilometers over monthly to interannual timescales. These observations are used to understand eddies and effluent transport, the structure and variability of poleward currents, the regional effects of El Niño, and thermohaline structure.

Repeated glider surveys of the greater San Pedro Bay region within the Southern California Bight (SCB) are used to describe coastal processes during the fall of 2006. Elevated subsurface chlorophyll levels within a small cyclonic eddy correspond to an inferred increase in nitrate availability to the euphotic zone. The low-salinity signature of the effluent plume from a coastal ocean outfall is used to show that the plume was advected poleward while remaining subsurface.

Glider observations and a numerical state estimate are used to describe the mean and variability of poleward flows in the CCS. Persistent poleward currents are observed near Point Conception, within the SCB, and offshore of the SCB. The poleward current offshore of the SCB migrates westward with across-shore wave number and frequency that are consistent with first-mode baroclinic Rossby dynamics. This westward propagation is tied to westward propagating density anomalies originating in the SCB during the spring-summer upwelling season.

The effects of the 2009–2010 El Niño in the CCS are investigated using glider observations. Positive upper ocean temperature anomalies and depression of isopycnals coincide with equatorial SST anomalies, while isopycnal salinity and alongshore transport anomalies are shown to be insignificant. Glider observations rule out advection of subtropical waters into the CCS during the 2009–2010 El Niño and suggest that an atmospheric teleconnection was important.

Glider observations show the distribution of temperature and salinity variations along isopycnals at mesoscales and submesoscales. Along-isopycnal salinity variance is used to identify distinct layers; increased variance is found in the seasonally restratifying layer and within a layer below the thermocline. Adjoint passive tracer calculations in a numerical state estimate show the differing histories of waters in each layer.

# Chapter 1

# Introduction

This dissertation examines upper ocean processes occurring in the California Current System (CCS) across a range of spatial and temporal scales. Chapter 2 focuses on the greater San Pedro Bay region adjacent to the coast of Southern California during the fall of 2006 and shows the biological significance of a small cyclonic eddy and the spreading of a subsurface effluent plume in the coastal ocean. Chapter 3 analyzes the mean and variability of poleward currents in the CCS. Chapter 4 describes the effects of the 2009–2010 El Niño event in the CCS and the possible mechanisms by which an equatorial event can affect the midlatitude CCS. Finally, Chapter 5 examines the thermohaline structure of the CCS and uses that structure to further understand the circulation of the CCS. Each chapter relies on upper ocean observations collected by autonomous underwater gliders, and Chapters 3 and 5 also make use of a numerical state estimate.

In the midlatitude oceans, basin-scale winds drive anticyclonic gyre circulation with poleward flow on the western sides of the basins and equatorward flow on the eastern sides of the basins. The poleward increase in the Coriolis parameter (the $\beta$ effect) leads to strong, narrow currents on the western boundaries (e.g., the Gulf Stream and Kuroshio). The return flow along the eastern margins is often characterized as broad and slow, but localized forcing along eastern boundaries leads to complex systems of equatorward and poleward currents that are referred to as eastern boundary current systems. The midlatitude eastern boundary current systems typically experience wind-driven upwelling, which brings nutrients to the surface and supports highly productive ecosystems.

Located offshore of the U.S. West Coast, the CCS is the eastern boundary current system of the midlatitude North Pacific. The surface-intensified California Current is the principal equatorward flow, while several surface and subsurface poleward flows are found in the region [*Hickey*, 1979; *Lynn and Simpson*, 1987]. Winds in the CCS typically blow equatorward along the coast, so Ekman transport moves water away from the coast and upwells nutrient-rich waters along the coast. Wind speed generally increases away from the coast, and the resulting positive wind stress curl leads to upwelling farther from the coast. This upwelling supports a highly productive marine ecosystem [*Botsford et al.*, 2006; *Rykaczewski and Checkley*, 2008] that has been the focus of the California Cooperative Oceanic Fisheries Investigations (CalCOFI) and, more recently, the California Current Ecosystem Long Term Ecological Research (CCE LTER) program. Small-scale features such as eddies, fronts, and squirts [*Davis*, 1985a] add rich structure at scales from a few kilometers to hundreds of kilometers and influence the marine ecosystem by transporting nutrients and organisms. Complex bathymetry in the Southern California Bight (SCB) has important effects on the local circulation [*Lynn and Simpson*, 1990]. Thorough understanding of the physical processes occurring across a range of scales is key to deciphering ecosystem dynamics in the region.

For decades, ship-based observations have provided the majority of our insight into the physical processes occurring in the CCS [e.g., *Sverdrup and Fleming*, 1941; *Hickey*, 1979; *Lynn and Simpson*, 1987; *Bograd et al.*, 2001], with the CalCOFI program being the longest routine monitoring program. Though working from research ships allows measurements of virtually any oceanic parameter, cost and personnel considerations restrict the amount of time ships can spend surveying the CCS. For instance, CalCOFI manages quarterly surveys along several across-shore transects in the southern portion of the CCS, but quarterly surveys are insufficient to capture the shorter timescales of many processes. Observations from drifters and moorings [e.g., *Davis*, 1985a,b; *Bray et al.*, 1999; *Dever and Winant*, 2002] capture some of the processes occurring at short time scales, but have typically lacked broad spatial coverage in the CCS.

In recent years, autonomous underwater gliders [*Davis et al.*, 2002; *Rudnick et al.*, 2004] have proven to be exceptional platforms for routine monitoring of the coastal ocean. These small (roughly 2 m in length and weighing about 50 kg) devices use changes in buoyancy to ascend and descend through the upper ocean while moving forward by pitching the nose upward during ascent and downwards during decent, much like an aerial glider. With horizontal speeds of around 0.25 m $s^{-1}$ (about 0.5 kt) and the ability to control their direction, gliders are able to navigate to prescribed waypoints, even in the presence of oceanic currents. Individual deployments typically last several months.

The studies of the CCS in this dissertation rely on observations collected by Spray gliders (Figure 1.1), the type of autonomous underwater glider developed at the Scripps Institution of Oceanography [*Sherman et al.*, 2001]. For deployments in the CCS, gliders are equipped with a conductivity-temperature-depth (CTD) sensor, an acoustic Doppler profiler (ADP), and a chlorophyll *a* fluorometer. With that instrument load, battery life allows each glider to remain at sea for 3–4 months while profiling to a maximum depth of 500 m with spatial resolution of about 3 km and temporal resolution of about 3 h. With the exception of two deployments along the coast that are used in Chapter 2, all glider deployments used herein follow existing CalCOFI survey lines with transects repeated roughly every three weeks.

In addition to glider observations, the analyses in Chapters 3 and 5 use a regional numerical state estimate [*Wunsch*, 2006; *Wunsch and Heimbach*, 2007] to understand processes occurring in the CCS. The state estimate is a numerical simulation for which initial conditions, boundary conditions, and forcing have been adjusted so that the simulated ocean state matches a variety of observations, including the glider observations. The state estimate provides dynamically consistent estimates of all oceanic parameters, both observed and unobserved, throughout the CCS and over a 2.6 year period that can be used to diagnose dynamics that are not resolved by observations. The adjoint to the numerical model [*Errico*, 1997; *Heimbach et al.*, 2005], which is used to optimize the initial conditions, boundary conditions, and forcing, can also be used to analyze the backward-in-time sensitivity of chosen metrics of the model state to any other modeled variables [e.g., *Fukumori et al.*, 2004; *Moore et al.*, 2009; *Veneziani et al.*, 2009]. In Chapter 5, the adjoint model is used to investigate past distributions of tagged waters.

Chapter 2 is an investigation of processes occurring in the San Pedro Bay region between the Los Angeles and Orange County coasts and Santa Catalina Island. Like most of the SCB, this area area has complex bathymetry that influences the flow in the region. Due to its proximity to the large populations of Southern California, the San Pedro Bay region also has significant anthropogenic inputs. Along the San Pedro Shelf, the effluent plume from an ocean outfall is tracked as it is advected poleward along an isopycnal by bathymetry-following currents. Repeated surveys of a small cyclonic eddy near the upstream end of Santa Catalina Island show how the eddy increased nutrient content in the euphotic zone, leading to elevated phytoplankton abundance.

Poleward currents in the CCS transport nutrient-rich water of southern origin into the region [*Lynn and Simpson*, 1987] and provide a potential route for planktonic organisms to return to higher latitudes if carried equatorward by the California Current. Chapter 3 examines the mean and variability of poleward currents in the CCS. Repeated sampling allows the persistence of poleward flows to be addressed, as well as their relationship to upwelling events. The common assumption of zero flow at 500 m is also tested.

The CCS is not isolated from physical processes occurring in other parts of the ocean; several modes of interannual variability are known to affect the physical and ecological state of CCS including El Niño [*Bograd et al.*, 2001; *Lynn and Bograd*, 2002], the Pacific Decadal Oscillation [*Chhak and Di Lorenzo*, 2007], and secular trends due to climate change [*Roemmich and McGowan*, 1995]. The four-year observational record from gliders in the CCS is not yet long enough to resolve decadal and longer-term trends, but the observations do capture the 2009–2010 El Niño event and its effect on the CCS. Chapter 4 examines the anomalous conditions in the CCS during the 2009–2010 event and considers mechanisms by which an equatorial El Niño event affected the midlatitude CCS. The ability of gliders to provide a continuous observing presence with transects repeated every few weeks makes them ideal platforms for observing the regional effects of El Niño and other modes of climate variability.

In the CCS, several water masses that each have distinct properties meet [*Lynn and Simpson*, 1987]. Stirring by the velocity field amplifies gradients of water properties by straining [see *Hodges and Rudnick*, 2006] while mixing works to destroy gradients. Along-isopycnal fluctuations in temperature and salinity, which vary from warm and salty to cold and fresh and are referred to as spice [*Munk*, 1981], are the end product of stirring and mixing over the history of a water mass, and can be treated as a passive tracer provided by nature. Chapter 5 uses glider observations of spice in the CCS to identify along-isopycnal layers with distinct spice characteristics. Passive tracers in the numerical state estimate are then used to investigate the past distributions of water in the observed layers.

**Figure 1.1**: A Spray glider on the surface before recovery.

# Chapter 2

# Monitoring the greater San Pedro Bay region using autonomous underwater gliders during fall of 2006

Robert E. Todd, Daniel L. Rudnick, and Russ E. Davis

**Abstract.** Glider surveys of the greater San Pedro Bay region in the Southern California Bight during the fall of 2006 demonstrated the utility of autonomous underwater gliders in a coastal region with complex flow and significant anthropogenic inputs. Three Spray gliders repeatedly surveyed between Santa Catalina Island and the coast of Southern California collecting profiles of temperature, salinity, and chlorophyll fluorescence and estimates of vertically averaged currents. These observations provided context for shelf transport studies during the Huntington Beach 2006 experiment and showed the transition from summer to winter conditions. Vertically averaged currents were predominantly poleward following topography with horizontal scales of approximately 20 km. The gliders surveyed a small cyclonic eddy near Santa Catalina Island and provided a unique view of the structure of the eddy. Nitrate concentration within the euphotic zone was estimated to be 19% greater within the eddy and led to significantly elevated chlorophyll concentrations at the subsurface maximum. Glider observations of

salinity reliably detected the distinctly fresh signature of the effluent plume from an ocean outfall near Huntington Beach, California. The salinity anomaly caused by the plume was used to track the spread of the plume as it was advected poleward and away from the coast while remaining subsurface.

## 2.1 Introduction

The Southern California Bight is notable for its eddy-rich circulation and for being adjacent to a highly developed coastal region. Complex bathymetry and offshore islands further complicate flow within the bight, and proximity to urban centers leads to substantial anthropogenic input into the coastal ocean from sources such as ocean outfalls. The purpose of this study is to demonstrate the utility of autonomous underwater gliders in such a region. Using glider surveys within the greater San Pedro Bay region of the Southern California Bight during the second half of 2006, we show the physical and biological properties of a small eddy and track the effluent plume from a large ocean outfall. Glider observations provide a unique view of the three-dimensional structure of the eddy. The freshwater signature of the effluent plume is useful for tracking its spread and can be detected reliably by glider salinity measurements.

The greater San Pedro Bay (SPB) region includes the San Pedro Shelf off of Orange County and southern Los Angeles County and the relatively deep San Pedro Basin between the shelf and Santa Catalina Island (Figure 2.1). Flow within SPB is usually poleward except in spring [*Lynn and Simpson*, 1987] and generally follows the bathymetry [*Hickey*, 1992]. Circulation and temperature distributions within SPB have been observed from mooring arrays, but there is a significant lack of salinity measurements in the region. *Lynn and Simpson* [1987] used CalCOFI data to characterize the seasonal variability of temperature, salinity, and currents within the California Current System, but only three CalCOFI stations (90.28, 90.30, and 90.35) fall within SPB.

Small eddies are common within SPB and throughout the Southern California Bight. Remote sensing of the ocean surface using synthetic aperture radar reveals numerous eddies smaller than 50 km in diameter that are predominately cyclonic [*DiGiacomo and Holt*, 2001]. Modeling studies suggest that eddies within SPB are largely the result of alongshore flow impinging upon Santa Catalina Island [*Dong and McWilliams*, 2007]. Despite the ubiquity of these small eddies, in situ observations of their vertical structure have not been presented. Autonomous underwater gliders are well suited to collect these observations because of their ability to collect vertical profiles with horizontal spacing of a few kilometers or less and temporal resolution of a few hours.

The Orange County Sanitation District (OCSD) discharges on the order of $1 \times 10^6$ m$^3$ d$^{-1}$ of treated wastewater through an outfall diffuser on the San Pedro Shelf off Huntington Beach, California [*Boehm et al.*, 2002; *OCSD*, 2007]. The 3 m diameter outfall pipe extends 7.5 km offshore and discharges wastewater along the 60 m isobath (Figure 2.1) through a series of diffuser ports that are designed to dilute effluent by at least 100 fold upon initial release [*Wu et al.*, 1994; *Boehm et al.*, 2002]. Several previous studies have focused on the effluent plume from the OCSD outfall. No studies have shown the outfall to be a source of contamination to Orange County beaches, but tidal or diurnal processes may lead to cross-shelf transport of diluted effluent that could bring it to the surface near shore [*Boehm et al.*, 2002; *Hamilton et al.*, 2004]. Autonomous gliders have the potential to provide spatially and temporally broad monitoring of the fate of the effluent plume if it can be reliably identified using available glider data.

Some of the glider observations used here were collected as part of the Huntington Beach 2006 (HB06) experiment. The intensive field campaign during HB06 was designed to measure processes that transport and disperse sediment, biota, and contaminants in the nearshore ocean. HB06 focused on the San Pedro Shelf near Huntington Beach, California during October 2006 (HB06 Website, http://www.sccoos.org/projects/hb06).

This paper focuses on the observations collected by Spray gliders in SPB during the fall of 2006. The spatial and temporal coverage of the gliders allows us to characterize the oceanographic conditions throughout SPB and provide a regional context for the smaller region of immediate focus during HB06. Glider measurements of salinity reveal structure not previously discussed in this region, and salinity proves to be a reliable tracer for oceanic discharge. The remainder of this paper is organized as follows: section 2.2 describes the Spray glider deployments and other observations used in this analysis; section 2.3.1 describes the physical and biological state of SPB and the transition from summer to winter conditions; section 2.3.2 presents observations of a small cyclonic eddy and an estimate of the nutrient flux to the euphotic zone in that eddy; section 2.3.3 describes the identification and tracking of the effluent plume from the OCSD outfall using salinity anomalies; and section 2.4 summarizes the results. Three appendices detail the correction of fluorescence measurements, calculation of current estimates from glider data, and comparisons between glider and mooring measurements.

## 2.2 Data and Methods

We primarily use data from three Spray gliders [*Sherman et al.*, 2001; *Davis et al.*, 2002; *Rudnick et al.*, 2004] deployed in SPB during the fall of 2006. We supplement those data with mooring data over the San Pedro Shelf and CalCOFI station data. The Spray deployments are described in section 2.2.1, and the mooring and CalCOFI data are described in section 2.2.2.

### 2.2.1 Glider Deployments

Spray gliders are buoyancy-powered autonomous underwater vehicles that, in this application, profiled from the surface to 500 m with horizontal resolution of approximately 3 km [*Sherman et al.*, 2001]. Two Spray gliders were deployed in SPB as part of the HB06 experiment. Just before recovery of the two HB06 gliders, a third glider was deployed along CalCOFI Line 90. The two HB06 gliders were deployed near Dana Point, California on 23 September 2006 and recovered near the same location on 20-21 October 2006, and the Line 90 (L90) glider was deployed from Dana Point on 19 October 2006 and recovered on 19 January 2007. All three gliders measured temperature, salinity, density, chlorophyll fluorescence, and acoustic backscatter at 750 kHz. We corrected chlorophyll fluorescence data and calculated current estimates as detailed in the appendices. Deployment statistics are given in Table 2.1.

One of the HB06 gliders (referred to as the San Pedro Shelf (SPS) glider) completed four circuits of a survey pattern over the San Pedro Shelf in the vicinity of the OCSD ocean outfall, southward along the coast and along the inshore edge of the San Pedro Channel (Figure 2.1). Most of the 716 profiles collected by the

SPS glider were in water shallower than 100 m, but the glider made dives to 500 m when in deep water. In many cases, several shallow profiles were completed without the glider surfacing to obtain a GPS fix. Consequently, the times and locations of some profiles were interpolated, and there were fewer estimates of vertically averaged velocity than profiles from the SPS glider. Due to the shallow profiles, horizontal (temporal) resolution was highest for the SPS glider (Table 2.1).

The second HB06 glider (referred to as the Santa Catalina Island (SCI) glider) surveyed primarily over the San Pedro Basin just inshore of Santa Catalina Island (Figure 2.1). The glider completed four sections along a zig-zag pattern near Santa Catalina Island, as well as two complete crossings of the San Pedro Channel and several sections along the southeastern segment of the SPS glider's survey pattern. The SCI glider completed 289 profiles, most of which were to near 500 m depth. The glider was generally kept clear of the shipping lane to avoid collisions with vessels during surface intervals; the combined survey patterns of the SCI and SPS gliders covered most of SPB.

The L90 glider completed four surveys along the roughly 500 km length of CalCOFI Line 90 and collected 846 profiles during its three-month deployment. For this analysis we considered only the portions of the L90 glider's surveys while it was within SPB (Figure 2.1). By 23 October, it had progressed offshore of Santa Catalina Island and beyond the area surveyed by the other gliders; it returned to the region between 30 November and 5 December and again from 12-14 January 2007.

### 2.2.2 Mooring Data and CalCOFI Stations

Numerous surface- and bottom-mounted moorings were deployed over the San Pedro Shelf during the fall of 2006 as part of HB06. While the Spray gliders rarely surveyed inshore of the 50-m isobath (Figure 2.1), the mooring observations extended from the 60-m isobath to inshore of the 10-m isobath near Huntington Beach (Figure 2.2). Surface moorings generally contained temperature loggers with 2-10 m vertical resolution throughout the water column and conductivity sensors at selected depths. Velocity profiles were available at some mooring locations from surface- or bottom-mounted RDI ADCPs. Preliminary data from seven moorings (MA - MG) deployed along the OCSD outfall pipe (Figure 2.2) were considered in this analysis, though only data from the MA site are shown. The moorings used here were deployed by OCSD and the United States Geological Survey. The third appendix compares the glider measurements with concurrent mooring measurements of salinity and currents.

Three CalCOFI stations (90.28, 90.30, and 90.35) within SPB were sampled by *R/V Roger Revelle* on 27 October. Cast data from those stations are available online (http://www.calcofi.org/data/CTD/). Station 90.28 was very near the coast in 72 m of water, 90.30 was in the middle of the San Pedro Channel in 617 m of water, and 90.35 was southeast of Santa Catalina Island in 341 m of water (Figure 2.1). We use the downcast profiles of nitrate and potential density from these three stations. A high-resolution profile of nitrate was not available for Station 90.35, so we use nitrate concentrations from bottle samples for that station.

## 2.3 Results and Discussion

### 2.3.1 Regional Conditions

Most of the observational effort during HB06 focused on the inner shelf, and the Spray gliders were the only tools for observing subsurface processes over the greater San Pedro Bay region. The glider observations showed the physical (section 2.3.1.1) and biological (section 2.3.1.2) conditions throughout SPB during HB06 and provided context for the eddy and effluent plume observations of sections 2.3.2 and 2.3.3.

#### 2.3.1.1 Physical Features

Vertically averaged currents were generally northwestward during September and October 2006 (Figure 2.3). The mean vertically averaged current speeds were 0.055 m $s^{-1}$ and 0.050 m $s^{-1}$ during the deployments of SPS and SCI gliders, respectively. These average currents are not directly comparable since vertical averaging occurs over the depth of each glider profile and most dives by the SCI glider were to 500 m depth while the SPS glider made many more shallow dives (Table 2.1). Vertically averaged currents rarely exceeded 0.2 m $s^{-1}$, allowing the gliders to navigate well throughout the survey period.

To estimate the mean circulation in SPB during the concurrent deployments of the SPS and SCI gliders, we objectively mapped the observed vertically averaged currents. We estimated autocorrelations for the east and north components of the vertically averaged velocity using along-track separation so that observations near the same locations but separated by large times were given less weight. These empirical autocorrelations showed an abrupt decrease in correlation at very small scales that we attributed to noise and were otherwise well modeled by a Gaussian with a characteristic scale of 17.6 to 26.2 km. We used a characteristic length scale of 20 km for the objective map. We constrained the mapped vertically averaged currents to be nondivergent and included noise with a noise-to-signal ratio of 0.2. Bathymetry was not explicitly considered in the objective map, but we excluded current measurements from profiles shallower than 50 m and masked the resulting map to exclude areas shallower than 50 m. We also masked mapped currents offshore of Santa Catalina Island where there were no data. The resulting mean flow (Figure 2.3, black vectors) was generally poleward and closely followed the bathymetry [*Hickey*, 1992; *Hickey et al.*, 2003]. In particular, the mean flow turned nearly due west where the San Pedro Shelf widens near Huntington Beach. The cyclonic signature of the eddy southeast of Santa Catalina Island (section 2.3.2) was apparent even in the mean currents.

Glider surveys revealed a subsurface salinity minimum (SSM) as a dominant feature in the region (Figure 2.4). The SSM was a remnant of subarctic water from the core of the California Current that was advected eastward and northward, consistent with the circulation of the Southern California Eddy [*Hickey*, 1979; *Lynn and Simpson*, 1987]. For the average of all profiles by the SCI glider, a minimum salinity of 33.27 psu occurred at a depth of 35 m. The SSM was found near the $\sigma_\theta = 24.4$ kg $m^{-3}$ isopycnal throughout the glider surveys. Over the San Pedro Shelf, isopycnals shoaled noticeably, so the depth of the SSM was less than 25 m. Moored measurements of salinity showed the SSM over the San Pedro Shelf to depths as shallow as 8 m (mooring MG), but the strength of the minimum was somewhat reduced over the inner shelf. Thus it seems that recirculation of California Current waters was predominantly over the deeper parts of SPB.

Repeated glider surveys allowed us to characterize the variability of the SSM within San Pedro Bay. Four repeated surveys of each of the patterns flown by the SPS and SCI gliders provided approximately weekly coverage of those patterns from late September to mid-October while four crossings of the San Pedro Channel by the SCI and L90 gliders provided approximately monthly repetition from late September to mid-January 2007. Changes in position and strength of the SSM were relatively small during the surveys of the SPS and SCI gliders; the SSM strengthened by 0.05 psu in the western part of SPB while it weakened by 0.05 psu along the San Pedro Shelf (Figure 2.4). Monthly surveys across SPB showed that the SSM weakened substantially in late fall. By mid-January, salinity at the SSM increased to 33.45 psu at a depth of 55 m (Figure 2.4). The observed weakening of the SSM may have resulted from reduced recirculation of California Current waters within the Southern California Bight following the summertime intensification of the Southern California Eddy [*Lynn and Simpson*, 1987]. Vertically averaged currents during the latter part of the deployment of the L90 glider were frequently onshore or equatorward (Figure 2.3), consistent with reduced recirculation and diminishment of the SSM.

Overlying the subsurface salinity minimum was a surface mixed layer with thickness generally less than 20 m (13.2 ± 5.3 m for the SCI glider) with the mixed layer thickness defined as a density difference from the surface of 0.1 kg $m^{-3}$ [*Rudnick and Ferrari*, 1999]. *Hickey et al.* [2003] reported a similar mixed layer depth for early fall using moored temperature and current measurements within the Southern California Bight during much of 1988. The repeated surveys of the SPS and SCI gliders showed that the mixed layer cooled by 1.5–2.1 °C and freshened by 0.07–0.1 psu during September and October (Figure 2.4). Cooling and freshening were both greater for the SPS pattern, but surveys of that pattern also took 8 days longer than the offshore SCI pattern. Between the second and third surveys there was more substantial cooling (inshore and offshore surveys) and freshening of the mixed layer (inshore survey). This abrupt change in the mixed layer was coincident with the weakening of the SSM noted above. From late September to early December, the mixed layer cooled a total of 4 °C, but little additional freshening occurred between late October and early December. While cooling continued into early winter, the mixed layer grew saltier and significantly deeper between the final two surveys by the L90 glider (Figure 2.4). The increase in salinity in both the mixed layer and SSM in late fall further suggests a change in horizontal advection rather than vertical exchange. Based on the depth of the mixed layer in mid-January, strong mixing extended from the surface to about 40 m depth. This mixing did not extend below the SSM to deeper saltier water, so saltier water must have been advected horizontally into the region near the surface.

While significant cooling occurred in the mixed layer, the water column warmed below the pycnocline. The warming was particularly evident in the monthly repeats of the San Pedro Channel crossing where temperatures at 100 m were 1.0 °C warmer during the third occupation on 30 November to 5 December than in the preceding surveys and warmed slightly more by mid-January. This warming below the pycnocline is consistent with the results of *Hickey et al.* [2003]. During this warming, water below 100 m first freshened, then grew saltier again by mid-January (Figure 2.4).

#### 2.3.1.2 Subsurface Chlorophyll Maximum and Zooplankton

A subsurface chlorophyll maximum (SCM) was observed throughout the region (Figure 2.4). The SCM was located slightly below, but generally within, the salinity minimum. Throughout the glider surveys, the SCM was found between the 24.5 kg $m^{-3}$ and 25.2 kg $m^{-3}$ isopycnals, though patches of high chlorophyll throughout the mixed layer occurred over the shelf. Like the SSM, the SCM was found shallower over the San Pedro Shelf where associated isopycnals were found closer to the surface (10–30 m over the shelf and 30–50 m over the San Pedro Basin). This shoaling of the SCM over the shelf may have contributed to the slightly enhanced fluorescence in the surveys by the SPS glider close to the San Pedro Shelf (Figure 2.4c).

During the inshore surveys of the SPS glider, the depth of the SCM decreased by 20 m, while the depth of the SCM in the offshore surveys of the SCI glider remained virtually constant during the month of observations. By late November, the SCM over the San Pedro Basin had shoaled by more than 10 m to a depth 25 m. The first and last surveys of the offshore pattern by the SCI glider and the first two surveys across the San Pedro Channel by the SCI and L90 gliders showed elevated chlorophyll fluorescence compared to the other surveys of those regions (Figure 2.4). Portions of those surveys were within a cyclonic eddy that produced locally elevated chlorophyll levels (section 2.3.2).

Acoustic backscatter measurements throughout SPB revealed a strong diel signal with high backscatter just below the mixed layer at night and deeper than 200 m during the day (Figure 2.5 shows a typical section). A similar signal has been noted in other glider surveys in Southern California [*Davis et al.*, 2008] and is attributed to vertically migrating zooplankton feeding in shallow waters at night and retreating to deep water to avoid predation during daylight. Indeed, the observed maximum in backscatter was colocated with the SCM during night, suggesting that the migrating zooplankton were feeding on the abundant phytoplankton within the SCM.

### 2.3.2 Eddy Observations

A small but persistent cyclonic eddy was sampled twice by the SCI glider and a third time by the L90 glider during the beginning of its deployment on CalCOFI Line 90. Vertically averaged currents during three passes of the gliders through the region to the southeast of Santa Catalina Island showed clear cyclonic rotation centered near 33.3°N, 118.1°W (Figure 2.6). The two passes by the SCI glider through this region were the only periods in which southward currents were observed consistently by that glider. The observations were made on 24–26 September, 11–14 October, and 20–22 October. Although it was not possible from the available observations to determine definitively that the three sets of observations were of the same eddy, the collocation of cyclonic currents suggested that this was the case.

If the observed eddy remained stationary for at least one month, then it was somewhat different than most small eddies reported or modeled in the region. The common eddy evolution scenario involves eddies shed from instabilities in island wakes that then propagated downstream [*Caldeira et al.*, 2005; *Dong and McWilliams*, 2007]. Not only did the eddy observed here not propagate, but it was also located near the upstream end of Santa Catalina Island. The proximity to the island and nearby bathymetric features suggests that the presence of Santa Catalina Island was key to the eddy's formation and persistence, but we do not have a dynamic explanation for the eddy based on our observations. *Caldeira et al.* [2005] generated a cyclonic eddy near the same location using the ROMS model, and other authors [*Owen*, 1980; *DiGiacomo and Holt*, 2001] have reported small eddies to the southeast of Santa Catalina Island in the fall, but none have suggested specific formation mechanisms.

Whereas most previous observations of small eddies in this region showed only surface signatures of the eddies [*DiGiacomo and Holt*, 2001], glider observations provided information on both the vertical and horizontal structure of the eddy. Doming isopycnals were evident in each pass through the eddy, with vertical displacements of 15–20 m below the mixed layer over a horizontal scale of 30–50 km (Figure 2.7 is representative of the passes). The doming of these isopycnals generated geostrophic velocities (referenced to the observed vertically averaged currents and smoothed over 10 km) that were consistent with a cyclonic eddy extending to 80-120 m depth (Figure 2.7).

Based on the cyclonic signature in the vertically averaged currents and domed isopycnals, we identified particular dives as being within the eddy. Dives 18–44 and 187–226 of the SCI glider, and dives 16–35 of the L90 glider were selected based on these criteria. We calculated an average chlorophyll profile for each group of dives and compared those with the mean chlorophyll profile for all observations within SPB that were away from the San Pedro Shelf (west of 117.9°W) and not within the eddy. Confidence intervals about these mean profiles were constructed assuming a $t$ distribution and using the means and standard deviations of the groups of profiles. The observations showed chlorophyll concentrations at the SCM within the eddy to be significantly greater (at the 90% significance level) than over the entire region (Figure 2.8). The eddy had little effect on surface chlorophyll concentrations.

Nutrient availability within the euphotic zone is often the limiting factor in phytoplankton abundance. Nitrate is one such nutrient for which measurements are readily available. Shoaling isopycnals are expected to bring increased nutrients into the euphotic zone [*McGillicuddy et al.*, 1998], and to bring isopycnal-following phytoplankton into better illuminated waters where their light-dependent growth rates increase. Both of these effects should stimulate phytoplankton growth and increase phytoplankton abundance.

We estimated the flux of nitrate into the euphotic zone due to the eddy by combining the glider observations with nitrate profiles from CalCOFI Stations 90.28, 90.30, and 90.35 on 27 October. The CalCOFI profiles showed constant low nitrate in the surface layer and nitrate increasing linearly with density below the $\sigma_\theta = 24.7$ kg m$^{-3}$ isopycnal. Unsurprisingly, this level fell very near the observed SCM. *Eppley et al.* [1979] reported a qualitatively similar nutrient profile. Despite the difference in location and bottom depth between the three stations, the profiles agreed well (Figure 2.9), though nitrate levels began to increase at a slightly denser isopycnal at Station 90.35. Using least-squares techniques, we fit a piecewise continuous function to the observed nitrate versus density profiles with a constant value shallower than the $\sigma_\theta = 24.7$ kg m$^{-3}$ isopycnal and a linear function of density below that level. The resulting fit was

$$[\mathrm{NO_3}] = \begin{cases} 0.39, & \sigma_\theta \leq 24.7 \text{ kg m}^{-3}, \\ 16.31\,\sigma_\theta - 402.47, & \sigma_\theta > 24.7 \text{ kg m}^{-3}, \end{cases} \tag{2.1}$$

when the concentration of nitrate, $[\mathrm{NO_3}]$, was measured in $\mu$mol l$^{-1}$.

We calculated nitrate profiles for each of the selected dives using the observed density profiles and (2.1). We created a mean nitrate profile outside of the eddy from the mean density profile from all dives of the SCI glider outside of the eddy and away from the shelf. The nitrate anomaly inside the eddy was defined relative to this mean nitrate profile. Integrating the nitrate anomaly between the surface and 100 m and averaging over all profiles within the eddy gave an estimated nitrate input due to doming isopycnals within the eddy of 0.15 mol m$^{-2}$. Integration over the upper 100 m was chosen to approximate the euphotic zone based on chlorophyll levels. *McGillicuddy et al.* [1998] performed a similar estimate of nitrate input to the euphotic zone for large open ocean eddies moving past a site in the oligotrophic Sargasso Sea. Their estimate of the annual input of nitrate to the euphotic zone was 0.19 mol m$^{-2}$. Located near a nutrient-rich coastal upwelling zone, the eddy near Santa Catalina Island was responsible for a similar nitrate flux over a period of a few months and despite being much smaller. The estimated increase in nitrate within the observed eddy represented more than 19% of the total nitrate in the euphotic zone. The doming isopycnals within the eddy increased nutrient inputs to the euphotic zone and allowed for increased local phytoplankton abundance.

### 2.3.3 Effluent Plume Tracking and Characterization

The survey pattern of the SPS glider took it in the vicinity of the OCSD ocean outfall. *Hamilton et al.* [2004] showed that the effluent plume from the OCSD outfall was characterized by a salinity minimum at temperatures below 14 °C that stood out from the background temperature-salinity profile. Salinity sections near the OCSD outfall showed two distinct salinity minima (Figure 2.10). The shallower of these minima (near the $\sigma_\theta = 24.4$ kg m$^{-3}$ isopycnal) was the shallow salinity minimum discussed above. Near the $\sigma_\theta = 25.0$ kg m$^{-3}$ isopycnal was the salinity anomaly that characterized the effluent plume.

Near the 200 km point along the glider track (Figure 2.10), the salinity minimum that indicated the plume extended at least 0.1 kg m$^{-3}$ deeper than the $\sigma_\theta = 25.0$ kg m$^{-3}$ and beyond the glider's profiling depth. That portion of the glider's track was nearly on top of the OCSD outfall diffuser, so we suspect that this may be observational evidence of the buoyant rise of the effluent plume (cf. *Roberts* [1999]). Examination of individual profiles from that portion of the survey also revealed some small density inversions that may have been due to buoyant water rising from the outfall.

#### 2.3.3.1 Manual Detection

Previous authors [*Jones et al.*, 2002; *Hamilton et al.*, 2004] used salinities below an empirical threshold combined with detectable levels of fecal indicator bacteria to identify the effluent plume from the OCSD outfall. The SPS glider did not measure an independent indicator of the effluent plume, and the proximity of the SSM to the effluent plume made application of a simple threshold salinity unreliable, so we used anomalies in salinity to detect the plume. The variability in vertical structure between profiles over the entire deployment led to ambiguity in identifying the plume based on fixed salinity thresholds [*Wu et al.*, 1994], so we considered profiles individually rather than in bulk as in previous studies [*Jones et al.*, 2002; *Hamilton et al.*, 2004]. We identified any portion of a $\theta$-$S$ profile with (1) a local minimum in salinity, (2) potential temperature less than 14°C, (3) potential density anomaly, $\sigma_\theta$, greater than or equal to 24.6 kg m$^{-3}$, and (4) a deviation from the background $\theta$-$S$ profile that was greater in magnitude than the small-scale variability in the remainder of the profile as indicative of the effluent plume from the OCSD outfall. The profile from dive 90 of the SPS glider (Figure 2.11) showed this anomaly particularly well.

Manual evaluation of these criteria for each of the 716 profiles collected by the SPS glider found that 199 profiles indicated the presence of the effluent plume. Although location of a profile was not a criterion for identifying the effluent plume, nearly all of the dives that showed evidence of the plume were located near the OCSD outfall (Figure 2.12). Only 8 out of the 199 profiles were more than 6 km from the along-isobath portion of the outfall pipe. The proximity of the selected dives to the outfall pipe suggested that the criteria used in detecting the plume were reliable.

#### 2.3.3.2 Automatic Detection

Manual evaluation of the detection criteria given above is tedious and lacks objectivity. To automate the process of plume detection, we developed a filtering method to detect the effluent plume in individual profiles. With this automated method, salinity anomalies remained the primary indicators of the effluent plume.

Profiles were analyzed in potential density space since the effluent plume was observed to follow isopycnals more than isobars. Measured salinity profiles were mapped onto uniformly spaced densities ($\Delta\sigma = 0.01$ kg m$^{-3}$) using linear interpolation. Salinities were intentionally over-sampled by the interpolation to avoid loss of variability in the original signal.

In order to effectively identify salinity anomalies due to the effluent plume, the background profile of salinity with density had to be removed from each measured profile. How to accomplish this was the primary difficulty in developing an automatic detection scheme. Since the distribution of salinity as a function of density was reasonably uniform across SPB, we used all measured profiles by the SCI glider to construct a typical salinity versus density profile that did not include the effects of the effluent plume. We subtracted this typical profile from each individual profile measured by the SPS glider. We then filtered the resulting profiles to accentuate variability at the scales typical of the effluent plume. A band pass filter that admitted variability with scales between 0.15 and 2 kg m$^{-3}$ worked well. Any filtered profile with a salinity anomaly less than -0.040 psu for $24.7 < \sigma_\theta < 25.2$ kg m$^{-3}$ was then considered to be indicative of the effluent plume. Figure 2.13 illustrates this detection scheme using the profile from dive 90 of the SPS glider.

The automatic detection method identified portions of 197 profiles as indicative of the effluent plume. Of those, 126 were also identified by the manual detection. Most of the remaining profiles detected automatically were located in close proximity to both the OCSD outfall and profiles that were identified manually. Some profiles that were relatively far from the outfall were identified (Figure 2.12), and increasing the selectivity of the algorithm (by changing the bandpass parameters and cutoff values) eliminated many of those profiles from detection. Some profiles near the OCSD outfall were also eliminated when the selection criteria were altered. Based on the overall agreement between the manual and automatic detection methods, we believe that the parameters presented for the automatic method were an appropriate compromise between generating false-positive and false-negative results for this outfall.

#### 2.3.3.3 Plume Transport

The fate of the effluent plume is critical to beach water quality. Under conditions of alongshore flow in May 2000, *Boehm et al.* [2002] used measurements of *E. coli* to show that the effluent plume remained offshore and subsurface. The effluent plume from the OCSD outfall was similarly isolated from the nearshore and surface during fall 2006. The effluent plume settled near the $\sigma_\theta = 25.0$ kg m$^{-3}$ isopycnal. At no point during the Spray surveys did this isopycnal reach the surface, so the effluent plume most likely remained subsurface within the survey region. Salinity measurements from the mooring array indicated that the effluent plume was not transported into the nearshore. The only mooring to show the salinity anomaly characterizing the effluent plume was MA, the mooring furthest from shore. Anomalously low salinities at MA were apparent at 45 m depth, but not at 25 m depth (Figure 2.11), so the effluent plume was trapped well below the surface.

Most indications of the effluent plume were to the north and west of the OCSD outfall (Figure 2.12). Although our observations to the south and east of the outfall were sparse, the location of the plume to the northwest of the outfall was consistent with advection of the plume by the mean vertically averaged currents (Figure 2.3). Profiles that indicated the presence of the effluent plume to the south and southeast of the OCSD outfall may have been the result of the following: the transport of the effluent by currents in the opposite direction of the mean flow; our selection criteria admitting some profiles that were not truly indicative of the effluent plume; or the influence of other, smaller ocean outfalls in the region. Vertically averaged current estimates from the SPS glider on 6–8 October showed southeastward currents at the northern end of its survey pattern. During the same time, ADCP measurements at the MA mooring site indicated that the alongshore component of the current near the depth of the plume (approximately 40 m) switched directions (Figure 2.14). Thus it is plausible that the effluent plume was advected southeastward along the coast at some times during our observation period.

## 2.4 Conclusion

Glider observations in the greater San Pedro Bay region during the fall of 2006 showed the physical and biological conditions during HB06 and the weekly to monthly variability during the transition from summer to winter conditions. The gliders surveyed most of SPB and collected measurements on spatial and temporal scales that have not been previously reported in the region. Moreover, our observations highlighted the importance of salinity structure in this portion of the Southern California Bight. The influence of subarctic waters recirculated in the bight appeared as a subsurface salinity minimum throughout the surveyed region. The strength of the SSM diminished in late fall, likely resulting from reduced recirculation within SPB.

A subsurface chlorophyll maximum was present throughout San Pedro Bay during the fall of 2006, and zooplankton migrated upwards to the chlorophyll maximum at night, presumably to feed. The strength and depth of the SCM varied throughout the surveys, notably shoaling over the San Pedro Shelf compared to over deeper water. The SCM was generally stronger over the San Pedro Shelf and strengthened in early winter.

Three glider sections through a small cyclonic eddy to the southeast of Santa Catalina Island provided a novel view of an eddy of this size in the Southern California Bight. The stationary eddy extended from the surface to approximately 100 m depth with doming isopycnals supporting geostrophically-balanced cyclonic currents. Consistent with theory, nitrate content in the euphotic zone was estimated to be 19% higher within the eddy, and chlorophyll concentrations were significantly greater within the eddy.

Glider surveys in the vicinity of the OCSD ocean outfall were used to identify and track an effluent plume based on its characteristic low salinity anomaly. Separate manual and automatic detection schemes agreed well, and showed that the effluent plume settled near the 25.0 kg m$^{-3}$ isopycnal and was advected primarily to the north and west of the outfall by observed currents. No observations showed the effluent plume near the surface, and comparison to mooring-based measurements of salinity over the inner San Pedro Shelf did not show evidence of onshore transport of the effluent plume during September-October 2006.

*Acknowledgments.* The Spray glider deployments would not have been possible without the support of the Instrument Development Group at the Scripps Institution of Oceanography. Mooring data were collected by George Robertson at OCSD and Marlene Noble at USGS and distributed by SAIC. We thank all those involved in collecting the CalCOFI data used in this analysis. This work was supported by the California Coastal Conservancy's Coastal Ocean Current Mapping Program (COCMP), NOAA through grant number NA17RJ1231, and a National Defense Science and Engineering Graduate (NDSEG) Fellowship to R. E. Todd. Chapter 2, in full, is a reproduction of the material as it appears in *Todd, Rudnick, and Davis* [2009], *J. Geophys. Res., 114*, C06001. The dissertation author was the primary investigator and author of this work.

## Appendix 2.A Correcting for Nonphotochemical Quenching

As with all fluorometric measurements of chlorophyll, our sensors measured fluorescence at wavelengths characteristic of chlorophyll *a*. Voltages recorded by the fluorometers were converted to chlorophyll-like units by scaling using the factory calibrations. As the gliders were unable to collect in situ measurements of chlorophyll concentration, we regarded the chlorophyll concentrations presented here as relative values only.

Due to the relatively slow movement of the gliders, a diel cycle in fluorescence is often observed in shallow waters with reduced fluorescence during daylight [*Davis et al.*, 2008]. This cycle is largely the result of nonphotochemical quenching [e.g., *Kiefer*, 1973] of fluorescence, and therefore it is not representative of phytoplankton abundance, the quantity in which we are ultimately interested.

We attempt to correct the chlorophyll fluorescence measurements by removing the portion of the fluorescence signal that is correlated with surface light intensity. We let $\tilde{F}(z,t)$ be the measured fluorescence as a function of depth (pressure) and time (or distance along track), and let $\phi(0,t)$ be the surface light intensity. We assume that the fluorescence can be modeled as

$$\tilde{F}(z,t) = A(z)\phi(0,t) + F(z,t), \tag{A1}$$

where the function $F(z,t)$ is uncorrelated with the surface light intensity and is the portion of the signal that we wish to obtain. A separate and unpublished experiment in which a Spray glider on CalCOFI Line 90 completed approximately four days of dives to 100 m depth with temporal resolution of approximately 0.75 h suggests that this linear model of fluorescence as a function of surface light intensity is valid. If we can determine $A(z)$, then we can remove the portion of the measured fluorescence, $\tilde{F}(z,t)$, that is correlated with surface light by simply keeping only $F(z,t)$.

The covariance of fluorescence with surface light is

$$\begin{aligned} \left\langle \tilde{F}(z,t)\phi(0,t) \right\rangle &= A(z)\left\langle \phi(0,t)\phi(0,t) \right\rangle + \left\langle F(z,t)\phi(0,t) \right\rangle, \\ &= A(z)\left\langle \phi(0,t)\phi(0,t) \right\rangle, \end{aligned} \tag{A2}$$

since $F(z,t)$ is assumed to be uncorrelated with the surface light. It follows that the portion of the fluorescence signal that is uncorrelated with surface light is

$$F(z,t) = \tilde{F}(z,t) - \frac{\left\langle \tilde{F}(z,t)\phi(0,t) \right\rangle}{\left\langle \phi(0,t)\phi(0,t) \right\rangle}\phi(0,t). \tag{A3}$$

It is relatively simple to show that the same result can be obtained by solving for $A(z)$ in (A1) using least squares techniques. Thus we exploit the computational efficiency of the least squares approach in actually calculating the corrected fluorescence signal. The linear regression is calculated over sliding groups of 32 dives (approximately 4 days) and the correction is applied from the surface to the depth at which the correlation of surface light with fluorescence becomes greater than $-0.2$. That is, we apply the correction until the correlation (which should be negative for nonphotochemical quenching) becomes sufficiently small. This method is similar to that of *Davis et al.* [2008], but we do not make the assumption that the decay rate of the covariance of measured fluorescence with surface light, $\left\langle \tilde{F}(z,t)\phi(0,t) \right\rangle$, is equal to the attenuation rate of light.

Due to the large number of dives that did not reach the surface during the deployment of the SPS glider, the technique could not be applied to the data from that glider. Thus, only the chlorophyll measurements from the SCI and L90 gliders were corrected for nonphotochemical quenching in this analysis.

## Appendix 2.B Current Estimates

The Spray gliders obtain a GPS fix upon reaching the surface after each dive and before leaving the surface for the next dive. These GPS fixes provide a measure of the total displacement of the glider while underwater. Measurements of pressure, pitch and heading allow us to determine the glider's displacement relative to the water during a dive. The difference between the measured displacement and the displacement relative to the water divided by the duration of the dive provides a measure of the vertically averaged current during each dive. We correct for surface drift and the slower ascent and decent rates of the glider near the top and bottom of the profiles.

We calculate geostrophic shear from horizontal density gradients between pairs of adjacent profiles in the usual manner. Since we desire spatial gradients rather than temporal gradients, we disregard gradients calculated from those pairs of profiles that are too closely spaced in the horizontal relative to their temporal spacing. Under optimal conditions, the ratio of the horizontal separation of two profiles and the times of those profiles will be on the order of 0.25 m $s^{-1}$, the speed of the glider through the water. We disregard gradients from pairs of dives in which this ratio is less than 0.125 m $s^{-1}$.

Integrating the geostrophic shear downwards from the surface to a given depth gives the geostophic velocity at that depth relative to the surface. A vertically-constant velocity is then added to the resulting velocity profile so that its vertical average is equal to the mean across-track vertically averaged current for each dive pair. As noted in the study by *Davis et al.* [2008], these geostrophic velocity estimates do not account for Ekman transport.

Profiles of the resulting across-track geostrophic velocities must then be smoothed to eliminate small-scale effects that are not in geostrophic balance. A balance of terms in the equations of motion suggest that the internal Rossby radius is approximately the horizontal scale at which geostrophy is valid. For SPB, the internal Rossby radius is on the order of 10 km, so the profiles are binned to 10 km.

## Appendix 2.C Comparisons Between Glider and Mooring Measurements

The SPS glider passed within a few hundred meters of the MA mooring during three circuits of its survey pattern. These passes provided an opportunity for comparing glider measurements of salinity and currents to similar measurements from the mooring. Twenty-one glider profiles of temperature and salinity within 0.5 km of the MA mooring and 26 estimates of vertically averaged current within 1.5 km of the mooring were made. A larger region around the mooring was required to obtain a sufficient number of estimates of vertically averaged currents because the glider made multiple profiles without surfacing while near the mooring.

Temperature and salinity were measured by two Sea-Bird Electronics MicroCATs on the mooring at 25 and 45 m depths. We compared salinities along isotherms during the duration of each glider profile. Salinity measurements at 45 m on the mooring were always fresher than the corresponding glider measurements by an average of 0.10 psu. Glider measurements were fresher than mooring measurements at 25 m for all but two profiles with an average difference of 0.06 psu. The mooring measurements bracketed the glider measurements. Without other data, we could not determine which of the three sensors had the most absolute accuracy, but since the glider used a single sensor to collect a salinity profile, any offset in the glider measurements would not have affected the shape of the resulting salinity profile and our analysis in Section 2.3.3 is not affected. The $\theta$-$S$ relationships were similar for the glider and mooring measurements (Figure 2.11).

To compare current measurements from the bottom-mounted ADCP at MA with the glider estimates of vertically averaged currents, we averaged the ADCP currents over the depth range and time span of each nearby glider profile. For consistency, we only used current estimates from glider dives shallower than 57 m, the depth at the MA site. We fitted glider estimates to moored estimates by solving

$$\left(u_{\text{glider}} + iv_{\text{glider}}\right) = m\left(u_{\text{mooring}} + iv_{\text{mooring}}\right), \tag{C1}$$

for the complex coefficient $m$ using least squares. The resulting fit showed the glider estimates to be 5.4% larger than the mooring estimates with a difference in direction of 0.8°. Much of the increased magnitude in the glider estimates was attributable to several successive estimates on 14 October when the glider current estimates showed significantly stronger westward flow than did the mooring estimates. These points are apparent in a scatter plot of the glider estimates against corresponding mooring estimates (Figure 2.C1). The glider estimates of vertically averaged currents agreed well with the moored estimates. This result is particularly encouraging since the glider estimates result from shallow multi-cycle dives during which the glider spends a larger portion of the dive moving slowly in the vertical, thereby making its horizontal motion through the water difficult to determine. During longer, deeper dives, the glider's motion through the water is better known, and we may expect more reliable velocity estimates.

**Table 2.1**: Deployment Statistics for the Three Gliders Deployed in the Greater San Pedro Bay Region During Fall 2006[a]

| Glider | SPS | SCI | L90 |
|---|---|---|---|
| Deployment date | 23 September | 23 September | 19 October |
| Recovery date | 21 October | 20 October | 19 January |
| Number of days | 28 | 27 | 92 |
| Number of Profiles | 716 | 289 | 846 |
| Spatial resolution (km) | $0.74 \pm 0.86$ | $1.94 \pm 0.87$ | $2.43 \pm 0.82$ |
| Temporal resolution (hours) | $0.90 \pm 0.81$ | $2.25 \pm 0.68$ | $2.59 \pm 0.57$ |

[a] Spatial and temporal resolutions are given as the mean value for each deployment plus or minus the standard deviation for each deployment.

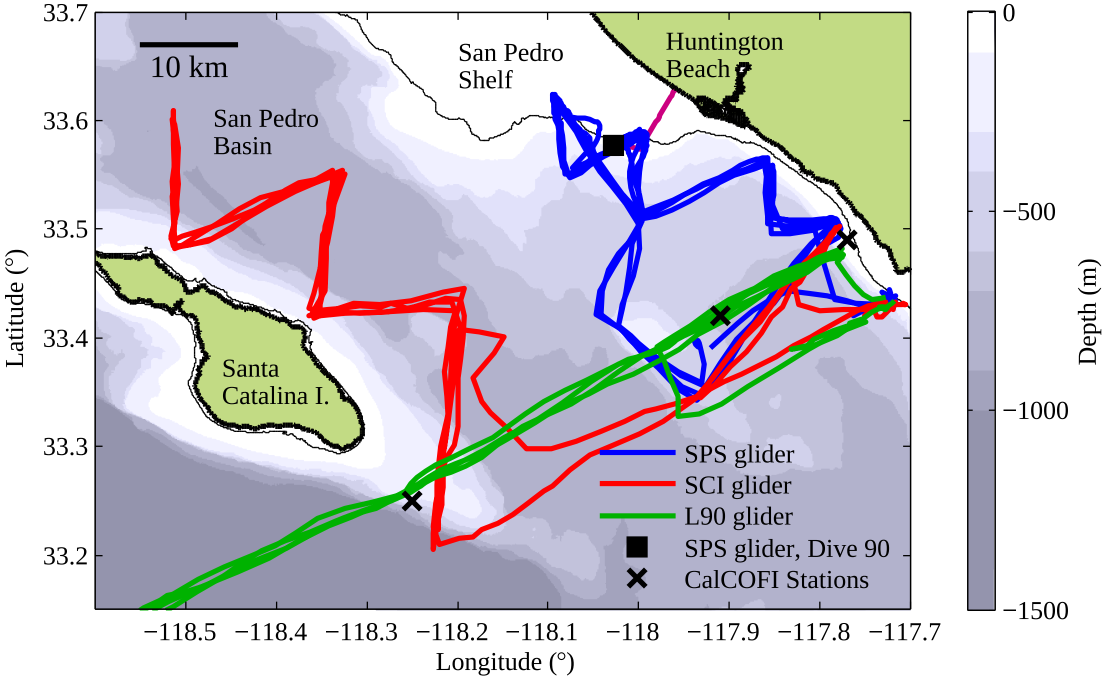

**Figure 2.1**: Bathymetry (shading) of the greater San Pedro Bay region with glider tracks overlaid. The coastline and 50-m isobaths are shown by the heavy and light black contours, respectively. The OCSD outfall pipe is shown by the heavy magenta line perpendicular to the coast near 33.6°N. The tracks of SPS, SCI, and L90 gliders are blue, red, and green, respectively. The black square denotes the position of dive 90 of the SPS glider. CalCOFI stations 90.28, 90.30, and 90.35 are shown by the black cross symbols. Station numbers increase away from the coast.

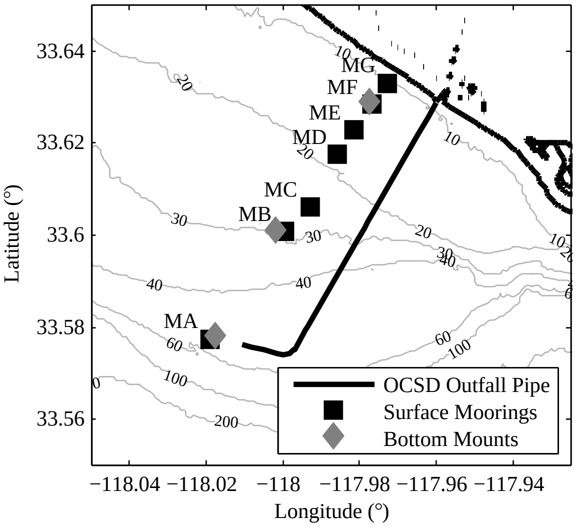

**Figure 2.2**: Locations of surface moorings and bottom-mounted instruments used in this analysis. Surface moorings are indicated by squares and bottom-mounted instruments by diamonds. The OCSD outfall pipe is shown by the heavy black line and bathymetry is gray with depths in meters.

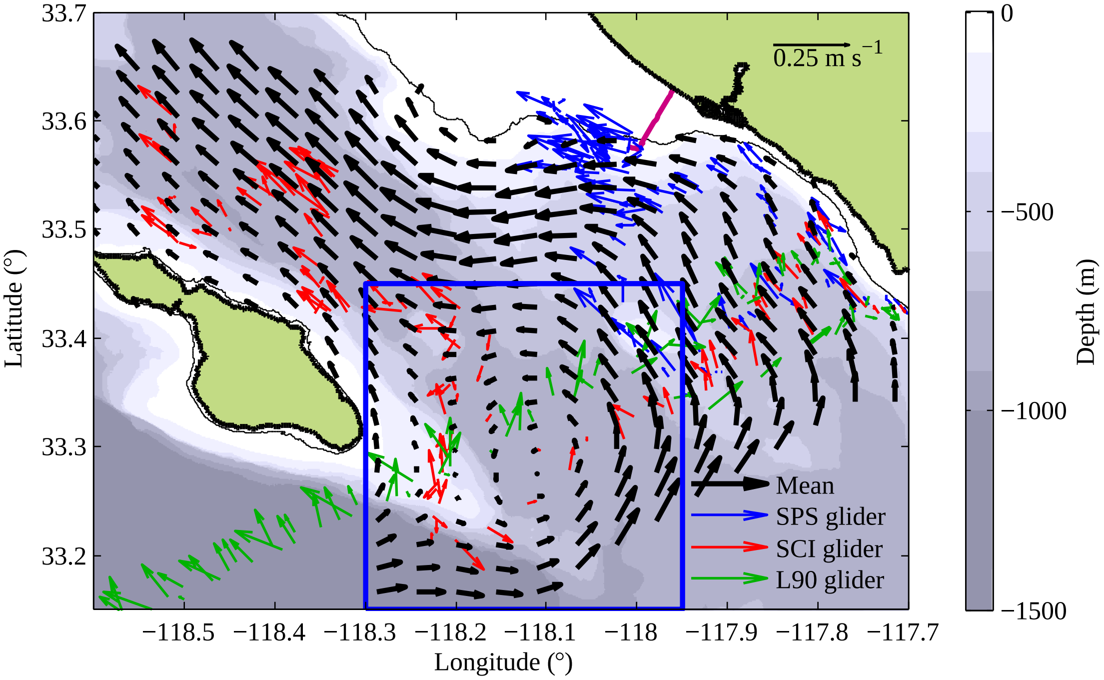

**Figure 2.3**: Vertically averaged currents in the greater San Pedro Bay region during the observation period. Averages over six hours of vertically averaged currents measured by the three gliders are shown in blue (SPS glider), red (SCI glider) and green (L90 glider). Heavy black vectors are a mean during the deployments of the SPS and SCI gliders formed by objective mapping. Bathymetry and the OCSD outfall are as in Figure 2.1. A vector representing a current of 0.25 m s$^{-1}$ is shown in the upper right. The blue box corresponds to the region shown in Figure 2.6.

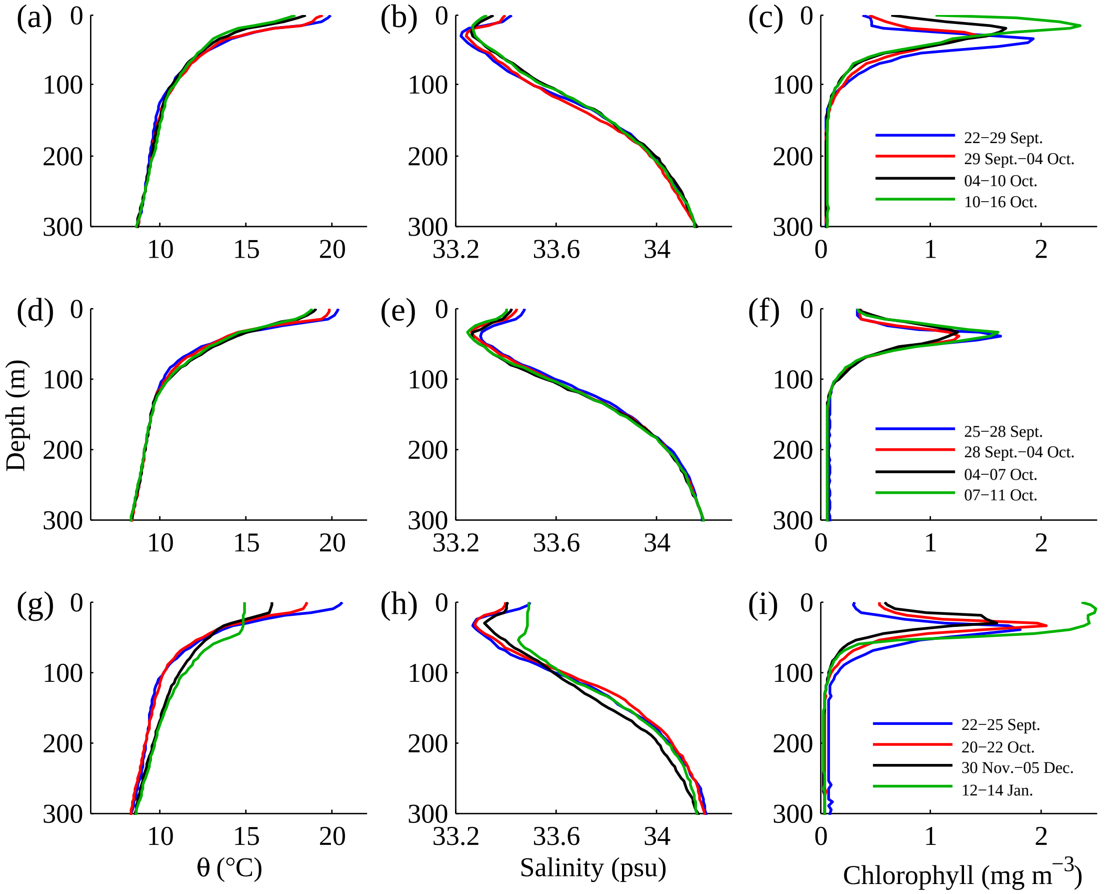

**Figure 2.4**: (a, d, g) Mean profiles of potential temperature, (b, e, h) salinity, and (a, f, i) chlorophyll from (a–c) the inshore survey pattern of the SPS glider, (d–f) offshore survey pattern of the SCI glider, and (g–i) crossings of San Pedro Channel from Dana Point, California to Santa Catalina Island. The dates of each survey are indicated in the figure legends and apply to all plots in a given row.

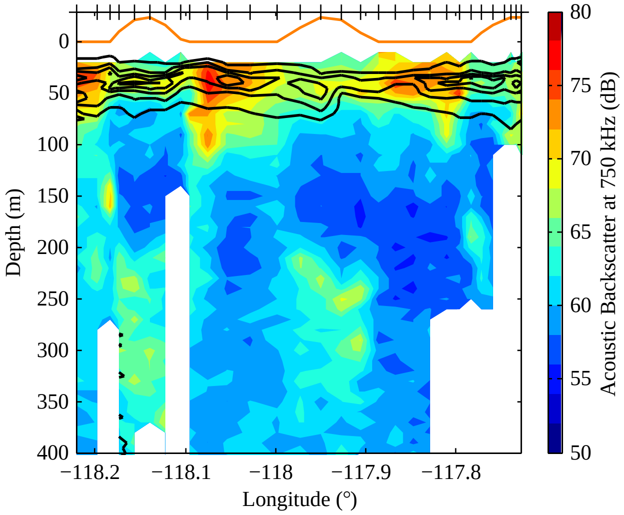

**Figure 2.5**: Chlorophyll fluorescence (black contours of 0.5 mg m$^{-3}$) and acoustic backscatter at 750 kHz for an east to west crossing of the San Pedro Channel by the SCI glider from 22 to 25 September. A geometric representation of sun angle is shown in orange, with values of zero at night. Tick marks on the top axis show individual dive locations.

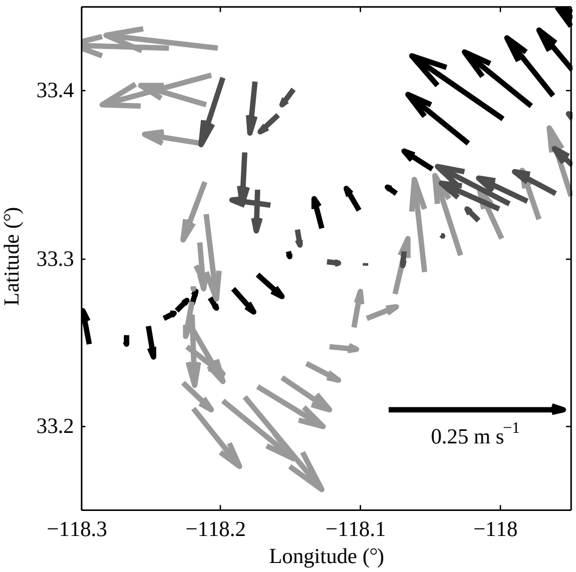

**Figure 2.6**: Individual measurements of vertically averaged currents to the southeast of Santa Catalina Island during three passes by the gliders on 24–26 September (light gray), 11–14 October (medium gray), and 20–22 October (black). A vector representing a current of 0.25 m s$^{-1}$ is shown in the lower right.

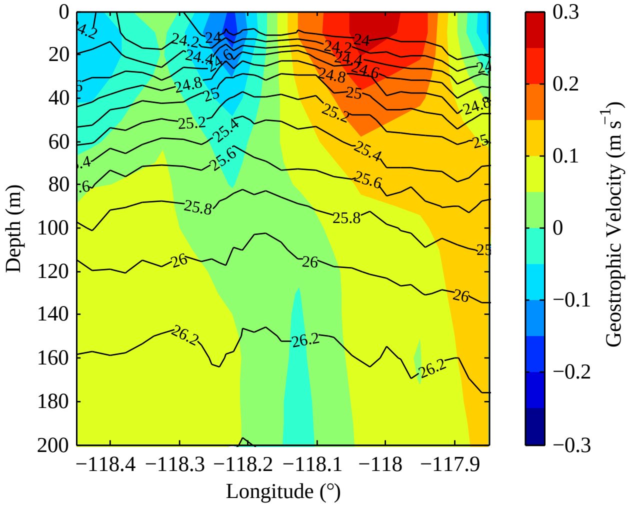

**Figure 2.7**: Potential density (contours in kg m$^{-3}$) and across-track geostrophic velocity referenced to vertically averaged velocity (colors) for the portion of the track of the L90 glider that passed through the eddy. Positive velocities are poleward (into the page). Data from dives 8–41 on 20–23 October are shown.

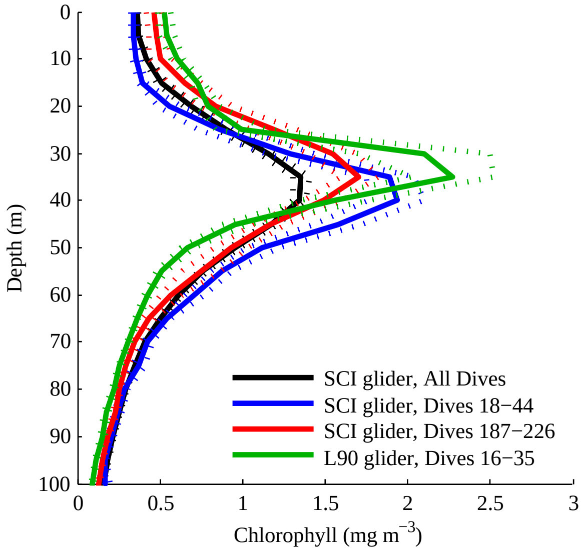

**Figure 2.8**: Average profiles of chlorophyll fluorescence for each pass through the eddy by a glider (blue, red, and green), and the mean profile for dives by the SCI glider that were west of 117.9°W and not within the eddy (black). The dotted lines represent 90% confidence intervals about the mean profiles.

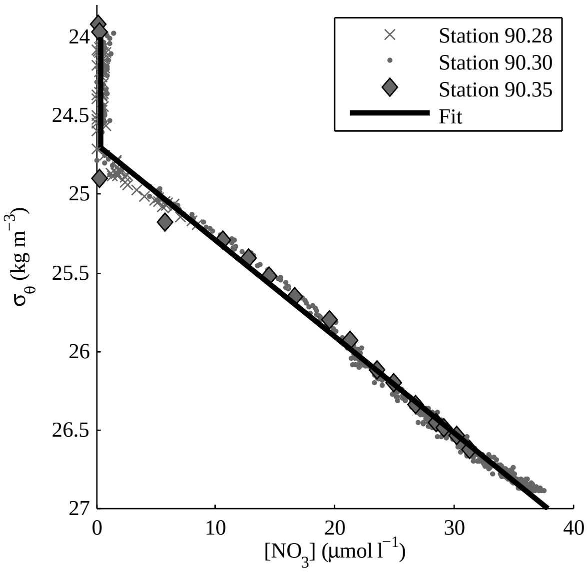

**Figure 2.9**: Measured nitrate concentration versus potential density for CalCOFI stations 90.28 (cross symbols), 90.30 (dots), and 90.35 (diamonds). The piecewise continuous least squares fit to the data, equation (2.1), is shown in black.

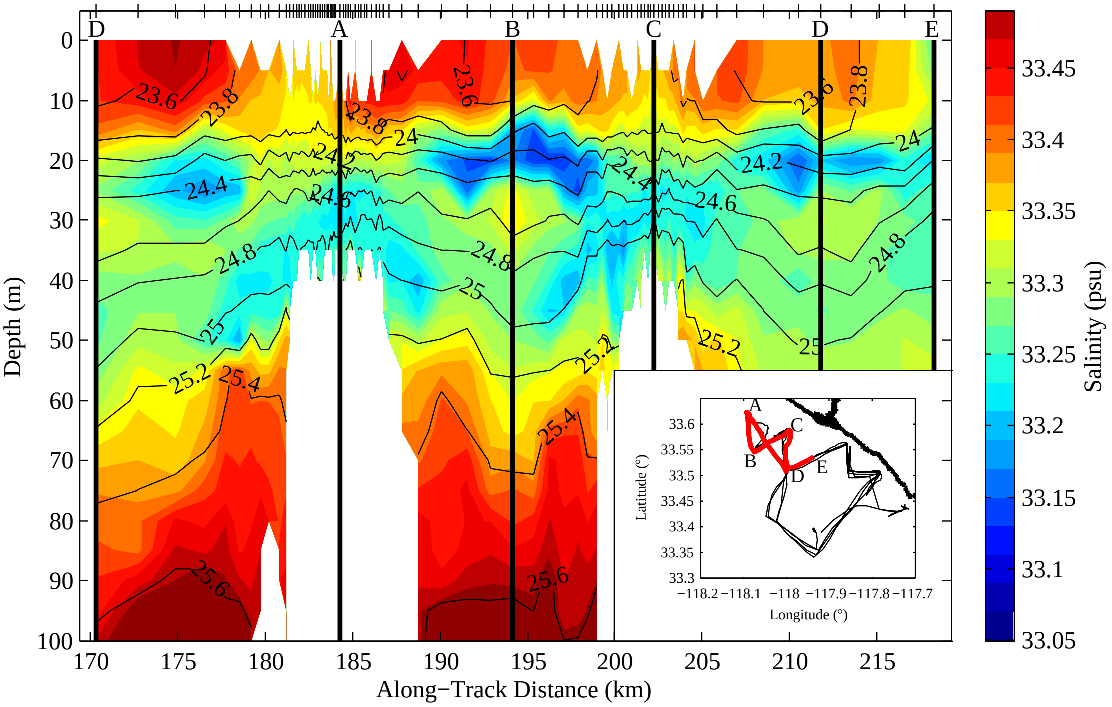

**Figure 2.10**: Salinity (color) and potential density (contours in kg m$^{-3}$) versus depth along a 50-km portion of the track of the SPS glider. The portion of the track is highlighted in red in the inset plot. Data shown are from 3 to 5 October. The two regions with dives to maximum pressures of less than 40 db correspond to the portions of the glider track over the San Pedro Shelf. The OCSD outfall is located near kilometer 202 along the glider track. Tick marks on the top axis show individual dive locations. Black bars at 184, 194, 202, and 212 km correspond to corners in the glider's track and are identified sequentially in the plot and inset figure by the letters A through D. Turn C is essentially on top of the OCSD outfall pipe. The section shown begins near turn D and ends near the point labeled E in the inset figure.

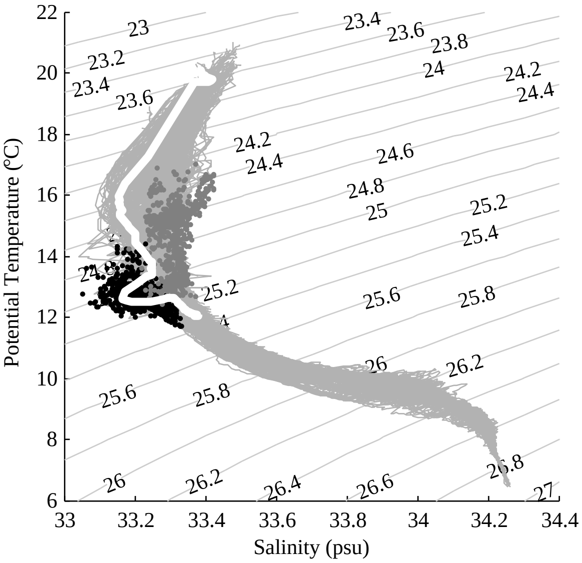

**Figure 2.11**: Potential temperature versus salinity profiles for all dives of the SPS glider (gray). The profile for dive 90 is highlighted in white. Also shown are potential temperature versus salinity at 25 m (medium gray) and 45 m (black) depth on the MA mooring during the time of the Spray surveys. Isopycnals are shown in light gray with labels in kg $m^{-3}$. The minimum in salinity at potential temperatures near 16 °C is indicative of subarctic waters from the California Current and is apparent in the majority of profiles. The low salinity anomaly at potential temperatures less than 14 °C is due to the effluent plume from the OCSD outfall. The highlighted profile shows this salinity anomaly particularly well.

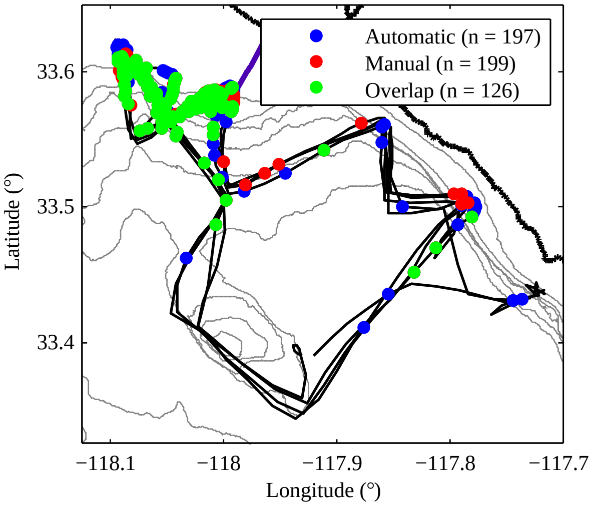

**Figure 2.12**: Locations of dives that indicated the effluent plume from the OCSD outfall. Points detected by only the automatic method are blue, those detected only by the manual method are red, and those detected by both methods are green. Bathymetric contours (gray) are shown at 50, 100, 200, 300, 400, 500, 750, and 1000 m, and the OCSD outfall pipe is indicated as in Figure 2.1. The track of the SPS glider is in black.

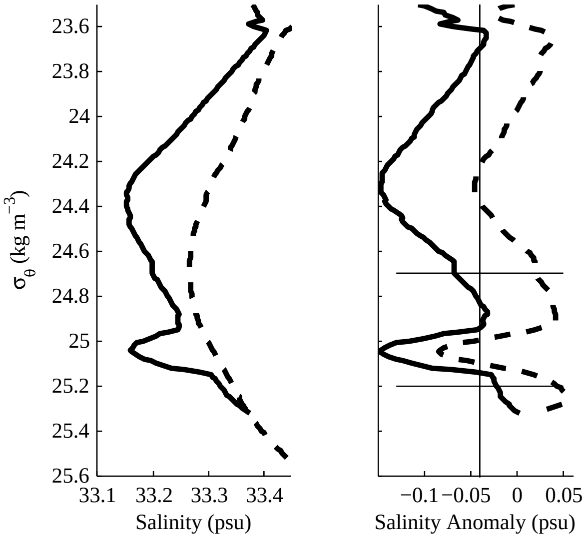

**Figure 2.13**: Illustration of the automatic plume detection scheme applied to the salinity profile from dive 90 of the SPS glider. (left) Original salinity profile (solid line) and mean profile over the deployment of the SCI glider (dashed line). (right) Mean-removed (solid line) and band-pass–filtered (dashed line) profiles, with the detection limits shown by the thin lines.

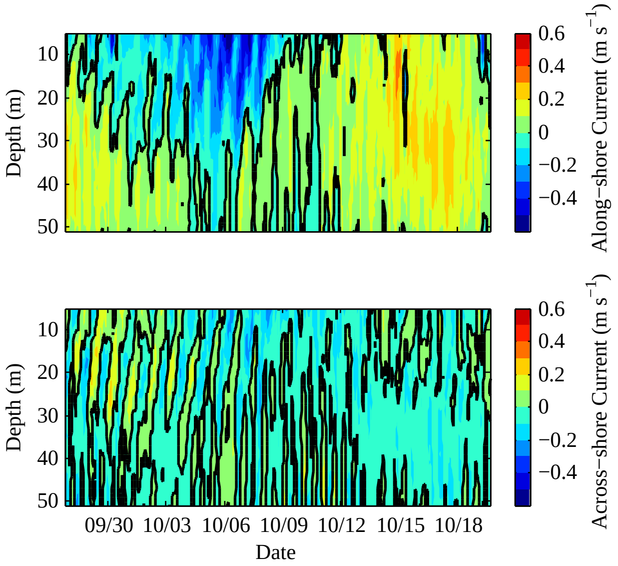

**Figure 2.14**: (top) Alongshore and (bottom) across-shore current velocity from the bottom-mounted ADCP at the MA mooring. The axes have been rotated 62 degrees counterclockwise so that positive alongshore velocities are poleward and positive across-shore velocities are onshore. The zero contour is indicated by the black line in both plots.

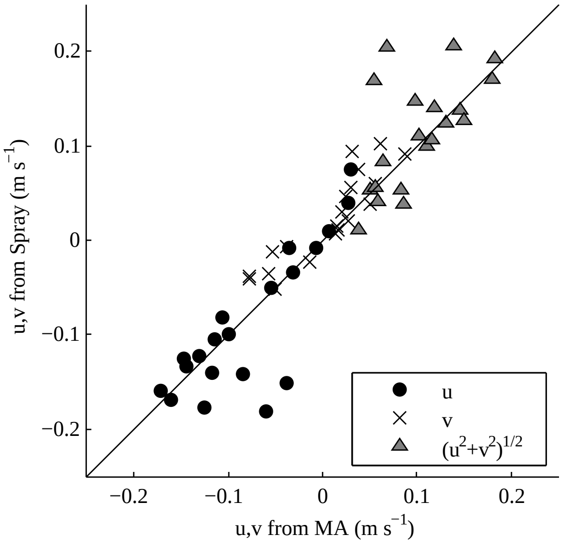

**Figure 2.C1**: Glider estimates of vertically averaged currents within 1.5 km of the MA mooring plotted against corresponding estimates of vertically averaged currents from the bottom-mounted ADCP at the MA mooring site. Eastward velocity (dots), northward velocity (cross symbols), and current magnitude (triangles) are shown. The black line is a one-to-one relationship.

# Chapter 3

# Poleward flows in the southern California Current System: Glider observations and numerical simulation

Robert E. Todd, Daniel L. Rudnick, Matthew R. Mazloff, Russ E. Davis, and
Bruce D. Cornuelle

**Abstract.** Three years of continuous Spray glider observations in the southern California Current System (CCS) are combined with a numerical simulation to describe the mean and variability of poleward flows in the southern CCS. Gliders provide upper ocean observations with good across-shore and temporal resolution along two across-shore survey lines while the numerical simulation provides a dynamically consistent estimate of the ocean state. Persistent poleward flows are observed in three areas: within 100 km of the coast at Point Conception, within the Southern California Bight (SCB), and offshore of the SCB and the Santa Rosa Ridge (SRR). Poleward transport by the flows within the SCB and offshore of the SRR exceeds the poleward transport off Point Conception, suggesting that the poleward flows are not continuous over the 225 km between observation lines. The numerical simulation shows offshore transport between the survey lines that is consistent with some of the poleward flow turning offshore before reaching

Point Conception. The poleward current offshore of the SRR is unique in that it is strongest at depths greater than 350 m and it is observed to migrate westward away from the coast. This westward propagation is tied to westward propagating density anomalies originating in the SCB during the spring-summer upwelling season when wind stress curl is most strongly positive. The across-shore wave number, frequency, and phase speed of the westward propagation and the lack of across-shore transport of salinity along isopycnals are consistent with first-mode baroclinic Rossby dynamics.

## 3.1 Introduction

The California Current System (CCS), an eastern boundary current system, is composed of variable equatorward and poleward currents. The equatorward flowing California Current carries cold, fresh waters of northerly origin while poleward flows transport warm, salty waters of southerly origin [*Wooster and Jones*, 1970; *Hickey*, 1979; *Lynn and Simpson*, 1987; *Huyer et al.*, 1989]. The poleward flowing California Undercurrent (CU) within the Southern California Bight (SCB) [*Lynn and Simpson*, 1990] and near Point Conception, as well as surface poleward flow near the coast, have been observed for decades by the California Cooperative Oceanic Fisheries Investigations (CalCOFI) program (http://www.calcofi.org) and other investigations [*Lynn and Simpson*, 1987; *Bray et al.*, 1999]. Recent velocity observations [*Davis et al.*, 2008; *Gay and Chereskin*, 2009] have revealed an additional subsurface poleward current offshore of the SCB to be a persistent feature in the CCS. This paper uses new observations collected by underwater gliders in the southern portion of the CCS and a new, regional, numerical state estimate to characterize the mean and variability of the poleward flows. Our observations show that the poleward current offshore of the SCB propagates westward in response to density anomalies propagating westward from the SCB and that the across-shore wave number and frequency of this westward propagation are consistent with first-mode baroclinic Rossby wave dynamics.

Historically, flow within the southern CCS has been diagnosed from thermal wind and decades of repeat hydrography, largely through the CalCOFI program. In most cases, the 500 db surface has been used as a level of no motion since CalCOFI measurements extend to 500 m. The resulting picture of the geostrophic flow [*Sverdrup and Fleming*, 1941; *Hickey*, 1979; *Lynn and Simpson*, 1987] shows the equatorward flowing California Current near the surface and somewhat offshore, the poleward flowing CU near the coast with highest velocity at depths of 100–300 m, and seasonally reversing surface flow near the coast. South of Point Conception, the CU appears inshore of the Santa Rosa Ridge (SRR, Figure 3.1) and flows between the various islands. Gaps in the SRR provide pathways for the CU to exit the SCB [*Lynn and Simpson*, 1990].

Subsurface poleward flow offshore of the SRR has been inferred occasionally from hydrography. *Sverdrup and Fleming* [1941] found northward flow at a depth of 200 m near the offshore side of the SRR during three cruises from March to July 1937. They identified the poleward flowing waters as having higher temperature and salinity than waters within the California Current, an indication of southerly origin. *Lynn and Simpson* [1990] used thermal wind referenced to 1000 db from a single survey in July 1985 to infer poleward flowing water of southern origin in the same region; they attributed the flow to an eddy formed by CU waters discharged through a gap in the SRR.

Velocity measurements within the southern CCS have recently revealed a poleward current offshore of the SRR to be a persistent feature. Geostrophic velocities referenced to vertically averaged currents from glider measurements on CalCOFI Lines 80.0 and 93.3 [*Davis et al.*, 2008] showed mean subsurface poleward flow within 100 km of the coast (the CU) as well as 200–250 km offshore on Line 80.0 and Line 93.3 from 2005 to early 2007. *Gay and Chereskin* [2009] used ten years of shipboard acoustic Doppler current profiler (ADCP) measurements from the quarterly CalCOFI cruises to show that the offshore poleward current is a persistent feature along Lines 86.7, 90.0, and 93.3, which fall within the SCB, but found only a single core (the CU) in the 10 year mean near Point Conception. The second poleward core at Line 80.0 seen in the glider observations was likely an artifact of the shortness of the data record available [*Davis et al.*, 2008], and glider observations of longer duration presented here do not show significant mean poleward flow at that location. The current offshore of the SRR has significant poleward flow at depths of 500 m and its speed diminishes with decreasing depth. Consequently, geostrophic calculations that assume zero flow at 500 m produce a surface intensified equatorward flow at the same location [*Davis et al.*, 2008].

The variability of the CU and shallow poleward flow within the SCB have been well documented [*Chelton*, 1984; *Lynn and Simpson*, 1987; *Bray et al.*, 1999; *Gay and Chereskin*, 2009], so our analysis focuses on the variability of the poleward current offshore of the SRR. *Gay and Chereskin* [2009] quantified the seasonal variability in transport of this offshore current and found it to be strongest in the fall. They found relatively little variability in the position of the current, but this is likely an effect of their mapping procedure which used long decorrelation scales and averaging in the alongshore direction [*Gay and Chereskin*, 2009]. The equatorward flowing California Current in the same region is known to meander [*Lynn and Simpson*, 1987], and our observations show that the poleward current offshore of the SRR propagates westward in a manner that is largely consistent with Rossby wave dynamics.

Rossby waves have been previously observed and modeled within the CCS. *White et al.* [1990] used satellite observations of sea surface height to characterize annual Rossby waves generated along the California coast. *Strub and James* [2000] hypothesized that westward propagating Rossby waves control offshore movement of a seasonal equatorward jet off central and northern California. *Lynn and Bograd* [2002] found that El Niño related dynamic height anomalies along Line 90.0 propagated westward at a phase speed consistent with a westward propagating Rossby wave. In a quasi-geostrophic numerical model, *Auad et al.* [1991] found that wind forcing generated first-mode baroclinic Rossby waves between 25° and 33°N. *Di Lorenzo* [2003] used the Regional Ocean Modeling System (ROMS) to demonstrate that density anomalies generated by alongshore wind stress and wind stress curl propagated westward from the SCB only when the $\beta$ effect was included. This dependence on the $\beta$ effect indicated that the westward propagation was the result of Rossby wave dynamics.

The remainder of this paper is arranged as follows: section 3.2.1 describes glider observations in the southern CCS; section 3.2.2 describes the numerical simulation; section 3.3.1 discusses the observed mean, transport, and variability of alongshore flow in the southern CCS; section 3.3.2 discusses the mean structure of poleward jets; section 3.3.3 characterizes the westward propagation of the current offshore of the SRR and compares the observations with Rossby wave dynamics; and section 3.4 summarizes the results. Two appendices discuss the accuracy of glider-based vertically averaged current measurements and describe velocity estimation using glider-mounted acoustic Doppler profilers.

## 3.2 Methods

### 3.2.1 Glider Observations

Spray gliders [*Sherman et al.*, 2001; *Davis et al.*, 2002; *Rudnick et al.*, 2004] are buoyancy-driven autonomous underwater vehicles that profile from the surface to a programmed depth while moving along a sawtooth flight path. Glider surveys in the southern portion of the CCS began in 2005 along established CalCOFI survey lines. Since October 2006, CalCOFI Lines 80.0 and 90.0 have been surveyed nearly continually by Spray gliders (Figure 3.2). Line 80.0 extends from Point Conception southwestward for approximately 350 km and passes through the upwelling center off Point Conception. Line 90.0 extends roughly 525 km southwestward from Dana Point, California and passes through the SCB (Figure 3.1). We use data collected between October 2006 and November 2009 in this analysis.

A typical deployment in the southern CCS begins just offshore of the kelp zone where the glider is placed in the water from a small boat. Gliders surveying Line 80.0 are deployed from Santa Barbara, California, and Line 90.0 gliders are deployed between San Diego and Dana Point, California. The gliders navigate to the inshore end of the appropriate CalCOFI survey line, then begin following the line to near its offshore end (typically to CalCOFI stations 80.100 and 90.100) where they reverse course and return to the inshore end of the line. Gliders take about three weeks to complete a transect in one direction, and battery life is sufficient for a glider to complete at least four full transects before being recovered and replaced by a refueled glider. The gliders are programmed to dive to 500 m when in deep water so that they cover approximately 3 km horizontally during a dive that lasts about 3 h. This analysis uses 57 transects from 13 deployments along Line 80.0 and 42 transects from 11 deployments along Line 90.0. Strong eddy activity at Line 80.0 often forces the gliders significantly off of their intended paths (Figure 3.1); gliders on Line 90.0 are only rarely displaced more than a few kilometers from the established survey line. Gliders deployed in the southern CCS are each equipped with a Sea-Bird 41CP conductivity-temperature-depth (CTD) sensor, a custom Sontek Argonaut 750 kHz acoustic Doppler profiler (ADP), and a Seapoint chlorophyll *a* fluorometer, all of which collect measurements on the ascending portion of the dive only [*Davis et al.*, 2008].

GPS fixes at the beginning and end of each dive are combined with records of pitch, heading, and depth during the entirety of each dive to measure vertically averaged currents, and these measurements are used to reference both geostrophic [*Davis et al.*, 2008; *Todd et al.*, 2009] and Doppler-derived velocity profiles (e.g., Figure 3.3). Vertically averaged currents from gliders have been shown to agree well with independent measurements from moored ADCPs [*Davis et al.*, 2002; *Todd et al.*, 2009], and Appendix 3.A considers sources of error in vertically averaged current measurements.

We use glider observations directly in our analysis whenever possible, but some applications (e.g., calculations of mean sections) require data on a uniform grid. For these applications, we objectively map the observations at each depth to a uniform grid using a Gaussian covariance matrix with a 30 km decorrelation scale and noise-to-signal ratio of 0.05. The length scale is close to the integral length scale of observed vertically averaged currents.

We also use objective mapping to calculate geostrophic velocities. We estimate the across-shore (along track) gradient of the density field by specifying appropriate covariance matrices. We again specify a 30 km length scale in the mapping, which eliminates density gradients due to internal waves. Alongshore (across-track) geostrophic velocities are calculated from the estimated density gradient by integrating the thermal wind relation and referencing to mapped vertically averaged current observations (e.g., Figure 3.3a).

The glider-mounted ADP provides vertical profiles of horizontal shear much like a lowered ADCP (LADCP) attached to a CTD rosette and lowered from a ship. Our processing is similar to that of the LADCP processing described by *Visbeck* [2002] but with the glider-based measurement of vertically averaged velocity used to reference the velocity profiles. Appendix 3.B provides the details of estimating horizontal velocity fields from the ADP. Sections of ADP-derived velocity (Figure 3.3b shows an example transect) have significant high-frequency variability from tidal, inertial, and other effects. Since this analysis focuses on lower-frequency processes, we apply a 30 h Gaussian filter in the time domain [*Pope*, 2000, Table 13.2] to the ADP velocity profiles when using individual transects of alongshore velocity in sections 3.3.2 and 3.3.3. These filtered velocities (Figure 3.3c) agree well with alongshore geostrophic velocities (Figure 3.3d). Since both the ADP-derived velocities and the geostrophic velocities are referenced to the measured vertically averaged currents, it is the agreement in vertical structure (shear) between filtered ADP-derived currents and geostrophic currents that is most reassuring. *Davis* [2010] calculates velocities from Spray glider-mounted ADPs by integrating vertical shears and finds similar agreement between smoothed ADP-derived velocities and geostrophic velocities. The slow horizontal speed of the gliders (about 0.25 m $s^{-1}$) results in a 30 km filter being nearly equivalent to a 30 h filter, so velocity estimates are not filtered in the time domain before being mapped onto a uniform grid. In this analysis, we use ADP-derived velocity estimates whenever possible, and only substitute geostrophic velocities during periods when ADP-derived current estimates are unavailable due to instrument failures (Figure 3.2).

The glider-based velocity estimates used in this analysis are referenced to measured vertically averaged currents and do not assume a level of no motion. This distinction sets them apart from the relative geostrophic velocity estimates used for most previous work in the CCS. Our results, with those of *Davis et al.* [2008] and *Gay and Chereskin* [2009], emphasize the need for properly referenced velocity measurements in the CCS.

### 3.2.2 Numerical Simulation

The numerical simulation used here is a regional version of the MITgcm [*Marshall et al.*, 1997a,b] that is based on the incompressible Navier Stokes equations. The model domain is $\begin{bmatrix} 130°\text{W} & 114°\text{W} \end{bmatrix} \times \begin{bmatrix} 27.2°\text{N} & 40°\text{N} \end{bmatrix}$ (Figure 3.1) with $\frac{1}{16}^{\circ}$ (about 6 km) horizontal resolution and 72 vertical levels. The model domain includes the west coast of North America from near Punta Eugenia in Baja California Sur, Mexico to near Cape Mendocino in California. The model is run for the period from 1 January 2007 to 30 July 2009 with a time step of 1200 s. Table 3.1 gives the values of viscosity, bottom drag, and diffusivities used in the model. First guess initial conditions and lateral boundary conditions are from an MIT-ECCO product [*Forget*, 2010]. First guess of the atmospheric state is from the North American Mesoscale (NAM) model produced by the National Centers for Environmental Prediction (NCEP).

We employ the 4DVAR state estimation technique [*Wunsch and Heimbach*, 2007] to bring the model solution into consistency with observations. The method uses the adjoint of the MITgcm [*Heimbach et al.*, 2005] to solve for the model controls (i.e., initial conditions and atmospheric state) that minimize the weighted misfit between the simulation and observations. The observations to be fit include: satellite sea surface temperature, satellite sea surface height (SSH), Argo CTD profiles, CalCOFI CTD profiles, Spray glider CTD profiles, moored CTD data, and other ship-based CTD measurements from the region. Glider profiles from Lines 80.0 and 90.0 (section 3.2.1) are supplemented by additional glider profiles from CalCOFI Line 66.7 off Monterey Bay. Velocity measurements are not used in the optimization. From a reference run with first guess controls, the model controls are iteratively adjusted to fit the observations in a least squares sense. The controls are constrained to remain within estimated errors of the first guesses, and smoothness constraints are also enforced. Our approach to optimizing the simulation has been to progressively increase the amount of structure in the controls, thereby ensuring large-scale agreement with observations before attempting to match smaller-scale features. To this end, the adjoint model is run with elevated horizontal viscosity (Table 3.1). For more on the adjoint method, see *Wunsch* [2006] and *Wunsch and Heimbach* [2007].

The simulation analyzed is a 31 month forward run of the model. The solution is strictly governed by the modeled dynamics and the optimized initial conditions and forcing fields. At this point in the optimization (the 64th data-assimilating iteration), only surface forcing and initial conditions have been solved for; boundary conditions are directly from the $1^\circ \times 1^\circ$ MIT-ECCO product. In contrast to sequential data assimilation techniques where unphysical discontinuities in the model state are a byproduct of the optimization, our simulation is dynamically consistent (adhering rigidly to model physics) while also being qualitatively consistent with the observed ocean. Though not a converged state estimate, the present solution exhibits the structure and temporal variability of the observed poleward flows (section 3.3.1), making it useful for analysis. The most significant remaining issue in the simulation is that, though the current structure is correct, the speeds, and therefore transports, tend to be 2–3 times smaller than observed. We suspect that this discrepancy is due to a combination of the smoothness constraints on the surface forcing fields as well as elevated viscosity in the adjoint run and our use of unadjusted, low resolution (1° × 1°) lateral boundary conditions. Our choice in developing the simulation has been to err on the side of smoothness and obtaining correct structure, and the slower currents in the simulation relative to observations are a consequence of this choice. Future efforts will work to improve this issue.

## 3.3 Results and Discussion

### 3.3.1 Alongshore Currents and Transport

Mean vertically averaged currents from glider observations along Lines 80.0 and 90.0 (Figure 3.1) are largely orthogonal to the two survey lines. In areas where the mean vertically averaged currents are equatorward, there tends to be an onshore component to the flow. Where poleward flows are strongest (e.g., near Point Conception, within the SCB on Line 90.0, and near 120°W on Line 90.0), depth averaged flow has little across-shore component. The remainder of our analysis focuses on only the alongshore component of the flow, defined to be perpendicular to the survey lines, since this component of the flow is largest in the mean and can be analyzed using geostrophic velocity estimates during times when ADP-derived velocity estimates are unavailable (Figure 3.2).

#### 3.3.1.1 Mean Alongshore Flow

The mean alongshore flow calculated over all available glider data on Lines 80.0 and 90.0 (Figures 3.4a and 3.4b) shows equatorward and poleward flow along both survey lines. Equatorward flow is strongest in the upper 150 m of the water column along both survey lines and is generally found greater than 50 km offshore at Line 80.0 and greater than 175 km offshore at Line 90.0. This equatorward flow is consistent with the well known California Current [*Hickey*, 1979; *Lynn and Simpson*, 1987]. Poleward flow at Line 80.0 is concentrated within 100 km of shore in the CU with peak speeds near 0.08 m $s^{-1}$ at depths between 50 and 300 m. At Line 90.0, mean flow inshore of the SRR (the dashed line 175 km from shore in Figures 3.4b and 3.4d) is poleward at all depths with some surface intensification and peak speeds of 0.05–0.07 m $s^{-1}$. This inshore poleward flow has been referred to alternately as the CU and the Inshore Countercurrent, with the latter referring to flow that manifests at the surface [*Lynn and Simpson*, 1987], but the mean flow presented here shows no distinction between subsurface and surface poleward flow that would warrant two names. Offshore of the SCB, mean poleward flow is found from the SRR to the offshore end of the survey line at depths below 300 m. The mean alongshore flow derived from the glider observations agrees well with the mean of *Gay and Chereskin* [2009] from more than a decade of shipboard observations, which suggests that the glider surveys now provide sufficient data to calculate stable mean fields.

The numerical simulation reproduces the key features of the mean alongshore flow at Lines 80.0 and 90.0 (Figures 3.4c and 3.4d). Off Point Conception, the model generates a narrow CU within 100 km of the coast with mean poleward velocities exceeding 0.02 m $s^{-1}$ between 100 and 400 m depth. Poleward velocities in the CU core are low by a factor of 2 to 3 in the model, but poleward flow extends beyond 500 m as in the observations. Along Line 90.0, the model produces poleward flow throughout the water column inshore of the SRR with highest velocities in the upper 150 m in agreement with observations. Offshore of the SRR, the model produces poleward flow in the region of the observed poleward current, but again with speeds reduced by a factor of 2 to 3. Equatorward flow is again surface intensified and split into at least two branches as in the observations. The agreement between the observed and modeled velocity fields is particularly encouraging since the numerical simulation does not incorporate any direct velocity observations. To produce realistic currents, the model is adequately reproducing the observed density and sea surface height fields that drive currents.

#### 3.3.1.2 Net Volume Transport

The two glider survey lines define a region for which we can calculate net transport. The eastern side of the region is closed off by the coast, but the western end (between the offshore ends of the survey lines) is open and not sampled by the gliders. Mean volume transports through Lines 80.0 and 90.0 are -1.0 Sv and 3.7 Sv, respectively (positive transports are poleward, Table 3.2). Estimates of standard errors of these mean transports are given in Table 3.2. To obtain standard errors, we estimate the integral timescale by integrating the time-lagged autocorrelation. We choose the maximum value of this integral to provide a conservative estimate of the number of degrees of freedom and standard error. Transports through the survey lines are significantly different from zero. There is a net volume flux into the region of 4.7 Sv which must be balanced by a combination of offshore flow between the offshore ends of the two survey lines and downward flow at 500 m depth.

The numerical simulation allows diagnosis of the remaining balance in volume transport. Alongshore volume transport through Line 80.0 in the model is -0.9 Sv, while poleward transport through Line 90.0 is 1.0 Sv. Simulated mean transports are of the correct sign along both survey lines, but transports through Line 90.0 have smaller magnitude than observed due to a combination of the weaker mean currents in the numerical simulation (Figure 3.4) and the difference in temporal coverage between the observations and simulation (Table 3.2 gives observed transports during the timespan of the simulation). Transport through the section between CalCOFI stations 80.100 and 90.100, which connects the offshore endpoints of the two glider survey lines, is 1.9 Sv directed offshore in the model, and balances the horizontal transport into the region through Lines 80.0 and 90.0. Net vertical transport at 500 m is not a significant contribution to the net volume transport.

These estimates of alongshore transport through the survey lines demonstrate the importance of using using properly referenced velocity measurements in the CCS. Previous work by *Roemmich* [1989] and *Bograd et al.* [2001] using geostrophic velocities relative to a level of no motion at 500 m in a box bounded by CalCOFI Lines 76.7 and 93.3 (about 75 km north and south, respectively, of our survey lines) found net equatorward transport through both the northern and southern boundaries. A similar calculation of geostrophic transports relative to 500 m using the glider observations also gives net equatorward transport through Line 90.0. The assumption of negligible flow at 500 m results in estimates of upper ocean transport that are qualitatively different from transport estimates obtained using properly referenced velocity estimates.

#### 3.3.1.3 Variability in Poleward Flows

The mean alongshore flow discussed in section 3.3.1.1 averages the meandering of the California Current and the poleward currents with the result being broader, slower flow than the synoptic current [*Chereskin and Trunnell*, 1996; *Bray et al.*, 1999]. Time series of alongshore currents averaged over the upper 500 m (or full depth in shallower water) from each transect along Lines 80.0 and 90.0 (Figure 3.5) show that the strength and position of poleward and equatorward currents vary significantly over the available record. At Line 80.0 (Figure 3.5a), the CU usually manifests as poleward (positive) alongshore flow within 100 km of the coast with peak vertically averaged velocities exceeding 0.20 m s$^{-1}$. At Line 90.0 (Figure 3.5b), poleward flow dominates the vertical averages within the SCB with peak vertically averaged velocities greater than 0.15 m s$^{-1}$. Offshore of the SRR on Line 90.0, the position of the strongest poleward flow is more variable and peak speeds regularly exceed 0.15 m s$^{-1}$. Poleward flow offshore of the SRR tends to migrate westward repeatedly along the survey line; we focus on this westward propagation in section 3.3.3.

The numerical simulation also shows considerable temporal variability in the poleward flows (Figure 3.6). The color scale is smaller in Figure 3.6 than in the previous plot to show the structure of the weaker flow in the model. Westward propagating signals are more apparent in the simulated alongshore velocity fields at Line 80.0, but the CU remains near the coast most of the time while other features migrate offshore. At Line 90.0, poleward flow dominates within the SCB as in the observations, while the poleward current offshore of the SRR migrates westward regularly.

### 3.3.2 Mean Poleward Jets

The poleward currents off Point Conception, within the SCB, and offshore of the SRR are narrow, meandering features with peak speeds substantially larger than indicated by the mean velocity sections of Figure 3.4. The narrowness and relative swiftness of these features justifies referring to them as "jets". To characterize the currents and the associated transports, we identify the poleward jets in each transect along Lines 80.0 and 90.0 and calculate mean properties of each current in a jet-following coordinate system. This allows us to define the width and depth of each jet and to show that the current offshore of the SRR is notably deeper than the others and likely not continuous with the CU at Pt. Conception.

We identify subsurface poleward jets as local maxima in the alongshore velocity averaged between 150 and 500 m ($\bar{v}$). For each maximum, we define the edges of the jet to be the first point in the onshore and offshore directions for which $\bar{v}$ equals half the peak value. A particular local maximum is excluded if it is exceeded by another local maximum within its identified edges, the value of $\bar{v}$ at the peak is less than 0.04 m s$^{-1}$, or the edges are less than 5 km apart. Figure 3.7 shows a typical transect on Line 90.0 and the identified jets. Along Line 80.0, the largest jet with a peak within 100 km is included in averaging; along Line 90.0, the largest jet inshore of the SRR (less than 175 km from shore) and the largest jet between the SRR and 400 km from shore are included in separate averages. We create a jet-following horizontal coordinate, $\hat{x}$, by setting $\hat{x} = 0$ ($\hat{x} = 1$) at the inshore (offshore) edge of each jet. Observed properties of the jets are interpolated onto a uniform grid in $\hat{x}$. We then average jet observations between transects in the jet-following coordinates.

The position and width of each jet determines the jet-following coordinate system, $\hat{x}$, so it is appropriate to discuss those properties of the jets before considering the results of averaging jets together. Table 3.3 gives the mean position and width of each of the three poleward jets. The jet off Point Conception is located closest to the coast. The mean position of the jet within the SCB is near the center of the bight, reflecting its tendency to meander within the bight. The jet offshore of the SRR on Line 90.0 is found about 100 km offshore of the SRR on average. We find the widths of the jets to be somewhat smaller than inferred from 10 years of shipboard ADCP data from CalCOFI [*Gay and Chereskin*, 2009]. The discrepancy may be the result of *Gay and Chereskin* [2009] using long decorrelation scales and averaging multiple transects in processing shipboard ADCP data. In both analyses, the jet offshore of the SRR is wider than the nearshore jets at Point Conception and within the SCB.

As expected, averaging the observations in a jet-following coordinate system results in peak velocities of the resulting mean jets (Figures 3.8a–3.8c) that are substantially larger than when the averaging does not account for meandering jets. At Line 80.0, poleward velocities exceed 0.11 m $s^{-1}$ at depths from 100 to 300 m near the center of the CU. This mean speed agrees well with the mean speed for the CU off northern California inferred from Lagrangian drifters [*Garfield et al.*, 1999] and from shipboard ADCP surveys over the shelf break from southern California to Vancouver Island [*Pierce et al.*, 2000]. Poleward velocities exceed 0.05 m $s^{-1}$ throughout the upper 500 m in the core of the jet. Within the SCB on Line 90.0, poleward flow peaks around 0.08 m $s^{-1}$ near the surface and exceeds 0.05 m $s^{-1}$ between the surface and 420 m depth. Though the jet was identified based on its subsurface properties, the mean jet (Figure 3.8c) extends to the surface; there appears to be no distinction between surface and subsurface poleward flow in the SCB. The poleward jet offshore of the SRR at Line 90.0 is concentrated deeper than the other jets. Poleward flow exceeding 0.08 m $s^{-1}$ is located deeper than 350 m and extends below the 500 m profiling depth of the gliders. Above this core, vertical shear is weak with isolines of poleward velocity nearly vertical. The depth of the velocity core offshore of the SRR is notably deeper than reported by *Gay and Chereskin* [2009] whose data were limited to the upper 400 m because of the range of the shipboard ADCP.

Salinity and density sections through the mean jets (Figures 3.8d–3.8f) confirm that the poleward flows transport warm and salty water northward below the thermocline. For each of the three cores of poleward flow, salinity increases along isopycnals in the onshore direction. Although isopycnals slope downward toward the coast, isohalines slope upward toward the coast within the core of the jets. This increase in spiciness [*Munk*, 1981] toward the coast indicates a change in water masses across the jets with warm and salty waters of southern origin [*Lynn and Simpson*, 1987] on the inshore side of the poleward jets. At the depth of the core of the jet offshore of the SRR, density and salinity are notably greater than in the jets within the SCB and off Point Conception.

Mean poleward transport by the two jets on Line 90.0 exceeds the poleward transport by the CU at Point Conception by more than a factor of two (Table 3.3). The CU at Point Conception has mean poleward transport of 2.0 Sv, an estimate that compares well with direct observations of the CU off northern Baja California near 31°N by *Wooster and Jones* [1970] and with the estimate of *Gay and Chereskin* [2009] from shipboard ADCP measurements on CalCOFI Lines 76.7, 80.0, and 83.3. Poleward transport by the jets along Line 90.0 is notably greater than reported by *Gay and Chereskin* [2009], and may be attributable to the deeper profiling depth of the gliders compared to the shipboard ADCP. The mean offshore transport between CalCOFI stations 80.100 and 90.100 of 1.9 Sv in the model is consistent with much of the poleward flow by the jets on Line 90.0 turning offshore before reaching Point Conception. The deeper depth and greater density and salinity of the jet offshore of the SRR and the evidence for offshore turning of the flow suggest that the poleward current offshore of the SRR is generally not continuous with the CU at Point Conception.

### 3.3.3 Westward Propagation

The variability in vertically averaged alongshore currents (Figure 3.5) suggests that the poleward undercurrent offshore of the SRR on Line 90.0 propagates westward while the CU at Point Conception and the poleward flow within the SCB meander back and forth in more limited regions. In this context, "westward" means toward the offshore end of Line 90.0, about 26° south of due west, since our observations are only along the line. We use autocorrelations of observed variables to verify this result and infer the dynamics behind the westward propagation of the poleward current offshore of the SRR.

#### 3.3.3.1 Autocorrelations

We calculate autocorrelations by averaging products of detrended pairs of measurements with similar spatial and temporal separations into bins that are 10 km by 30 days, a size that ensures a sufficient number of data in each bin, then normalizing by the variance. Observations are detrended by removing a mean and across-shore trend using least squares; no spatial or temporal harmonics are removed. Positive across-shore separations are to the west since we measure distance from the coast.

The autocorrelation of alongshore velocity at 300 m depth and offshore of the SRR (greater than 200 km offshore) on Line 90.0 shows a clear signal of westward propagation (Figure 3.9a). We show only the autocorrelation of alongshore velocity at 300 m since autocorrelations are similar throughout the upper 500 m and the core of the poleward flow is found near 300 m. Pairs of observations in which the later observation is further offshore (to the west) tend to be well correlated over greater separations than pairs for which the later observation is inshore. The banding pattern of the autocorrelation resembles the autocorrelation of a westward propagating sinusoid, which would itself be a two-dimensional sinusoid with a maximum at zero separation and the same wave number and frequency as the original sinusoid. This similarity suggests that we can extract the across-shore wave number, frequency, and across-shore phase speed of the westward propagating signal directly from the autocorrelation. We fit a sinusoid to the autocorrelation using least squares and weighted by the squared number of pairs of observations in each bin. The sinusoid with best fit to the observed autocovariance has an across-shore wave number of $-4.1 \times 10^{-3}$ km$^{-1}$ (244 km wavelength) and frequency of $3.7 \times 10^{-3}$ d$^{-1}$ (273 day period). A negative across-shore wave number corresponds to offshore propagation. The across-shore phase speed is then 0.90 km d$^{-1}$. A line representing westward propagation at this speed is plotted on the Hovmöller plot of vertically averaged alongshore velocity (Figure 3.5b) for comparison. Inshore of the SRR on Line 90.0 and at Line 80.0 off Point Conception, autocorrelations of observed alongshore velocity and other variables (not shown) show little evidence of westward propagation, so we limit further investigation of westward propagation to the region offshore of the SRR along Line 90.0.

The autocorrelation of simulated alongshore velocity between 200 and 550 km from shore on Line 90.0 (Figure 3.9b) is similar to the autocorrelation of observed velocities (Figure 3.9a). The westward propagating signal is again clearly evident but with longer correlation scales in the direction of propagation. The best-fit sinusoid has an across-shore wave number of $-3.0 \times 10^{-3}$ km$^{-1}$ (334 km wavelength) and a frequency of $3.1 \times 10^{-3}$ d$^{-1}$ (326 day period) with associated across-shore phase speed of 1.03 km d$^{-1}$; the simulation is producing westward propagation with slightly greater wavelength and period than observed. Although details of the simulated velocity field differ from the observed velocities, the agreement between the autocorrelations of observed and simulated velocities indicates that the model is generating the same type of variability as observed.

At the low frequencies considered here, subsurface flow in the CCS is primarily geostrophic, so, given a relatively constant barotropic flow (e.g., a reasonably steady-in-time sea level gradient), we expect the variability in observed poleward currents to be coupled to the variability in the density gradients via the thermal wind relation. For various isopycnals below the thermocline, the autocorrelations of across-shore isopycnal slope (not shown) have similar structure to the autocorrelation of alongshore velocity (Figure 3.9a). The across-shore wave number and frequency of the best-fit sinusoid to the autocorrelation of across-shore slope of the 26.5 kg m$^{-3}$ isopycnal are $-3.6 \times 10^{-3}$ km$^{-1}$ (279 km wavelength) and $3.7 \times 10^{-3}$ d$^{-1}$ (270 day period). This isopycnal is located at a depth of about 225 m in the region of the poleward current (Figure 3.8e).

The sinusoidal autocorrelations of alongshore velocity and isopycnal slope suggest the presence of a wave-like phenomenon. Analysis of properties along isopycnals provides further support for this hypothesis. The autocorrelation of depth of the 26.5 kg m$^{-3}$ isopycnal (Figure 3.10a) yet again shows evidence for westward propagation, but the autocorrelation of salinity on that isopycnal (i.e., spice) shows no evidence of westward propagation (Figure 3.10b). While isopycnal depth anomalies propagate westward, there is no associated across-shore transport of salinity along the isopycnal. If the observed westward propagation was caused by an advective process, we would expect salinity anomalies to be transported westward; since this does not occur, our observations are consistent with a wave-like phenomenon.

#### 3.3.3.2 Rossby Wave Dynamics

The observations show that variability in the alongshore currents offshore of the SRR is due to a wave-like phenomenon with across-shore wavelength of a few hundred kilometers and period nearing 1 year that propagates westward, suggesting that Rossby wave dynamics may be important. To determine whether the observed westward propagation is consistent with Rossby wave dynamics, we compare the observed wave number and frequency with the theoretical Rossby wave dispersion relation. Since we are only considering westward propagation offshore of the SCB and SRR where the water depth generally exceeds 2000 m (Figure 3.1) and we will show in section 3.3.3.4 that the main forcing region is within the SCB, we consider only free Rossby waves dynamics in the absence of topographic effects.

In a coordinate system with the $x$ axis rotated by an angle $\alpha$ counterclockwise from east, the flat-bottom, free, baroclinic Rossby wave dispersion relation is

$$\omega = -\frac{\beta(k\cos\alpha - l\sin\alpha)}{k^2 + l^2 + \frac{f_0^2}{c_n^2}}, \tag{3.1}$$

where $\omega$ is the angular frequency, $k$ is the across-shore wave number, $l$ is the alongshore wave number, $f_0$ is the local Coriolis parameter, $\beta$ is the local rate of change of the Coriolis parameter, and $c_n$ is the speed of the $n$th gravity wave mode [*Gill*, 1982, equation 6.11.18]. For Line 90.0, $\alpha = 26°$. To estimate $c_n$ in the region, we combine glider observations with World Ocean Atlas 2005 climatologies of temperature and salinity [*Antonov et al.*, 2006; *Locarnini et al.*, 2006] to produce a full depth profile of the buoyancy frequency. We make a similar calculation of $c_n$ in the model by using the simulated stratification.

Since we observe only the across-shore component of the wave number, we must make some simplifications to (3.1) for comparison to the observations. For

Rossby waves traveling directly along the survey line, and roughly perpendicular to the coast, we have $l = 0$, and the dispersion relation is

$$\omega = -\frac{\beta k \cos\alpha}{k^2 + \frac{f_0^2}{c_n^2}}. \tag{3.2}$$

The dispersion relation (3.1) also provides an upper limit for the frequency $\omega$ at any given across-shore wave number $k$. For $\alpha = 0$, that limit is a wave propagating due west with $l = 0$, but in our rotated coordinate system the alongshore wave number that maximizes the frequency varies with the across-shore wave number. The case for $l = 0$ (3.2) and the maximum frequency case are shown for the first three baroclinic modes in Figure 3.11.

The wave number and frequency of the westward propagation of both the observed and simulated alongshore velocity and the observed isopycnal slope agree well with the theoretical Rossby wave dispersion relation (Figure 3.11). The observed frequencies lie between the dispersion curve for a first-mode baroclinic wave moving along the observation line (3.2) and the curve for a first-mode wave with maximum frequency, and they are far removed from the curves corresponding to the higher baroclinic modes. The across-shore wave number and frequency of westward propagation in the numerical simulation, though somewhat smaller than observed, are similarly consistent with first-mode baroclinic Rossby wave dynamics (Figure 3.11). The dispersion curves for the model are slightly different from those for the observed fields due to minor differences in stratification in the model.

#### 3.3.3.3 Alongshore Wave Number and Direction of Propagation

Our observations cannot resolve the alongshore component of the wave number ($l$). However, if we assume that first-mode baroclinic Rossby dynamics accurately describe the westward propagation, then (3.1) provides a means of calculating $l$. Since (3.1) is quadratic in $l$, it gives two solutions for each observed value of $k$ and $\omega$, but one solution gives wavelengths of 900 km or longer. Since the westward propagation was not apparent off Point Conception, only 225 km up the coast, we consider only the larger solution for $l$, which gives shorter wavelengths. For the values of $k$ and $\omega$ corresponding to observed alongshore velocities and across-shore isopycnal slopes, the values of $l$ are $4.5 \times 10^{-3}$ km$^{-1}$ (221 km wavelength) and $3.9 \times 10^{-3}$ km$^{-1}$ (254 km wavelength), respectively. The resulting vector wave numbers for both alongshore velocity and isopycnal slope are oriented towards 292° true. The same calculation using modeled velocity at 300 m gives an alongshore wave number of $6.7 \times 10^{-3}$ km$^{-1}$ (149 km wavelength) and a direction of propagation of 310° true.

The numerical simulation provides velocity information at all locations, so we can investigate the direction of propagation in the model without assuming anything about the dynamics by calculating velocity autocorrelations over a two-dimensional region. For the simulated currents at 300 m and in the region $\left[\begin{array}{cc} 122°\text{W} & 119°\text{W} \end{array}\right] \times \left[\begin{array}{cc} 30°\text{N} & 33°\text{N} \end{array}\right]$, we calculate the autocorrelation of velocity as

$$\mathrm{cor}(\Delta x, \Delta y, \Delta t) = \frac{\langle \vec{u}(x,y,t) \cdot \vec{u}(x+\Delta x, y+\Delta y, t+\Delta t) \rangle_{x,y,t}}{\langle \vec{u}(x,y,t) \cdot \vec{u}(x,y,t) \rangle_{x,y,t}}. \tag{3.3}$$

Slices through the resulting autocorrelation matrix at fixed values of $\Delta t$ (Figure 3.12) show the area of highest correlation moving nearly due west with increasing temporal separation, in reasonable agreement with the 292° direction of propagation estimated from the observations with the assumption of first-mode baroclinic Rossby wave dynamics.

#### 3.3.3.4 Source of Westward Propagation

The observed westward propagation offshore of the SRR along Line 90.0 is consistent with density perturbations propagating westward from the SCB, and we now consider the source of those density perturbations. *Di Lorenzo* [2003] used ROMS to show that the combination of alongshore wind stress near the coast and positive wind stress curl within the SCB raised isopycnals within the SCB in spring. The relaxation of the wind forcing in summer allowed the density anomalies to propagate westward when model dynamics included the $\beta$ effect. Glider observations of the anomalous depth of the 26.5 kg m$^{-3}$ isopycnal show a similar uplift of the isopycnal in spring of each year along Line 90.0 with westward propagation of the density anomaly in the summer and fall (Figure 3.13b). Isopycnals shoal in spring at Point Conception, but there is no apparent westward propagation of the density anomalies in the summer and fall (Figure 3.13a). The timing of the setup of density anomalies within the SCB is then consistent with the annually periodic wind forcing suggested by *Di Lorenzo* [2003].

In the absence of wind observations with sufficient coverage of the SCB, we turn to the numerical simulation and its adjusted wind stress field. Alongshore winds at Line 90.0 (not shown) are always equatorward with a maximum 200–400 km offshore and near zero velocity at the coast. Wind stress curl is positive inshore of the maximum with strongest positive curl inshore of the SRR (Figure 3.14a). Wind stress curl in the SCB is strongest in April–May (Figure 3.14b). Annual maxima in simulated wind stress curl within the SCB lead the observed shoaling of isopycnals within the SCB by about two months (Figure 3.14b). When the wind stress curl relaxes, isopycnal depth anomalies begin to propagate westward. The observed across-shore wave numbers (section 3.3.3.1) and the alongshore wave numbers estimated by assuming Rossby wave dynamics (section 3.3.3.3) give a spatial scale roughly equivalent to the size of the SCB. For forcing concentrated within the SCB as indicated by modeled wind stress curl, the resulting Rossby waves would be expected to have spatial scales similar to the size of the SCB [*Debnath*, 2007].

#### 3.3.3.5 Rossby Waves or Eddies?

Recent work by *Chelton et al.* [2007] and *Chelton et al.* [2011] using SSH observations has shown that much ocean variability that had been attributed to linear Rossby waves [e.g., *Chelton and Schlax*, 1996] is actually due to nonlinear eddies that propagate westward with speeds close to the baroclinic Rossby wave speeds. Although westward propagating features in SSH typically have phase speeds faster than permitted by linear theory [*Chelton and Schlax*, 1996], the phase speeds that we observe (0.90 km $\mathrm{d}^{-1}$ or 0.01 m $\mathrm{s}^{-1}$) and model (1.03 km $\mathrm{d}^{-1}$) are within the range allowed by the linear theory (Figure 3.11). The observed westward propagating features do not transport salinity along isopycnals (Figure 3.10), but nonlinear eddies with closed contours that form near the coast and move offshore across the background salinity gradient (e.g., Figure 3.8) would produce across-shore salinity transport. Though these findings are consistent with linear dynamics, the phase speeds are smaller than observed mean velocities in the region (Figure 3.4), so we may expect nonlinear effects to also be important, particularly as features evolve and move out of our observation region.

## 3.4 Conclusions

We combine long-term, high-resolution observations from a network of autonomous underwater gliders in the southern California Current System with a regional, numerical state estimate. This novel technical framework allows us to (1) characterize the narrow poleward flows in the region, particularly the recently detected poleward current offshore of the SRR; (2) show that the poleward current offshore of the SRR propagates westward; and (3) demonstrate that the observed westward propagation is largely consistent with linear Rossby wave dynamics.

We observe persistent poleward flows in three areas: within 100 km of the coast at Point Conception, inshore of the SRR within the SCB, and offshore of the SRR. We account for variability in the strength and position of poleward flows in the CCS by constructing averages in jet-following coordinates for each region of poleward flow. These jet-following averages reveal the poleward flows to be narrower and faster than suggested by long-term mean sections of alongshore flow. Mean poleward velocities are on the order of 0.1 m $s^{-1}$ in each region. Contrary to previous work, we find no distinction between subsurface and surface poleward flow within the SCB and, consequently, no support for separate naming of surface and subsurface currents. We show that the poleward current offshore of the SRR is deeper, denser, and saltier than the CU at Point Conception and that much of the poleward transport through Line 90.0 does not reach Line 80.0, so we conclude that the poleward current offshore of the SRR is generally not continuous with the CU at Point Conception.

We find that the poleward current offshore of the SRR propagates westward, unlike the poleward flows at Point Conception and within the SCB. This westward propagation is apparent in both the velocity and density fields since the two are linked by the dominant geostrophic dynamics. Without the high-spatial- and -temporal-resolution observations provided by the network of gliders, we could not have detected these subsurface westward propagating signals.

The across-shore wave number, frequency, and phase speed of the westward propagation and the lack of westward transport of salinity along isopycnals are consistent with first-mode baroclinic Rossby wave dynamics. Observed isopycnal depth anomalies and adjusted wind stress from the numerical simulation show that local winds during spring and early summer raise isopycnals within the SCB. When these winds relax, density anomalies and the poleward current propagate westward. While consistent with linear dynamics, the relatively slow speed of propagation suggests that nonlinear effects are likely important.

Poleward undercurrents are a ubiquitous feature of midlatitude eastern boundary current systems, but the details of the flows vary by region [*Neshyba et al.*, 1989]. By virtue of its location along the west coast of the United States, the CCS is by far the best observed eastern boundary current system. Without similarly thorough observations in other eastern boundary current systems, we can only speculate about the applicability of our findings to other regions. Typical poleward undercurrents in other eastern boundary current systems could be expected to be on the order of a few 10s of km wide with speeds near 0.1 m $s^{-1}$ as found in the CCS. Since eastern boundary current systems generally experience seasonally modulated wind forcing [*Bakun and Nelson*, 1991], westward propagation of density anomalies that subsequently affects the position of undercurrents may be found in other regions. The CCS and other eastern boundary current systems support highly productive ecosystems and associated fisheries [*Botsford et al.*, 2006]. Strong and variable alongshore currents may be important to the distribution, dispersal, and retention of organisms in these systems. We anticipate that observations from networks of autonomous vehicles and continually improving numerical simulations will be essential to improving our understanding of eastern boundary current systems and their associated ecosystems.

*Acknowledgments.* Spray glider observations could not have been completed without the support of the Instrument Development Group at the Scripps

Institution of Oceanography and the Southern California Coastal Ocean Observing System (SCCOOS). Francisco Chavez (MBARI) assisted with glider observations along Line 66.7. We thank Dudley Chelton (OSU) for helpful comments on the manuscript. We gratefully acknowledge funding from the Gordon and Betty Moore Foundation, the Coastal Ocean Currents Monitoring Project (COCMP), and NOAA. Modeling and glider observations on Lines 66.7 and 90.0 are part of the Consortium on the Ocean's Role in Climate (CORC) program. R. E. Todd was partially supported by an Achievement Rewards for College Scientists (ARCS) scholarship. Chapter 3, in full, is a reproduction of the material as it appears in *Todd, Rudnick, Mazloff, Davis, and Cornuelle* [2011a], *J. Geophys. Res., 116*, C02026. The dissertation author was the primary investigator and author of this work.

## Appendix 3.A Accuracy of Vertically Averaged Current Measurements From Gliders

Glider-based measurements of vertically averaged currents are used to reference ADP-derived shears and geostrophic shears throughout this analysis, so the accuracy of those measurements is critical to our results. For each glider dive, the true vertically averaged water velocity relative to the earth, $\tilde{u}_w$, is related to the true vertically averaged glider velocity over the earth, $\tilde{u}_g$, and the true vertically averaged glider velocity through the water, $\tilde{u}_r$, by

$$\tilde{u}_w = \tilde{u}_g - \tilde{u}_r, \tag{3.4}$$

where we have used complex variables for velocities with the eastward velocity as the real component and the northward velocity as the imaginary component. We denote our measurements of these three quantities as $\hat{u}_w$, $\hat{u}_g$, and $\hat{u}_r$. Our measurement of the glider's velocity over the earth, $\hat{u}_g$, is based on GPS measurements at the beginning and end of each dive that have position accuracy of 10 m. Our measurement of horizontal glider velocity through the water, $\hat{u}_r$, is based on an estimated angle of attack from a model of glider flight [see *Sherman et al.*, 2001] and integrating measured heading, pitch, and vertical velocity over each dive, so it may be subject to accumulated errors in magnitude and direction. Since the glider's vertical velocity is not perfectly constant, our measurements $\hat{u}_w$, $\hat{u}_g$, and $\hat{u}_r$ are temporal averages during each dive rather than depth averages.

Previous authors have considered the main sources of error in calculating glider displacement through the water during a dive (e.g., vertical ocean velocities and errors in the model of glider flight) and found these factors to contribute to errors in vertically averaged current estimates of $O(0.01 \text{ m s}^{-1})$ for a single dive, with accuracy increasing when many dives are considered [*Davis et al.*, 2002; *Gourdeau et al.*, 2008]. With the exception of two deployments on Line 80.0 that failed to return complete data sets for detailed postdeployment calibration, all glider deployments used in this analysis have had heading-dependent compass calibrations applied, eliminating the largest source of error in the vertically averaged currents discussed by *Gourdeau et al.* [2008]. *Eriksen et al.* [2001] found a strong linear relationship with gain near unity between $\hat{u}_g$ and $\hat{u}_r$ for a Seaglider deployment in a region with relatively weak currents, suggesting that the current estimates were credible.

The 3 year record of observations used in this analysis allows us to determine the accuracy of measurements of glider velocity through the water, $\hat{u}_r$, using a technique analogous to the ADCP calibration method described by *Pollard and Read* [1989]. We will assume that true water velocity, $\tilde{u}_w$, is constant on either side of a turn by the glider. Our estimated water velocity, $\hat{u}_w$, however, may change because of errors in $\hat{u}_r$. To account for these errors, we find a complex factor $\gamma$ that, when applied to $\hat{u}_r$, makes $\hat{u}_w$ constant across glider turns. We write

$$\hat{u}_w = \hat{u}_g - \gamma \hat{u}_r. \tag{3.5}$$

We consider glider measurements around 39 offshore turnarounds to determine $\gamma$. We use offshore turnarounds ($> 350$ km offshore) because they are in deep water where the glider dives to 500 m and, consequently, spends a smaller fraction of the dive flying poorly while leaving the surface and turning at the bottom of the profile. For each turnaround, we average $\hat{u}_w$, $\hat{u}_g$, and $\hat{u}_r$ over the last eight dives (about 1 day) approaching the turnaround to get $\bar{u}_{w1}$, $\bar{u}_{g1}$, and $\bar{u}_{r1}$, respectively. Similarly, we average over the first eight dives leaving the turnaround to get $\bar{u}_{w2}$, $\bar{u}_{g2}$, and $\bar{u}_{r2}$. Writing $\bar{u}_{w1} = \bar{u}_{w2}$ and using (3.5), our estimate of $\gamma$ for each turnaround is

$$\gamma = \frac{\bar{u}_{g1} - \bar{u}_{g2}}{\bar{u}_{r1} - \bar{u}_{r2}}. \tag{3.6}$$

Excluding a single turnaround for which the water velocity appears to have changed significantly between the outbound and inbound legs, values of $\gamma$ are clustered about a mean of $1.0154-0.0008i$ with a standard deviation of 0.0413. The amplitude and angle of the mean value of $\gamma$ are 1.0154 and -0.0424°, respectively. For a typical glider speed through the water of 0.25 m $\text{s}^{-1}$, average bias in $\hat{u}_r$ would be less than $4 \times 10^{-3}$ m $\text{s}^{-1}$. If all of the magnitude bias is attributed to error in the assumed angle of attack, then our assumed angle of attack of 3° is too large by 0.28°. The standard deviation of $\gamma$ suggests an uncertainty in $\hat{u}_r$ of 0.01 m $\text{s}^{-1}$, in agreement with *Davis et al.* [2002], and an uncertainty in the true angle of attack of about 0.75°.

Increasing fouling during a deployment may affect the angle of attack of the glider. As fouling increases drag and disrupts flow over the glider, we would expect the glider's angle of attack to increase and its vertical velocity to decrease, both of which cause its forward speed through the water to slow. Changes in vertical velocity are measured, but changes in angle of attack are not accounted for in our estimate of $\hat{u}_r$. For most deployments, the glider completes four transects, so two offshore turnarounds are available from the same deployment. The difference between values of $\gamma$ from the first and second offshore turnaround of each deployment gives some indication of the influence of fouling. For 16 deployments with two offshore turnarounds each, the mean change in $\gamma$ between the first and second turnaround is $-0.0263+0.0015i$. Attributing all of the change in $\gamma$ between turnarounds to changes in angle of attack gives an increase in angle of attack of 0.50° between turnarounds. Directional bias in $\hat{u}_r$ remains negligible.

Since the mean value of $\gamma$ found in this analysis is less than a standard deviation from unity, we have not applied any correction to vertically averaged velocity estimates. Any magnitude bias in $\hat{u}_r$ should result in errors in the along-track (across-shore) component of $\hat{u}_w$ which are not the focus of this analysis. In the mean over many sections, any bias should average to zero because the gliders survey in both the onshore and offshore directions.

## Appendix 3.B Horizontal Currents From Glider-Mounted Acoustic Doppler Profilers

Each Spray glider deployed in the CCS is equipped with a custom Sontek Argonaut 750 kHz acoustic Doppler profiler (ADP) mounted in the tail. The instrument is oriented such that an upward pitch at the nominal 17° ascent angle and zero roll result in the central axis of the ADP pointing downward so that range bins are depth bins. The three beams of the instrument are aimed 25° off the central axis with one beam looking forward along the long axis of the glider.

The ADP collects a 16 ping ensemble average every 4 m in the vertical during the ascending portion of a dive (Figure 3.B1a). Each ensemble average provides measurements of along-beam speed and return amplitude in five measurement cells for each beam. Each measurement cell extends 4 m in the vertical. For the settings used in the CCS, the first measurement cell is centered 10 m below the glider. The sampling parameters are such that cells from successive ensembles should align as indicated in Figure 3.B1a.

Glider ADP measurements undergo several processing and quality control steps before profiles of ocean velocity are estimated. We calculate the depth of each measurement cell from records of the glider's depth, pitch, and roll during each 16 ping ensemble. Data from ensembles when the glider is pitched or rolled enough to displace measurement cells from their nominal alignment are excluded from further processing. The ADP can be used as an altimeter during the descending portion of a dive; data in cells that are deeper than the altimeter-derived bottom depth are excluded. Along-beam speeds are used to calculate eastward ($u$), northward ($v$), and upward speeds relative to the glider by successive rotations using records of the glider's pitch, roll, and heading during each ensemble average. Velocities relative to the glider that exceed 0.75 m $\text{s}^{-1}$ are considered to be erroneous since the speed of the glider through the water is approximately 0.25 m $\text{s}^{-1}$ and the range of the ADP is too small (about 20 m) to expect very large relative velocities. We also exclude measurements for which the signal-to-noise ratio is less than 1.0.

Transducer failures have occurred during some deployments. We use the average return strength for each beam during each profile to detect failures of transducers. Any sudden drop in return strength of one beam relative to the other two indicates failure of the respective transducer, and data from that beam are not used in further calculations. The loss of data from one or more beams prohibits calculation of a velocity profile. Transducer failures are the primary cause of the missing ADP velocity profiles shown in Figure 3.2.

We let $N$ be the number of ensemble averages during the ascending portion of a glider dive; the sampling geometry defines a set $N+4$ estimation bins (Figure 3.B1b). Measurements in the shallowest cell (cell 1) for each ensemble are not used because of ringing of the ADP transducers, so up to four measurements contribute to the estimate in each bin. The exclusion of data from cell 1 results in no data in the uppermost sampling bin, so we only estimate velocity in the $N + 3$ bins with data. The number of measurements contributing to the estimate in a bin is reduced if measurements are excluded during quality control. Because the glider sampling pattern is not perfectly regular, the depth of a given estimation bin is defined to be the mean depth of each good measurement in the bin.

The glider-mounted ADP functions similarly to a lowered acoustic Doppler current profiler (LADCP) deployed from from a research vessel, and our calculation of ocean velocity profiles from the glider-mounted ADP data is based on the LADCP data processing scheme presented by *Visbeck* [2002]. For each valid measurement of horizontal water velocity relative to the glider, $(u, v)_r$, we have an equation

$$(u, v)_r = (u, v)_w - (u, v)_g, \tag{3.7}$$

where $(u, v)_w$ is the ocean velocity at the location of the measurement cell, and $(u, v)_g$ is the velocity of the glider at the same moment. (Note that here the subscript $r$ refers to water velocity relative to the glider, which is the opposite of the glider's velocity through the water used in Appendix A.) Both terms on the right hand side of equation (3.7) are unknown. There are $N$ unknown glider velocities (one for each sampling depth), and $N+3$ unknown water velocities (one for each estimation bin with data). Excluding data from the shallowest cell for each ensemble, we have at most $4N$ equations of the form of (3.7). This system of equations can be written as a matrix equation of the form $\mathbf{Gm} \cong \mathbf{d}$, where

$$\mathbf{d} = \begin{bmatrix} u_{1,2} & u_{1,3} & u_{1,4} & u_{1,5} & u_{2,2} & \cdots & u_{2,5} & \cdots & u_{N,5} \end{bmatrix}^{\mathrm{T}} \tag{3.8}$$

is the vector of observations of speed relative to the glider in one direction,

$$\mathbf{m} = \left[ \begin{array}{ccc|ccc} u_{g,1} & \cdots & u_{g,N} & u_{w,2} & \cdots & u_{w,N+4} \end{array} \right]^{\mathrm{T}} \tag{3.9}$$

is the vector of unknown glider and water velocities in that direction, and

$$\mathbf{G} = \left[ \begin{array}{ccccc|ccccccc} -1 & 0 & 0 & \cdots & 0 & 1 & 0 & 0 & 0 & 0 & \cdots & 0 \\ -1 & 0 & 0 & \cdots & 0 & 0 & 1 & 0 & 0 & 0 & \cdots & 0 \\ -1 & 0 & 0 & \cdots & 0 & 0 & 0 & 1 & 0 & 0 & \cdots & 0 \\ -1 & 0 & 0 & \cdots & 0 & 0 & 0 & 0 & 1 & 0 & \cdots & 0 \\ 0 & -1 & 0 & \cdots & 0 & 0 & 1 & 0 & 0 & 0 & \cdots & 0 \\ 0 & -1 & 0 & \cdots & 0 & 0 & 0 & 1 & 0 & 0 & \cdots & 0 \\ 0 & -1 & 0 & \cdots & 0 & 0 & 0 & 0 & 1 & 0 & \cdots & 0 \\ 0 & -1 & 0 & \cdots & 0 & 0 & 0 & 0 & 0 & 1 & \cdots & 0 \\ 0 & 0 & -1 & \cdots & 0 & 0 & 0 & 1 & 0 & 0 & \cdots & 0 \\ \vdots & \vdots & \vdots & \ddots & \vdots & \vdots & \vdots & \vdots & \vdots & \vdots & \ddots & \vdots \\ 0 & 0 & 0 & \cdots & -1 & 0 & 0 & 0 & 0 & 0 & \cdots & 1 \end{array} \right] \tag{3.10}$$

is the matrix of coefficients when all measurements are good. When all measurements are used, $\mathbf{d}$ has dimensions $4N \times 1$ and $\mathbf{G}$ has dimensions $4N \times (N+N+3)$. Loss of measurements reduces only the number of equations in the system, so that, in practice, $\mathbf{d}$ and $\mathbf{G}$ have at most $4N$ rows, but $\mathbf{m}$ always has dimension $(N+N+3) \times 1$.

Though the number of equations exceeds the number of unknowns, we still require additional information to solve the system of equations since the ADP data alone can only provide the baroclinic portion of the ocean velocity [*Visbeck*, 2002]. We use the estimate of vertically averaged water velocity during each dive (Appendix 3.A) to reference the ADP shear. This measurement of vertically averaged velocity is valid from the surface to the maximum depth reached by the glider, a range that is offset from the sampling range of the ADP since the ADP samples below the glider. We account for this offset in two ways. First, we exclude ADP velocity estimates in the seven bins ($i_{\text{bin}} = N-2, \ldots, N+4$) that are deeper than the glider's maximum depth (Figure 3.B1b) from the constraint. Second, we assume that the near-surface portion of the water column that is not sampled by the ADP has uniform velocity. Under this assumption, we weight the uppermost estimation bin as if it extended to the surface in the vertically averaged velocity constraint. This constraint adds the row

$$\left[\begin{array}{ccc|cccccc} 0 & \cdots & 0 & \Delta z_2 & \cdots & \Delta z_{N-3} & 0 & \cdots & 0 \end{array}\right], \tag{3.11}$$

to the matrix $\mathbf{G}$. The $\Delta z_i$ are the vertical extents of the velocity bins, which are approximately 4 m, except for $\Delta z_2$ which is larger as discussed above. The corresponding element added to $\mathbf{d}$ is $U \sum_{i=2}^{N-3} \Delta z_i$, where $U$ is the estimated vertically averaged velocity. Since the ADP measures shear only on the ascending portion of each dive and vertically averaged velocity is based on the glider's displacement throughout the entire dive, there is a mismatch in location and time between the shear profile and the barotropic constraint that is unaccounted for. At the 30 km and larger scales considered in this analysis, any errors due to this mismatch should not be significant. The agreement between ADP-derived currents after 30 h filtering and geostrophic currents (e.g., Figure 3.3) suggests that the induced errors are small.

Ideally, the overdetermined system $\mathbf{Gm} \cong \mathbf{d}$ is now solvable by least squares techniques. However, the loss of equations due to bad measurements can make the system ill conditioned. To further constrain the problem and reduce noise in the solution, we apply the curvature-minimizing smoothness constraint of *Visbeck* [2002] to the horizontal ocean velocities and horizontal glider velocities. These constraints add $N+1$ and $N-2$ additional equations to the system, respectively.

The additional rows added to $\mathbf{G}$ are

$$w \times \left[\begin{array}{ccc|cccccc} 0 & \cdots & 0 & -1 & 2 & -1 & 0 & \cdots & 0 \\ 0 & \cdots & 0 & 0 & -1 & 2 & -1 & \cdots & 0 \\ \vdots & \ddots & \vdots & \vdots & \vdots & \vdots & \vdots & \ddots & \vdots \\ 0 & \cdots & 0 & 0 & 0 & 0 & 0 & \cdots & -1 \end{array}\right], \tag{3.12}$$

and

$$w \times \left[\begin{array}{cccccc|ccc} -1 & 2 & -1 & 0 & \cdots & 0 & 0 & \cdots & 0 \\ 0 & -1 & 2 & -1 & \cdots & 0 & 0 & \cdots & 0 \\ \vdots & \vdots & \vdots & \vdots & \ddots & \vdots & \vdots & \ddots & \vdots \\ 0 & 0 & 0 & 0 & \cdots & -1 & 0 & \cdots & 0 \end{array}\right], \tag{3.13}$$

where $w$ is a weight that determines the degree of smoothing. We choose $w = 5$ to produce sufficiently smooth velocity profiles. The data vector $\mathbf{d}$ gains $2N - 1$ rows of zeros since we seek to minimize curvature in the solution.

We then solve the system for the unknown glider velocities and horizontal ocean velocities using least squares techniques to minimize the $L_2$ norm of $\mathbf{Gm}-\mathbf{d}$. The solution is

$$\mathbf{m} = \left(\mathbf{G}^{\mathrm{T}}\mathbf{G}\right)^{-1} \mathbf{G}^{\mathrm{T}}\mathbf{d}. \tag{3.14}$$

**Table 3.1**: Model Parameters Used in the Forward Run and Adjoint

| Parameter | Forward Run | Adjoint |
|---|---|---|
| Vertical viscosity ($m^2$ $s^{-1}$) | $1 \times 10^{-4}$ | $1 \times 10^{-4}$ |
| Horizontal viscosity ($m^2$ $s^{-1}$) | $1 \times 10^{2}$ | $1 \times 10^{3}$ |
| Biharmonic horizontal viscosity ($m^4$ $s^{-1}$) | $1 \times 10^{9}$ | $1 \times 10^{9}$ |
| Quadratic bottom drag | $1 \times 10^{-3}$ | $1 \times 10^{-3}$ |
| Vertical diffusivity ($m^2$ $s^{-1}$) | $1 \times 10^{-5}$ | $1 \times 10^{-5}$ |
| Horizontal diffusivity ($m^2$ $s^{-1}$) | $1 \times 10^{0}$ | $1 \times 10^{0}$ |

**Table 3.2**: Mean Volume Transports Through Line 80.0, Line 90.0, and the Section Between Stations 80.100 and 90.100 From Observations and Numerical Simulation[a]

| Section | Line 80.0 | Line 90.0 | 80.100-90.100 |
|---|---|---|---|
| Observed transport, 10/2006-11/2009 (Sv) | $-1.0 \pm 0.7$ | $3.7 \pm 1.3$ | N/A |
| Observed transport, 1/2007-7/2009 (Sv) | $-1.1 \pm 0.7$ | $2.7 \pm 0.7$ | N/A |
| Simulated transport, 1/2007-7/2009 (Sv) | $-0.9 \pm 0.5$ | $1.0 \pm 0.4$ | $1.9 \pm 0.3$ |

[a] Values are reported as the mean plus or minus standard error. Estimates of standard errors are based on the integral timescale for each transport. Positive transports through Lines 80.0 and 90.0 are poleward. Positive transport through the section between stations 80.100 and 90.100 is offshore.

**Table 3.3**: Mean Position, Width, and Volume Transport for the Poleward Jets Off Point Conception on Line 80.0, Within the SCB on Line 90.0, and Offshore of the SRR on Line 90.0[a]

| Region | Point Conception | Offshore SCB | Within SCB |
|---|---|---|---|
| Position (km) | 43±4 | 282±12 | 76±6 |
| Width (km) | 36±3 | 55±8 | 31±3 |
| Volume Transport (Sv) | 2.0±0.2 | 2.9±0.5 | 1.4±0.3 |

[a] Values are reported as the mean plus or minus standard error for each quantity with units noted. Estimates of standard errors are based on the integral timescale for each quantity.

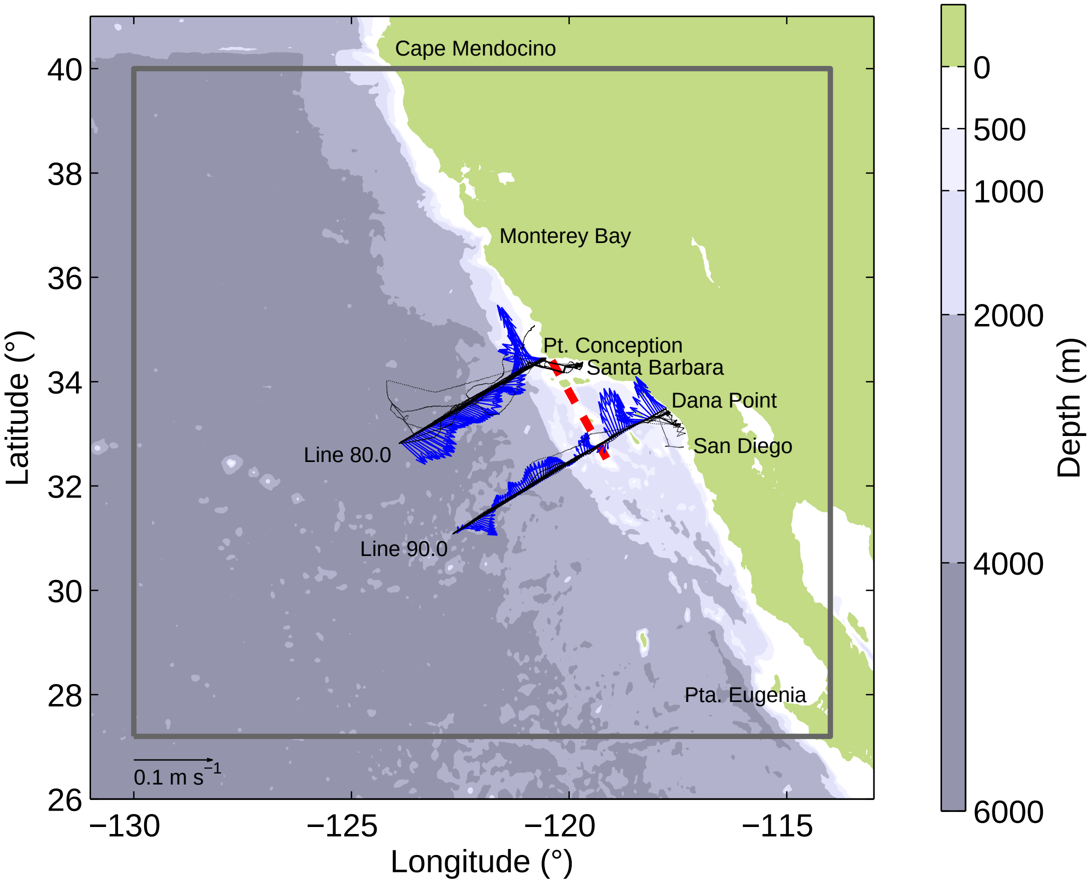

**Figure 3.1**: Bathymetry of the region considered in this analysis (color) with tracks of glider deployments along CalCOFI Lines 80.0 and 90.0 (black) and mean observed vertically averaged currents over the upper 500 m (blue vectors). A scale vector is given in the lower left. The grey box denotes the domain of the numerical model. The dashed red line denotes the Santa Rosa Ridge, which is the offshore boundary of the Southern California Bight.

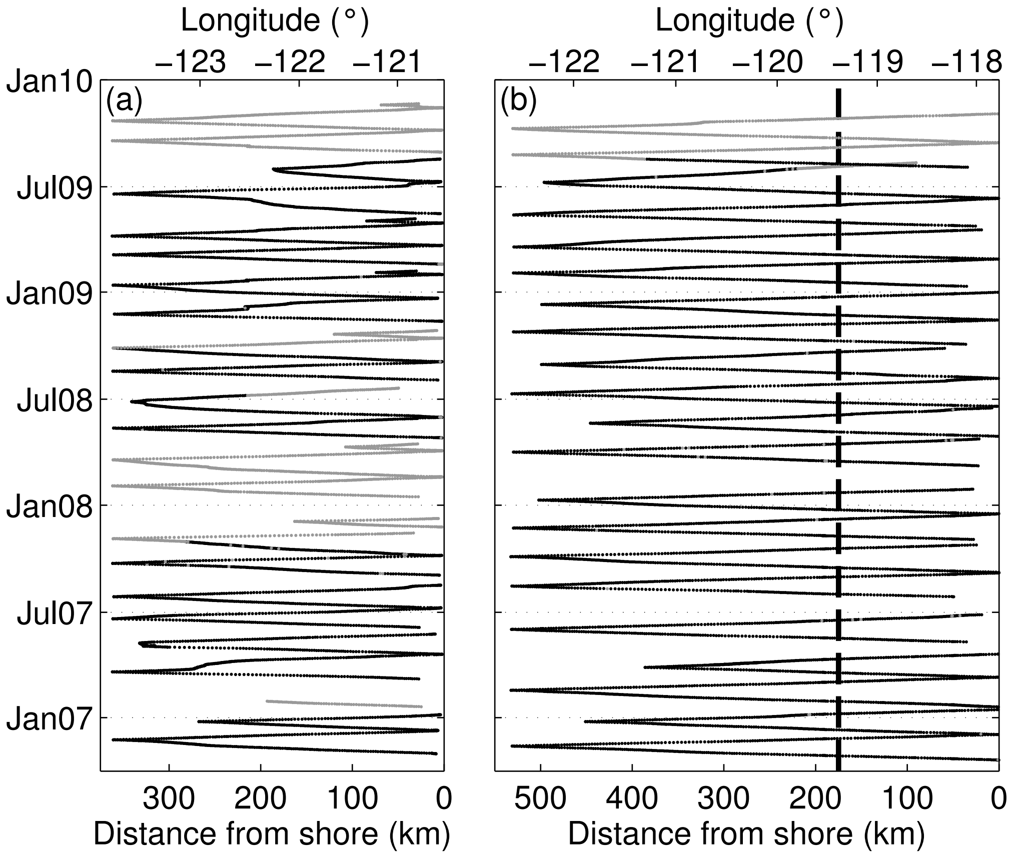

**Figure 3.2**: Across-shore and temporal sampling pattern along CalCOFI Lines (a) 80.0 and (b) 90.0. Each point denotes the location of a glider profile. Black points indicate profiles with valid ADP-derived current estimates; profiles without ADP-derived current estimates are grey. The dashed black line in Figure 3.2b shows the location of the Santa Rosa Ridge.

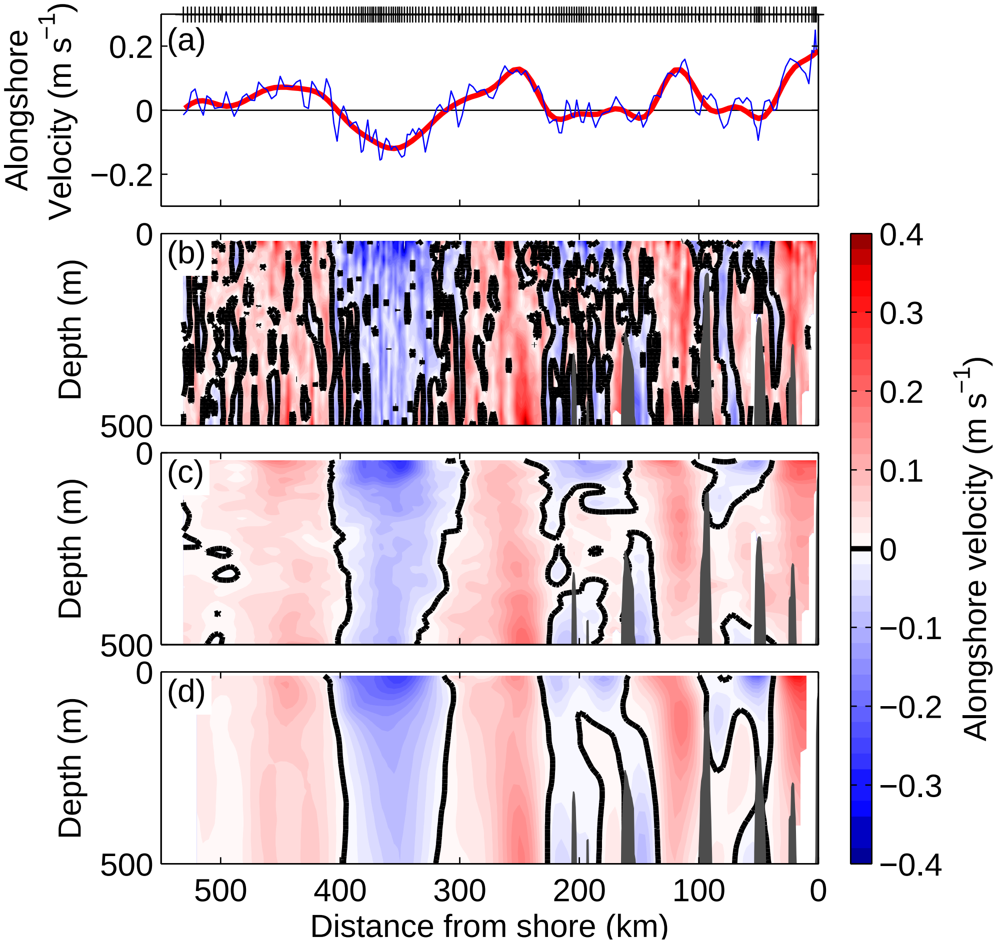

**Figure 3.3**: Alongshore velocities from an inshore-to-offshore transect along Line 90.0 from 18 June 2008 to 10 July 2008. (a) Vertically averaged alongshore velocities for each dive used to reference ADP velocities (blue) and objectively mapped velocities used to reference geostrophic velocities (red). (b) ADP-derived velocities with no temporal smoothing. (c) The same ADP-derived velocities after filtering with a 30 h Gaussian in the time domain. (d) Geostrophic velocities. Tick marks on the uppermost horizontal axis indicate the locations of individual profiles. Positive (negative) velocities are poleward (equatorward). Dark grey shading (Figures 3.3b–3.3d) represents the bathymetry along Line 90.0.

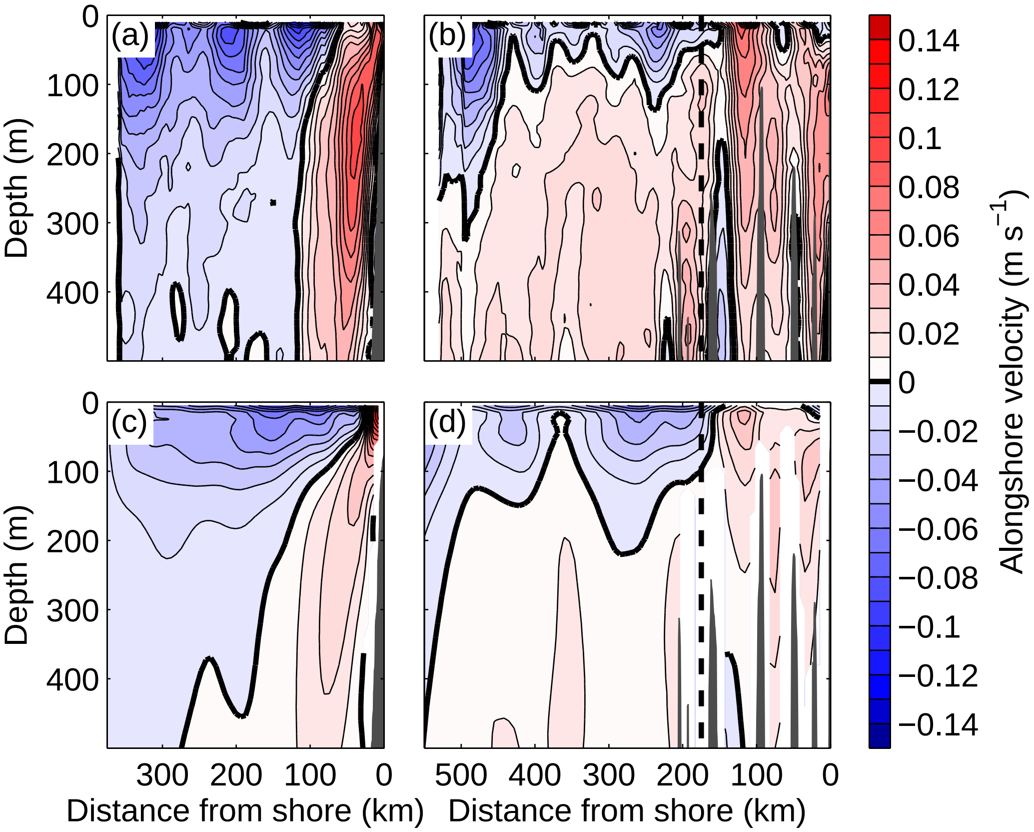

**Figure 3.4**: (a and b) Mean alongshore currents from all glider observations and (c and d) the numerical simulation along CalCOFI Line 80.0 (Figures 3.4a and 3.4c) and CalCOFI Line 90.0 (Figures 3.4b and 3.4d). Contours are drawn every 0.01 m s$^{-1}$ with the zero contour given in bold. Positive velocities are poleward. The dashed line at 175 km along Line 90.0 (Figures 3.4b and 3.4d) denotes the location of the Santa Rosa Ridge. Dark grey shading represents the bathymetry along the survey lines. The mean in Figures 3.4a and 3.4b is over the period October 2006 to November 2009 while the mean in Figures 3.4c and 3.4d is over the period January 2007 to July 2009.

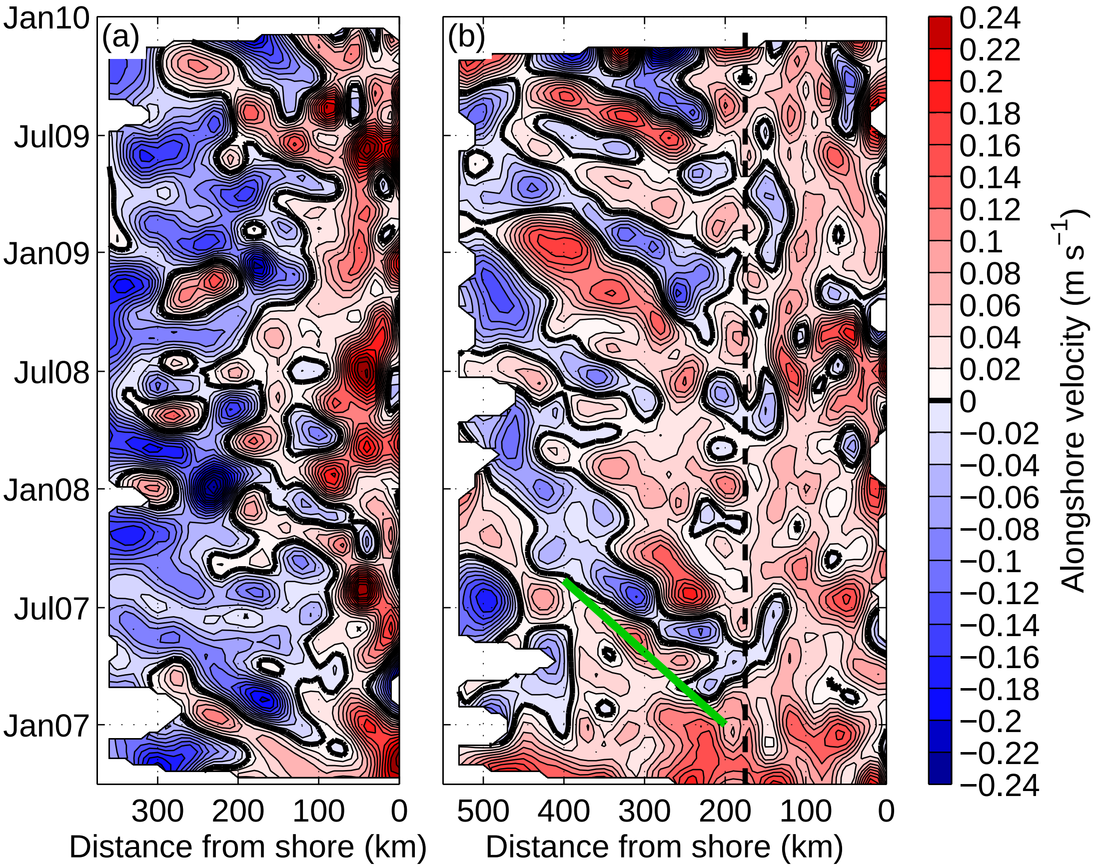

**Figure 3.5**: Hovmöller plots of vertically averaged alongshore current in the upper 500 m at (a) Line 80.0 and (b) Line 90.0. Observations were objectively mapped using a Gaussian covariance with decorrelation scales of 30 km and 60 days in the across-shore direction and time, respectively. The noise-to-signal ratio was set to 0.1. Regions with mean square errors exceeding 20% are masked. Contours are drawn every 0.02 m s$^{-1}$ with the zero contour given in bold. Positive velocities are poleward. The dashed line at 175 km along Line 90.0 (Figure 3.5b) denotes the location of the Santa Rosa Ridge. The bold green line in Figure 3.5b indicates a westward propagation speed of 0.90 km d$^{-1}$ as calculated in section 3.3.3.1.

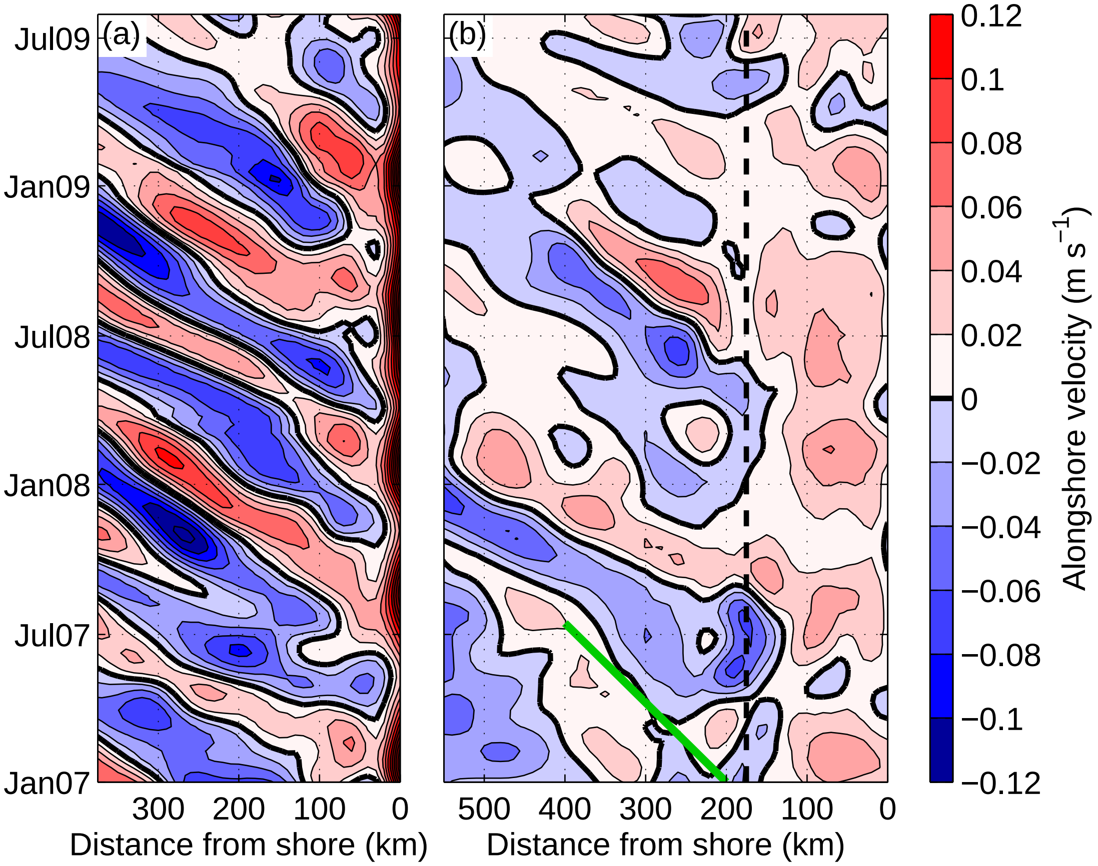

**Figure 3.6**: Hovmöller plots of vertically averaged alongshore current in the upper 500 m at (a) Line 80.0 and (b) Line 90.0 from the numerical simulation. Six-day averages from the model are objectively mapped as in Figure 3.5. Note the difference in the *t*- and color axes compared to Figure 3.5. The bold green line in Figure 3.6b indicates a westward propagation speed of 1.03 km d$^{-1}$ as calculated in section 3.3.3.1.

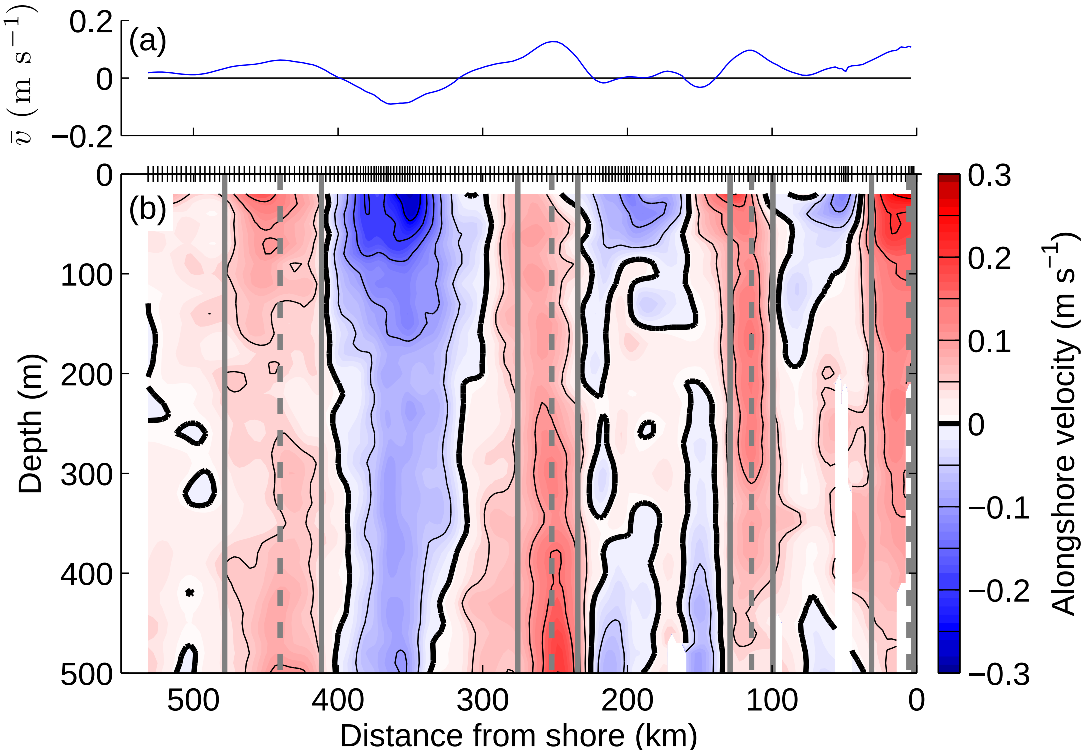

**Figure 3.7**: Example of identifying poleward jets using ADP velocity data from 18 June to 10 July 2008 on Line 90.0. (a) Vertically averaged alongshore current between 150 and 500 m, $\bar{v}$. (b) Low-pass filtered alongshore velocity with the centers and edges of poleward jets identified by the dashed and solid grey lines, respectively. The jets centered nearest the coast and 250 km from the coast were identified as the strongest jets inshore and offshore of the SRR, respectively, and included in the averages of Figure 3.8. Velocity contours are drawn every 0.05 m s$^{-1}$ with the zero contour given in bold. Positive velocities are poleward. Tick marks on the top axis (Figure 3.7b) indicate the positions of individual profiles.

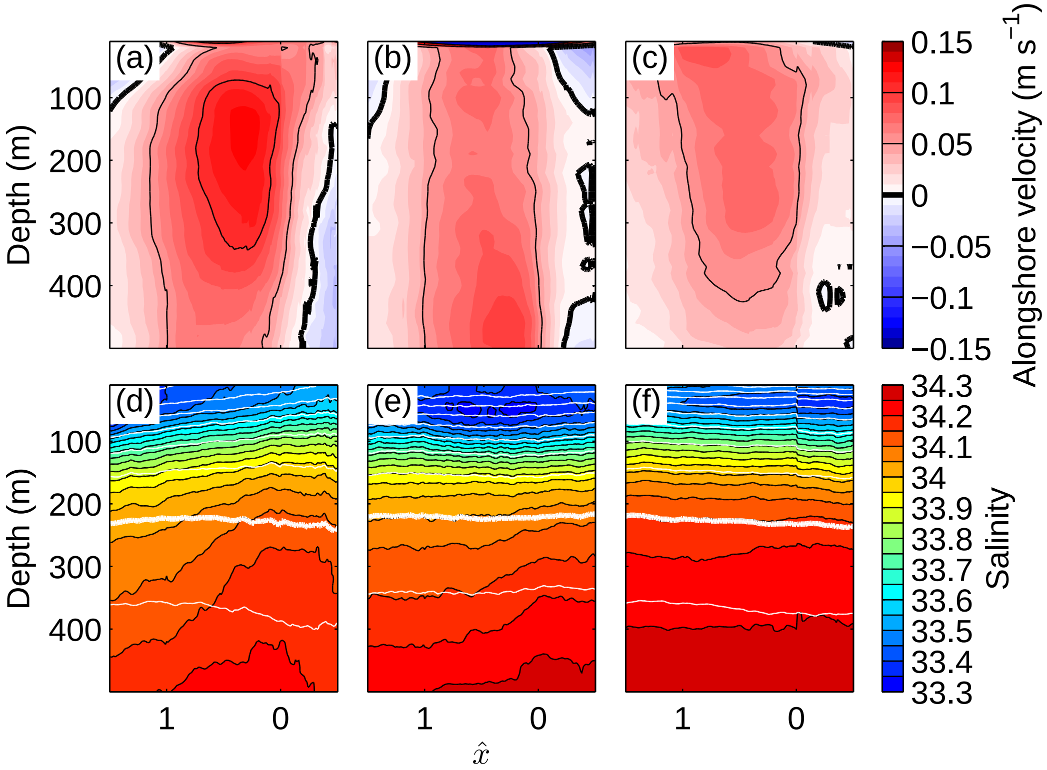

**Figure 3.8**: (a–c) Alongshore velocity and (d–f) salinity (color) and potential density (white contours) averaged in jet-following coordinates for the poleward jets at Line 80.0 (Figures 3.8a and 3.8d), offshore of the Santa Rosa Ridge on Line 90.0 (Figures 3.8b and 3.8e), and inshore of the Santa Rosa Ridge on Line 90.0 (Figures 3.8c and 3.8f). Potential density contours are drawn every 0.25 kg m$^{-3}$, and the 26.5 kg m$^{-3}$ isopycnal is given in bold.

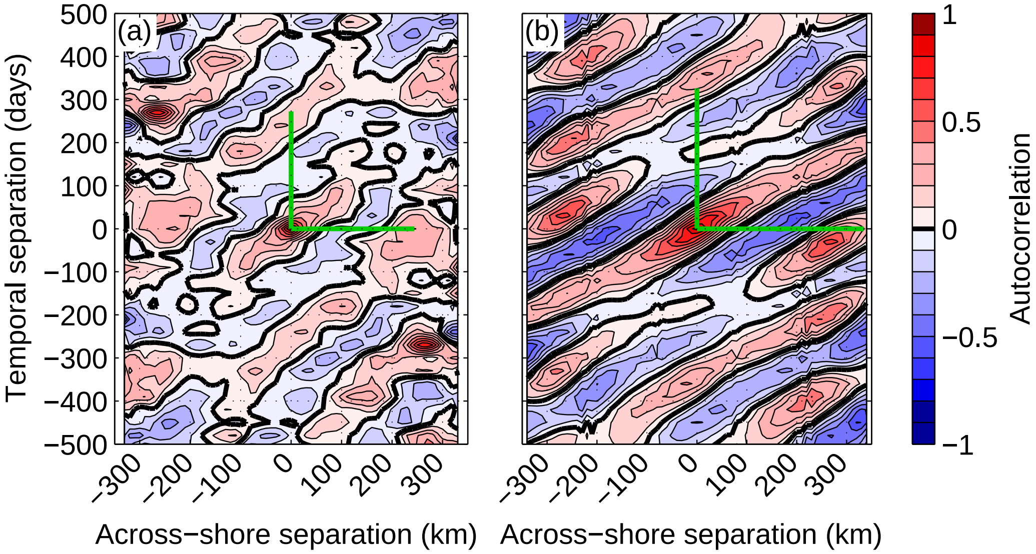

**Figure 3.9**: Autocorrelation of alongshore velocity at 300 m depth and offshore of the SRR on Line 90.0 from (a) observations and (b) the numerical simulation. The contour interval is 0.1 and the zero contour is given in bold. The two green lines in each panel represent the wavelength and period of the best-fit sinusoid to each autocorrelation.

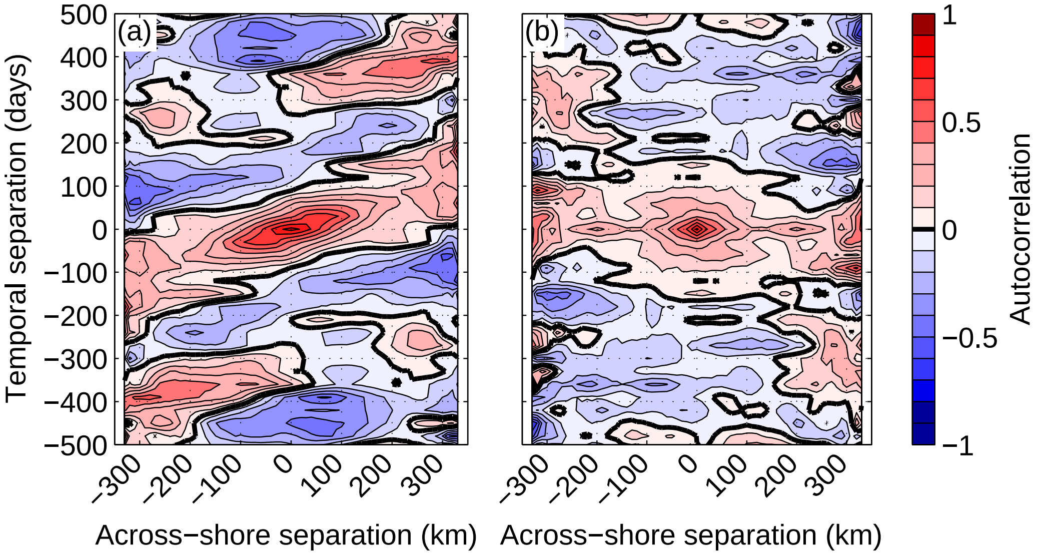

**Figure 3.10**: (a) Autocorrelation of depth of the 26.5 kg m$^{-3}$ isopycnal and (b) autocorrelation of salinity on the same isopycnal offshore of the SRR on Line 90.0. The contour interval is 0.1 and the zero contour is given in bold.

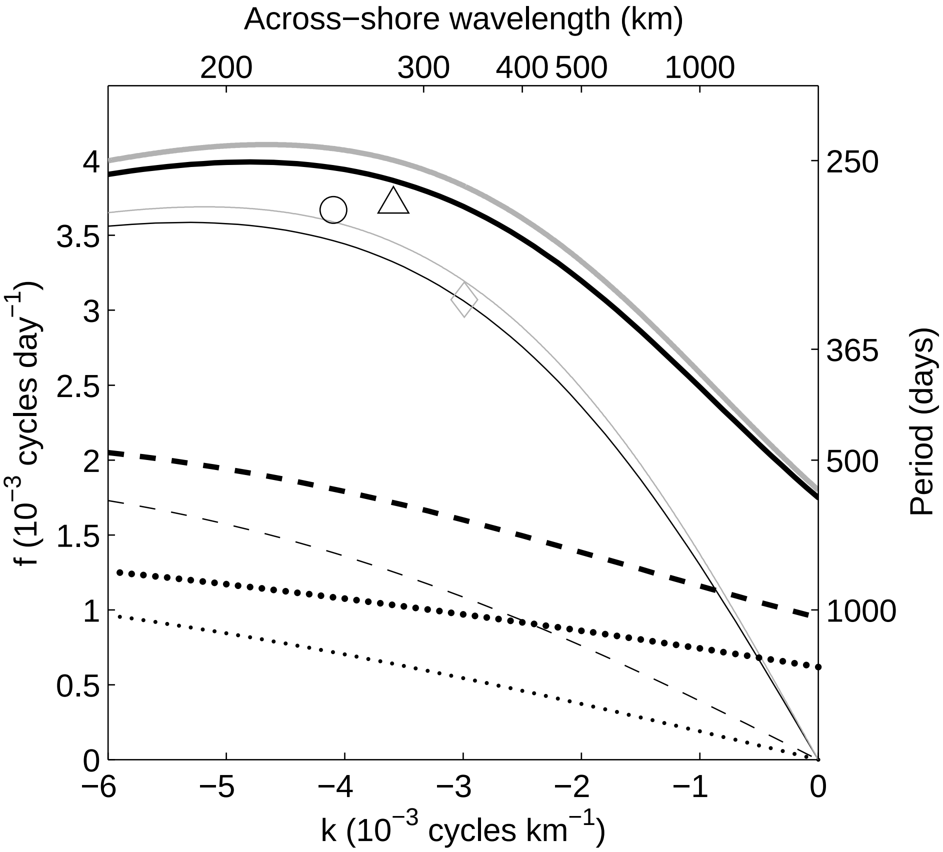

**Figure 3.11**: Rossby wave dispersion relations (lines) and across-shore wave number ($k$) and frequency ($\omega$) of observed alongshore velocity at 300 m (circle), observed slope of the 26.5 kg m$^{-3}$ isopycnal (triangle), and simulated alongshore velocity at 300 m (diamond). The black curves are for the observed stratification; the grey curves are for the simulated stratification. The thin curves are for waves propagating along the observation line (3.2), and the bold lines show the maximum frequency for each across-shore wave number. The first (solid), second (dashed), and third (dotted) baroclinic modes are shown for the dispersion relation with observed stratification; only the first baroclinic mode is shown for the modeled stratification.

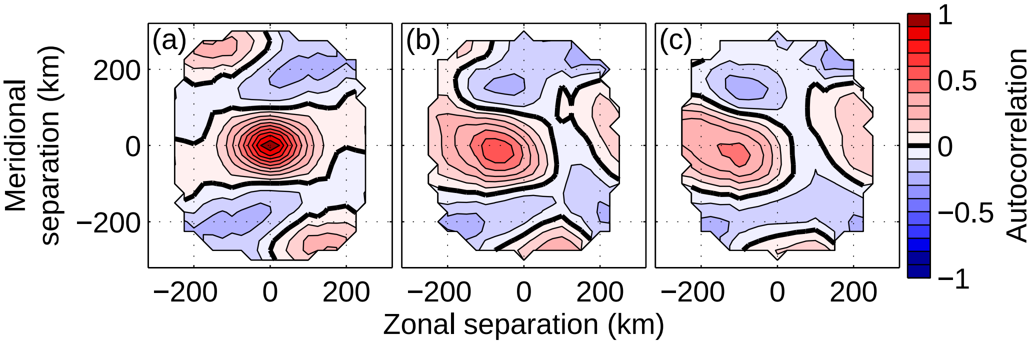

**Figure 3.12**: Spatial autocorrelations of vector velocity from the numerical simulation in the region [122°W 119°W] × [30°N 33°N], which surrounds the poleward current offshore of the SRR. Autocorrelations are calculated as described in the text and (3.3) and shown for calculations with data pairs separated in time by (a) 0 days, (b) 50 days, and (c) 75 days. Results are masked when the number of pairs is less than 5% of square of the number of data points.

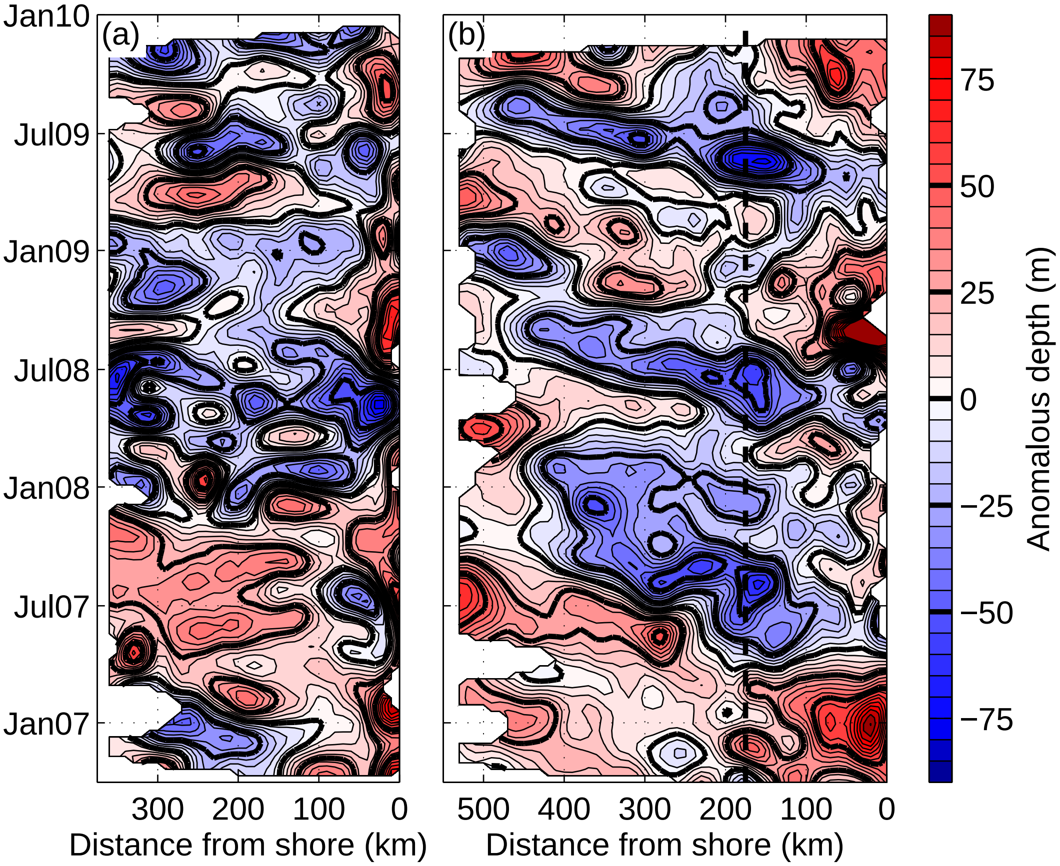

**Figure 3.13**: Hovmöller plots of the anomalous depth of the 26.5 kg m$^{-3}$ isopycnal at (a) Line 80.0 and (b) Line 90.0. The anomalous depth is calculated by removing a mean and across-shore trend as in the calculation of the covariances. Positive anomalies indicate deepening of the isopycnal. Mapping parameters and plot features are as in Figure 3.5.

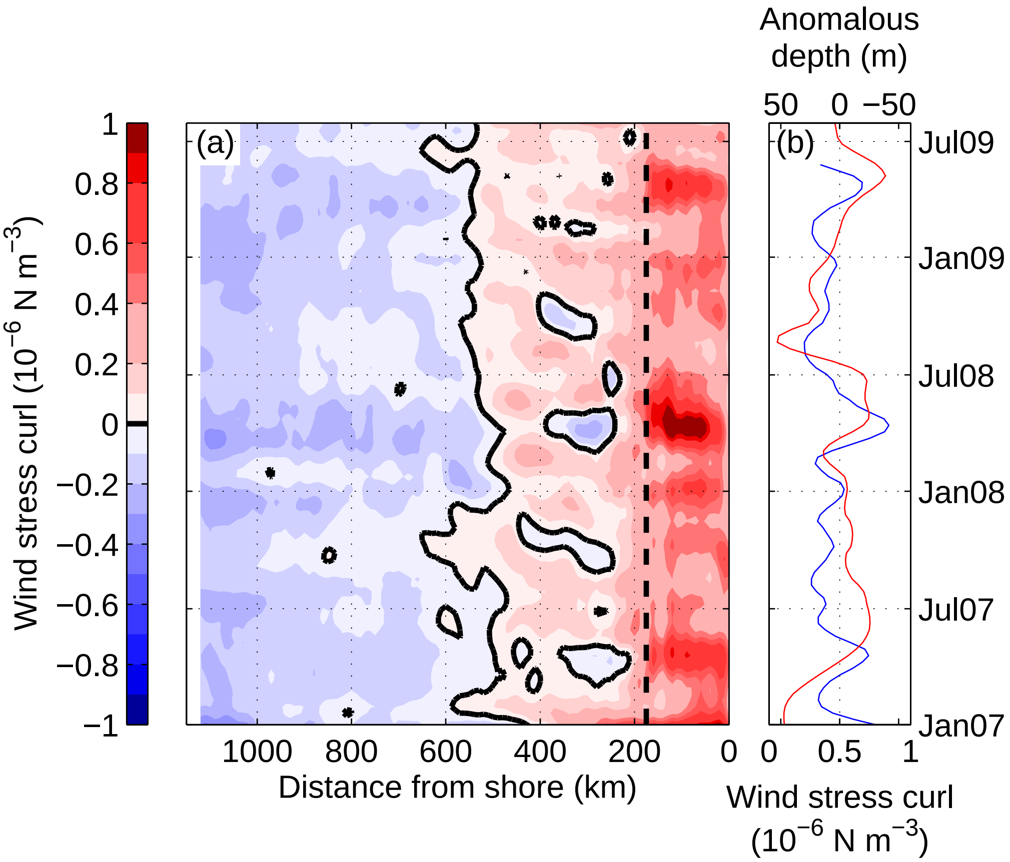

**Figure 3.14**: (a) Hovmöller plot of the adjusted wind stress curl along Line 90.0 in the numerical simulation. The dashed line denotes the location of the SRR. The zero contour is given in black. The wind stress curl has been objectively mapped as in Figure 3.5. (b) Mean adjusted wind stress curl (blue) and mean observed anomalous depth of the 26.5 kg m$^{-3}$ isopycnal (red) inshore of the SRR on Line 90.0 as functions of time. The time axes are the same in Figures 3.14a and 3.14b.

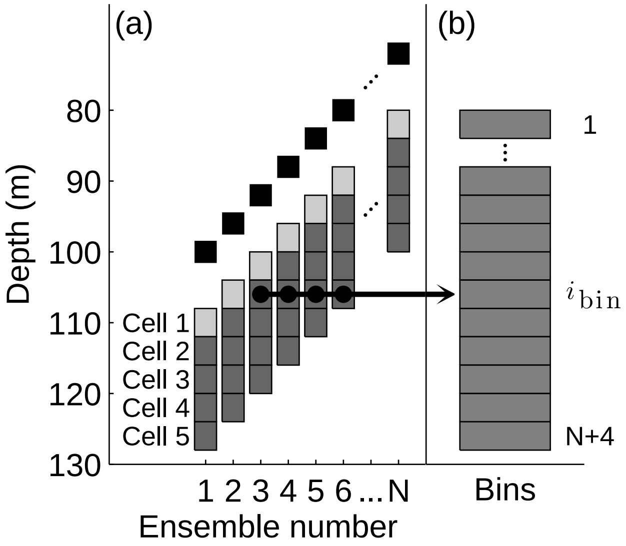

**Figure 3.B1**: (a) Sampling pattern and (b) estimation bins for glider ADP sampling. The position of the glider at the time of each of the $N$ 16-ping ensembles is shown by the black squares. For each ensemble, the glider measures along-beam speed and return strength in five measurement cells below the glider. The timing of ensembles is set such that measurement cells from successive ensembles align as indicated. The cells intersected by the black arrow are at the same depth and sort into the $i$th bin as indicated. Measurements from the shallowest cell for each ensemble (cell 1, light grey shading) are not used in estimates of velocity.

# Chapter 4

# Underwater gliders reveal rapid arrival of El Niño effects off California's coast

Robert E. Todd, Daniel L. Rudnick, Russ E. Davis, and Mark D. Ohman

**Abstract.** The 2009–2010 El Niño marked the first occurrence of this climate phenomenon since the initiation of sustained autonomous glider surveillance in the California Current System (CCS). Spray glider observations reveal the subsurface effects of El Niño in the CCS with spatial and temporal resolutions that could not have been obtained practically with any other observational method. Glider observations show that upper ocean waters in the CCS were unusually warm and isopycnals were abnormally deep during the El Niño event, but indicate no anomalous water masses in the region. Observed oceanic anomalies in the CCS are nearly in phase with an equatorial El Niño index and local anomalies of atmospheric forcing. These observations point toward an atmospheric teleconnection as an important mechanism for the 2009–2010 El Niño's remote effect on the midlatitude CCS.

## 4.1 Introduction

El Niño conditions, identified as anomalously warm upper ocean temperatures in the central and eastern equatorial Pacific [*Philander*, 1983; *McPhaden*, 1999], returned to the tropical Pacific from June 2009 through May 2010. Effects of El Niño events extend beyond the tropical Pacific; they have had dramatic impacts on the hydrography and dynamics of the California Current System (CCS) [*Simpson*, 1984; *Dever and Winant*, 2002; *Lynn and Bograd*, 2002; *Strub and James*, 2002] and on biological productivity and community structure [*Lavaniegos et al.*, 2002; *Chavez et al.*, 2002; *Lavaniegos and Ohman*, 2007] in this ecologically and economically important eastern boundary upwelling system. Mechanisms by which El Niño may affect the CCS are changes in basin-wide atmospheric conditions and surface forcing (atmospheric teleconnections) [*Simpson*, 1984; *Emery and Hamilton*, 1985; *Ramp et al.*, 1997; *Schwing et al.*, 2002], propagation of coastally trapped waves from the tropics [*Enfield and Allen*, 1980; *Chelton and Davis*, 1982; *Meyers et al.*, 1998; *Ramp et al.*, 1997; *Strub and James*, 2002], and anomalous advection of warmer water masses of southern or western origin into the CCS [*Simpson*, 1984; *Bograd et al.*, 2001; *Lynn and Bograd*, 2002].

The effects of the strong 1997–1998 El Niño [*McPhaden*, 1999] were heavily studied in the CCS using ship-based observations [*Lynn and Bograd*, 2002], moorings and drifters [*Dever and Winant*, 2002], and satellite observations [*Strub and James*, 2002]. Of these methods, only ship-based methods provided spatially broad observations of the subsurface effects of El Niño, and this only with great expense and substantial manpower. The 2009–2010 El Niño marks the first time that autonomous instruments have been able to provide spatially broad observations at the temporal resolution needed to study the effects of El Niño in the CCS.

We use continuous upper ocean observations collected by autonomous underwater gliders to show the effects of the 2009–2010 El Niño on the upper ocean off the coast of California. The observations show oceanic anomalies that are consistent with an atmospheric teleconnection being an important mechanism for this event while ruling out an advective influence. Glider observations can neither confirm nor exclude the influence of coastally trapped waves. This is the first use of a network of autonomous underwater vehicles to resolve the mechanisms of an El Niño event in the upper ocean.

## 4.2 Glider Observations and Ancillary Data

Spray gliders [*Sherman et al.*, 2001; *Rudnick et al.*, 2004] are buoyancy-driven autonomous underwater vehicles that profile along a sawtooth path through the upper ocean. Gliders have been continuously surveying along three established California Cooperative Oceanic Fisheries Investigations (CalCOFI, www.calcofi.org) survey lines in the CCS (Figure 4.1) since late 2006 [*Todd et al.*, 2011a]. Line 66.7 extends 550 km offshore from Monterey Bay; Line 80 extends 350 km offshore from Point Conception; and Line 90 extends 550 km from near Dana Point and through the Southern California Bight (SCB). Gliders provide observations of temperature, salinity, density, and velocity in the upper 500 m with horizontal resolution of 3 km and transects repeated about every 3 weeks (Figure 4.2a–c). Differences between the glider's velocity over land and velocity through the water for each dive give estimates of vertically averaged velocity [*Todd et al.*, 2011a]. This analysis uses glider observations collected between October 2006 and October 2010.

To aid in interpreting the glider observations, we use equatorial sea surface temperature (SST) anomalies in the form of the Oceanic Niño Index (ONI, Figure 4.3a) and wind stress from the U.S. Navy's operational eastern Pacific COAMPS product [*Hodur*, 1997]. The ONI is provided by the NOAA Climate Prediction Center (www.cpc.noaa.gov); it is the three-month running mean of SST anomalies in the Niño 3.4 region (5°S–5°N,120°W–170°W) relative to a 1971–2000 base period. COAMPS output was generated by the Fleet Numerical Meteorology and Oceanography Center and provided online by the U.S. Global Ocean Data Assimilation Experiment (www.usgodae.org). The COAMPS product provides wind stress with sufficient resolution (27 km) to calculate wind stress curl in the SCB, and it is immediately available so that we can compare with recently collected glider observations. COAMPS wind stress curl compares favorably with optimized wind stress curl from a numerical state estimate of the CCS for the period 1 January 2007 to 30 July 2009 [*Todd et al.*, 2011a] at monthly time scales, so we believe the COAMPS wind product is sufficient for use in this analysis.

## 4.3 Results and Discussion

Upper ocean temperatures in the SCB were unusually warm during winter 2009–2010, a characteristic manifestation of El Niño in the CCS [*Lynn and Bograd*, 2002; *Dever and Winant*, 2002]. Along Line 90, temperatures at 50 m depth and within 200 km of the coast (Figure 4.2c) exceeded 15 °C in early 2010. These were the warmest winter temperatures observed in the area since glider observations began. Temperatures within 200 km of shore along the other two survey lines (Figures 4.2a and 4.2b) and at other depths (not shown) were similarly warm in early 2010.

Removing a mean annual cycle more clearly shows the distribution of unusually warm waters. We define temperature anomalies at 50 m on each survey line relative to mean annual cycles constructed by objectively mapping [*Bretherton et al.*, 1976] observations from all years into a single year. Warm (positive) anomalies at 50 m (Figures 4.2d–4.2f) appeared in mid-2009 within 200 km of the coast on Lines 80 and 90 and 100–200 km offshore on Line 66.7, coincident with the onset of El Niño in the equatorial Pacific. Soon after, there was a brief period of negative temperature anomalies at 50 m along Lines 80 and 90 that we attribute to upwelling that continued longer than during previously sampled years; the timing and magnitude of upwelling in the CCS are known to vary interannually [*Schwing et al.*, 2006]. From late 2009 through the spring of 2010, warm anomalies of 0.5–1.5 °C at 50 m extended over most of the three survey lines. The westward propagation of El Niño anomalies apparent in Figure 4.2 is consistent with observations during previous events [*Lynn and Bograd*, 2002].

We create various indices of the physical state of the CCS by averaging anomalies of properties in the across-shore direction. As above, anomalies are defined relative to mean annual cycles constructed by objective mapping. Since El Niño-related temperature anomalies were largest within 200 km of the coast on Line 90 (Figure 4.2), we focus on this region when averaging anomalies. This region is the portion of Line 90 inshore of the topographic ridge that defines the western boundary of the SCB (Figure 4.1). We compare these glider-based indices to the ONI, an equatorial gauge of El Niño. We do not report correlation statistics between indices because the currently available observations capture only a single El Niño-La Niña cycle and test statistics therefore have a limited number of effective degrees of freedom.

Temperature anomalies at 10 m and 50 m (Figures 4.3b and 4.3c) generally varied in phase with the ONI over the observation period. Upper ocean temperatures in the CCS were anomalously warm at the end of the mild 2006–2007 El Niño, became cool during the 2007–2008 La Niña, and warmed again with the onset of the 2009–2010 El Niño in June 2009. Warm anomalies persisted from June 2009 through May 2010 with the exception of a period of cool anomalies at 50 m in late 2009 due to variability in the timing and magnitude of upwelling. A return to cool anomalies in the CCS accompanied the onset of La Niña in the summer of 2010. There is little, if any, phase lag between warming of equatorial sea surface temperatures and warming in the upper ocean off California.

Anomalous depth of the 26.0 kg $m^{-3}$ isopycnal (Figure 4.3d) was also in phase with the ONI. Generally found within the thermocline, the isopycnal was deeper during El Niño events and shallower during La Niña events. The depression (elevation) of isopycnals during El Niño (La Niña) events is consistent with the observed elevation (depression) of sea surface height (SSH) along the west coast of North America during previous El Niño (La Niña) events [*Enfield and Allen*, 1980; *Chelton and Davis*, 1982; *Lynn and Bograd*, 2002].

Glider observations of salinity anomalies and alongshore currents rule out an advective influence of the 2009–2010 El Niño in the CCS. Salinity anomalies on an isopycnal indicate changes in water masses; a salty (and therefore warm) anomaly indicates water of southerly origin [*Lynn and Simpson*, 1987] advected into the region. Salinity on the 26.0 kg $m^{-3}$ isopycnal (Figure 4.3e) did not show consistent, positive anomalies during the 2009–2010 El Niño, implying that there was little advection of warm, salty waters into the SCB. Local alongshore currents in the upper 500 m (Figure 4.3f) also did not show anomalous poleward transport consistently throughout the 2009–2010 El Niño. This result contrasts with the strong 1997–1998 El Niño, which produced isopycnal salinity anomalies along Line 90 that indicated advection of waters from equatorward of 27°N along the coast [*Lynn and Bograd*, 2002]. The 2009–2010 event has been identified as a central-Pacific El Niño with relatively weak temperature anomalies in the eastern equatorial Pacific [*Lee and McPhaden*, 2010; *Lee et al.*, 2010], possibly explaining the lack of coastal advection.

Recent analysis of euphausiid (krill) abundance in Southern California waters (M. D. Ohman, unpublished data, 2010) also indicates a lack of an advective influence on the CCS by the 2009–2010 El Niño. In spring 2010, the two species of subtropical euphausiids that have been elevated in abundance in Southern California during some previous El Niño springs [see *Brinton and Townsend*, 2003] were either completely undetectable (*Nyctiphanes simplex*) or present at extremely low abundance (*Euphausia eximia*). The absence of these planktonic species suggests that the subtropical waters in which they live were not present in the SCB during this El Niño, in contrast to previous events.

Surface forcing by alongshore wind stress and wind stress curl (Figures 4.3g and 4.3h) shows anomalies during the 2009–2010 El Niño that could have caused the observed oceanic anomalies. Anomalies of alongshore wind stress and wind stress curl were downwelling favorable during the 2009–2010 El Niño. Given a shallow upwelling overturning cell [*Davis*, 2010], depression of isopycnals cuts off the supply of cold, subsurface water that is upwelled and mixed in the surface layer, leading to the observed warming in the upper ocean. Anomalies of wind stress curl and, to a lesser degree, alongshore wind stress in the SCB peaked with the onset El Niño conditions in May 2009 and the initial appearance warm temperature anomalies and depressed isopycnals. The decrease in wind stress curl anomalies in late 2009 is consistent with the observed cooler temperatures, shallower isopycnals and extended upwelling season. From late 2009 through the end of the El Niño event, downwelling favorable wind stress and wind stress curl anomalies persisted over the SCB. The switch to La Niña conditions in summer 2010 saw alongshore wind stress anomalies change sign and wind stress curl anomalies decrease in magnitude. The correspondence between observed hydrographic anomalies in the CCS and anomalies of alongshore wind stress and wind stress curl over the SCB points to an atmospheric teleconnection as an important mechanism for the 2009–2010 El Niño's effects in the CCS.

El Niño-related SSH anomalies have been shown to propagate poleward as coastally trapped waves at phase speeds ranging from 0.4–3 m $s^{-1}$ [*Enfield and Allen*, 1980; *Chelton and Davis*, 1982; *Ramp et al.*, 1997; *Meyers et al.*, 1998]. The fastest of these propagation speeds agree with the theoretical speed of first-mode baroclinic Kelvin waves and would result in propagation from the equator to the CCS in a month or less, consistent with the near zero phase lag between anomalies in the CCS and the ONI. Our glider observations are spread over about 525 km along the coast with transects repeated every three weeks, so we are unable to resolve possible poleward propagation at Kelvin wave speeds; a wave traveling poleward at 3 m $s^{-1}$ would take about two days to travel from Line 90 to Line 66.7. We cannot rule out poleward propagating coastally trapped waves as a mechanism for the 2009–2010 El Niño's effect on the CCS. However, previous studies have shown that the mouth of the Gulf of California near 23°N can act as a barrier to coastally trapped waves [*Ramp et al.*, 1997; *Strub and James*, 2002]. Satellite observations of SSH and tide gauge observations, which have greater alongshore coverage and temporal resolution, are necessary to identify the influence of coastally trapped waves.

## 4.4 Conclusion

The three ways that El Niño events may affect the CCS are (1) atmospheric teleconnections, (2) oceanic advection, and (3) oceanic coastally trapped waves. We conclude that an atmospheric teleconnection was likely important during the 2009–2010 El Niño, and that advection of southern waters into the CCS did not occur. The glider observations and local atmospheric data examined here do not allow a definitive conclusion concerning the importance of coastally trapped waves.

*Acknowledgments.* Spray glider deployments were supported by the Instrument Development Group (IDG) at the Scripps Institution of Oceanography. We acknowledge funding from the Gordon and Betty Moore Foundation, the Coastal Ocean Currents Monitoring Project (COCMP), NSF through the California Current Ecosystem LTER site, and NOAA through the Consortium on the Ocean's Role in Climate (CORC) and the Southern California Coastal Ocean Observing System (SCCOOS). R.E.T. was partially supported by an Achievement Rewards for College Scientists (ARCS) scholarship. Chapter 4, in full, is a reproduction of the material as it appears in *Todd, Rudnick, Davis, and Ohman* [2011b], *Geophys. Res. Lett., 38*, L03609. The dissertation author was the primary investigator and author of this work.

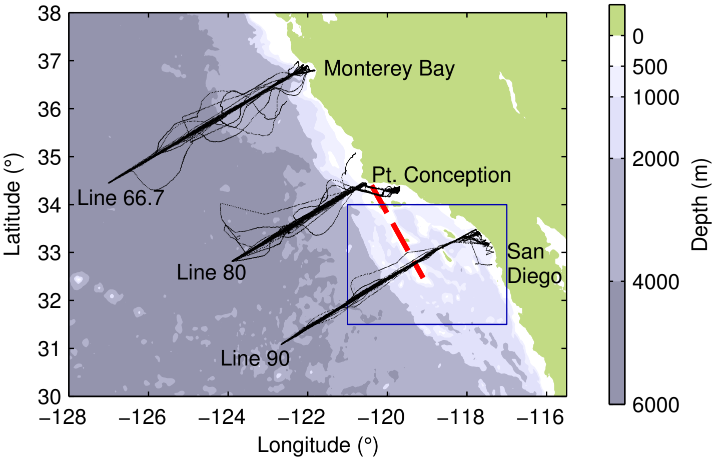

**Figure 4.1**: Location of all glider observations used in this analysis. Glider tracks along CalCOFI Lines 66.7, 80, and 90 are in black. Bathymetry is shown in grey. The dashed red line indicates the topographic ridge at the western boundary of the SCB. The blue box denotes the region over which surface forcing data are averaged in Figure 4.3.

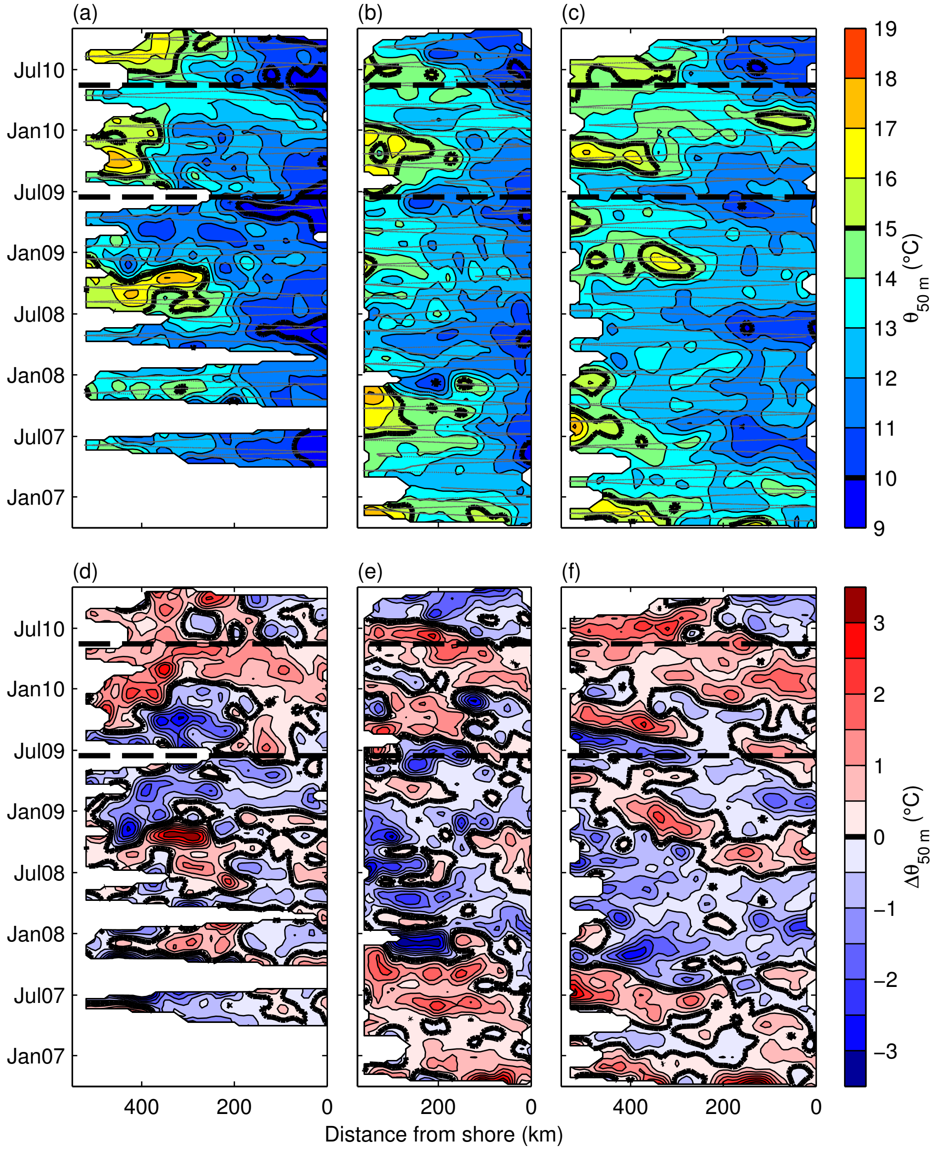

**Figure 4.2**: Hovmöller plots of (a–c) potential temperature ($\theta$) and (d–f) potential temperature anomaly ($\Delta\theta$) at 50 m along Line 66.7 (Figures 4.2a and 4.2d), Line 80 (Figures 4.2b and 4.2e), and Line 90 (Figures 4.2c and 4.2f). Observations were objectively mapped using a Gaussian covariance with 30-km and 60-day scales. Anomalies are defined relative to a mean annual cycle constructed by objectively mapping observations from all years into a single year. Small grey dots in Figures 4.2a–4.2c show the across-shore and temporal sampling by gliders; each point indicates a single glider profile. Dashed horizontal lines indicate the beginning and end of the 2009–2010 El Niño based on the ONI.

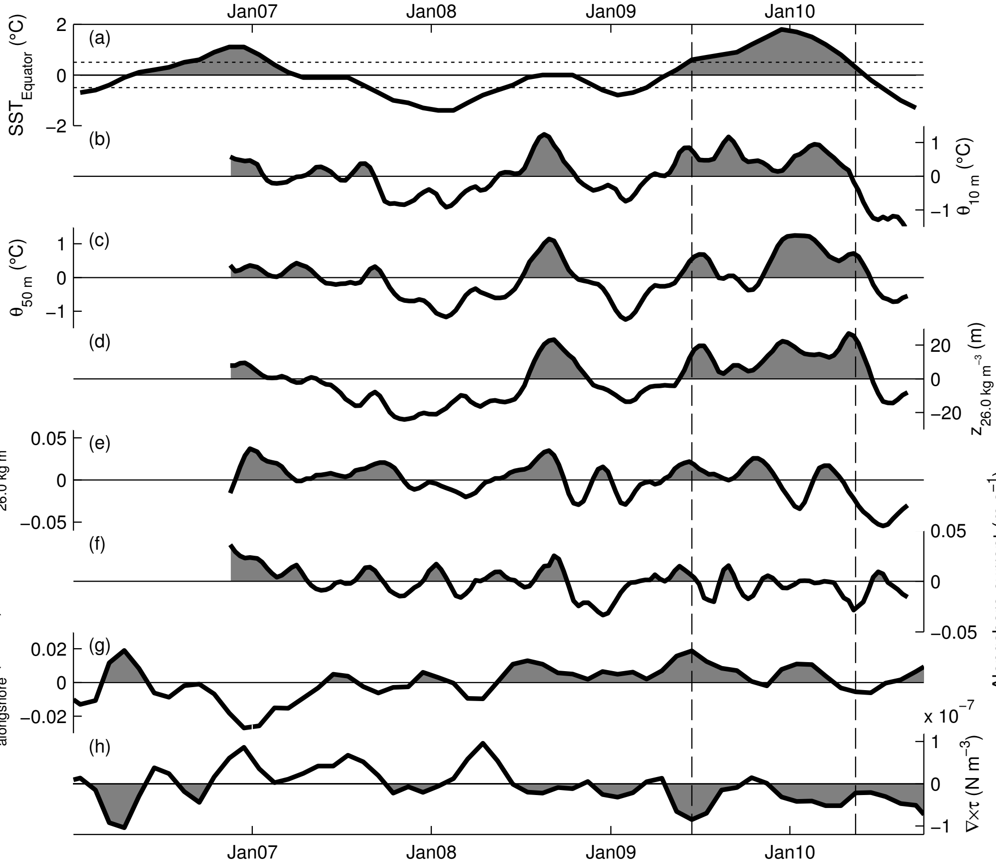

**Figure 4.3**: Time series of property anomalies. (a) Equatorial SST in the Niño 3.4 region (the Oceanic Niño Index, ONI). Anomalies averaged within 200 km of the coast on Line 90: (b and c) potential temperature ($\theta$) at depths of 10 m and 50 m, respectively; (d) depth ($z$) of the 26.0 kg m$^{-3}$ isopycnal (positive anomalies are deeper); (e) salinity ($s$) on the 26.0 kg m$^{-3}$ isopycnal; and (f) alongshore currents (positive poleward) averaged over the upper 500 m. (g and h) Alongshore wind stress ($\tau$, positive poleward) and wind stress curl ($\nabla \times \tau$), respectively, over the boxed region in Figure 4.1 from the 27-km COAMPS product. Monthly COAMPS anomalies are defined relative to means over 2003–2010. Dotted horizontal lines in Figure 4.3a indicate the thresholds for El Niño and La Niña conditions. Dashed vertical lines indicate the start and end of the 2009–2010 El Niño based on the ONI.

# Chapter 5

# Upper ocean thermohaline structure in the California Current System

Robert E. Todd, Daniel L. Rudnick, Matthew R. Mazloff, Bruce D. Cornuelle,
and Russ E. Davis

**Abstract.** Upper ocean thermohaline structure in the California Current System is investigated using sustained observations from autonomous underwater gliders and a numerical state estimate. Both observations and the state estimate show layers distinguished by the temperature and salinity variability along isopycnals (i.e., spice variance). Mesoscale and submesoscale spice variance is largest in the seasonally restratifying layer, decreases to a minimum below the pycnocline near 26.2 kg m$^{-3}$, and then increases again near the 26.6 kg m$^{-3}$ isopycnal. Layers of high and low spice variability are collocated with large and small mean, large-scale spice gradients, consistent with stirring of large-scale gradients to produce smaller scale thermohaline structure. Adjoint passive tracer calculations in the numerical state estimate are used to show that waters in each layer have different histories that lead to their distinctive thermohaline properties. Waters in the restratifying layer have source waters to the north along the coast; waters in progressively deeper layers contain larger portions of water with southerly origin. Below the restratifying layer, local bathymetry forces waters to enter the Southern

California Bight from the south along the coast, regardless of origin. Effective diffusivity decreases monotonically with depth in the simulation, so changes in stirring with depth are not sufficient to create the layers of high and low spice variance.

## 5.1 Introduction

In the California Current System (CCS), waters of equatorial, central Pacific, and subarctic origin [*Lynn and Simpson*, 1987], meet in a region characterized by equatorward and poleward flows [*Hickey*, 1979; *Lynn and Simpson*, 1987, 1990; *Todd et al.*, 2011a], eddies [*Davis et al.*, 2008; *Todd et al.*, 2009], and upwelling. The combination of these processes stirs and mixes the various water masses across a range of scales. Long-term observations by underwater gliders in the CCS resolve the resulting thermohaline structure and reveal along-isopycnal layers that are distinguished by their thermohaline structure. We investigate the history of water in these distinct layers using a numerical state estimate.

Thermohaline structure in the upper ocean is the end result of processes occurring across a range of scales and over an extended period of time. Along surfaces of constant depth, the internal wave field causes vertical stratification to be projected onto the horizontal through tilting of isopycnals. Thermohaline variability along isopycnals is unaffected by the internal wave field and variability is controlled by horizontal advection and mixing [*Cole and Rudnick*, 2011]. Temperature and salinity fluctuations along isopycnals, which vary from cold and fresh to warm and salty, provide a dynamically passive tracer [*Veronis*, 1972] that has been referred to as spice [*Munk*, 1981].

*Cole and Rudnick* [2011] demonstrated the presence of along-isopycnal layers defined by salinity variance along isopycnals (i.e., spice variance) using 2.5 years of repeated glider transects north of Hawaii. Though spice variance was expected to decay monotonically with depth, they found that spice variance was lowest in an intermediate layer that coincided with an oxygen minimum and a local maximum in stratification. The distinct layers were inferred to have different histories of stirring and mixing which lead to their unique thermohaline properties.

Underwater gliders [*Davis et al.*, 2002; *Rudnick et al.*, 2004] are well suited for providing long-term observations of thermohaline structure in the upper ocean. Gliders can provide a continuous presence that would be prohibitively expensive using ship-based observational tools while collecting measurements at high spatial resolution (typically a few kilometers between profiles). In many parts of the ocean, gliders are able to occupy predefined transects repeatedly with relatively small deviations due to strong currents [e.g., *Perry et al.*, 2008; *Castelao et al.*, 2010; *Todd et al.*, 2011a; *Cole and Rudnick*, 2011].

Numerical state estimation [*Wunsch*, 2006; *Wunsch and Heimbach*, 2007] is a powerful tool for understanding oceanic processes. A state estimate is a dynamically consistent numerical simulation with forcing, initial conditions, and boundary conditions adjusted so that the simulation agrees well with a wide array of observations over an extended period of time. *Todd et al.* [2011a] showed that a numerical simulation of the CCS that incorporates observations from gliders and other sources reproduces the velocity field in the region well. In this analysis, we take advantage of the adjoint [*Heimbach et al.*, 2005] to the same state estimate to investigate the past distributions of tagged waters.

This paper is organized as follows: section 5.2 describes our glider observations, numerical state estimate, and analysis techniques; section 5.3.1 describes the mean, large-scale thermohaline structure in the CCS; section 5.3.2 describes layers defined by mesoscale and submesoscale spice variance; section 5.3.3 considers the history of those layers using adjoint passive tracers in the numerical state estimate; and section 5.4 summarizes the results. The appendix derives the adjoint to the advection-diffusion equation and the passive tracer sensitivity in a continuous framework.

## 5.2 Data and Methods

### 5.2.1 Glider Observations

Spray gliders [*Sherman et al.*, 2001; *Rudnick et al.*, 2004] have been continually surveying in the CCS [*Davis et al.*, 2008; *Todd et al.*, 2011a,b] along California Cooperative Oceanic Fisheries Investigations (CalCOFI) Lines 66.7, 80.0, and 90.0 (Figure 5.1) for more than four years. Line 66.7 extends about 525 soutwestward from Monterey Bay; Line 80.0 extends about 375 km southwestward from Point Conception; and Line 90.0 extends about 525 km southwestward from Dana Point, California and through the Southern California Bight (SCB). Continuous observations along Lines 80.0 and 90.0 began in October 2006, while glider surveys along Line 66.7 began in April 2007 (Figure 5.2a–c). Gliders provide observations of temperature, salinity, density, velocity, chlorophyll fluorescence, and acoustic backscatter in the upper 500 m with horizontal resolution of about 3 km and transects repeated about every three weeks [*Davis et al.*, 2008; *Todd et al.*, 2011a,b]. This analysis uses observations collected through October 2010 with a total of 40 transects on Line 66.7, 75 transects on Line 80.0, and 54 transects on Line 90.0. With the exception of February and March along Line 66.7, glider observations are well spaced throughout the year on each line (Figure 5.2d–f), so means calculated from the observations are not biased by the sampling pattern.

Individual transects of salinity and density from each survey line (Figure 5.3a–c) demonstrate the high spatial resolution of the glider observations and reveal variability across all observed scales. The smallest-scale variability in depth of isopycnals is largely due to heaving by the internal wave field. The relatively slow horizontal speed of the gliders (about 0.25 m $s^{-1}$) results in high-frequency temporal variability being aliased with high-wave number spatial variablity [*Rudnick and Cole*, 2011], so much of the small-scale salinity variability in Figure 5.3a–c is due to the vertical displacement of isopycnals. This effect is apparent in observations of properties along isobaric surfaces at scales smaller than about 30 km; observations of properties along isopycnals are not affected because following isopycnals explicitly filters out the internal waves [*Rudnick and Cole*, 2011]. Temperature along isopycnals, which is equivalent to spice, from the same example transects (Figure 5.3d–f) also shows variability across the observed range of scales. On some isopycnals, such as the 25.0 kg $m^{-3}$ isopycnal on all three transects, temperature fluctuates by a few degrees throughout the transect, so spice variance is relatively large. Along the 26.0 kg $m^{-3}$ isopycnal, temperature fluctuations are noticeably smaller. Deeper still, temperature fluctuations and spice variance on these example transects increase again. This apparent layering of spice variability is the main focus of this analysis.

As in *Todd et al.* [2011a], we create mean transects by objectively mapping observations from individual transects onto a uniform grid using a Gaussian covariance with a 30-km length scale, then averaging across transects. Mapping is performed along both depth surfaces and isopycnals. Alongshore geostrophic velocities, when used in place of missing Doppler-derived currents (Figure 5.2), are also calculated by objective mapping [*Todd et al.*, 2011a].

### 5.2.2 Numerical State Estimate

The numerical state estimate used in this analysis is the same regional, data-assimilating version of the MITgcm [*Marshall et al.*, 1997a,b] used in *Todd et al.* [2011a]. The model domain is $\left[\begin{array}{cc} 130°\text{W} & 114°\text{W} \end{array}\right] \times \left[\begin{array}{cc} 27.2°\text{N} & 40°\text{N} \end{array}\right]$ (Figure 5.1, solid blue box), and the period of simulation is 1 January 2007 to 30 July 2009. Here we use the 90th data-assimilating iteration. Open boundary conditions have not yet converged to optimal values, resulting in some unrealistic characteristics along the open boundaries. To avoid these areas, we restrict our analysis to the portion of the domain greater than 1° from the open boundaries (Figure 5.1, dashed blue box).

### 5.2.3 Wavelets

We use the wavelet transform to partition along-isopycnal salinity variance by scale and location. The wavelet transform, $\tilde{p}(s, x_0)$, [*Torrence and Compo*, 1998; *Ferrari and Rudnick*, 2000] of a variable $p(x)$ at scale $s$ centered about location $x_0$ is

$$\tilde{p}(s, x_0) = \int_{-\infty}^{\infty} p(x)\psi^*_{s,x_0}(x)\, dx, \tag{5.1}$$

where the $\psi_{s,x_0}(x)$ is a scaled and translated version of the mother wavelet, $\psi(x)$, given by $\psi_{s,x_0}(x) = |s|^{-\frac{1}{2}}\psi\left(\frac{x-x_0}{s}\right)$, and the $^*$ indicates the complex conjugate. For a mother wavelet, we choose the Morlet wavelet, $\psi(x) = \mathrm{e}^{i2\pi nx}\mathrm{e}^{-\frac{x^2}{2}}$, which is a sinusoid modulated by a Gaussian envelope. The parameter $n$ controls the number of oscillations of the wavelet within the Gaussian envelope; we choose $n = 1$.

The wavelet transform (5.1) is most efficiently calculated by using the Fourier transforms $\hat{p}(k)$ and $\hat{\psi}(k)$ of $p(x)$ and $\psi(x)$, respectively. Since our data (from both observations and the state estimate) are not uniformly spaced in the horizontal, we interpolate the data onto a uniform grid with spacing of 0.5 km before calculating Fourier transforms [*Cole et al.*, 2010]. Oversampling ensures that all resolved scales of variability are retained in resulting wavelet transforms. Data are detrended by removing a linear least squares fit.

The wavelet energy density in the $(s, x_0)$ plane is $\frac{|\tilde{p}(s,x_0)|^2}{E_\psi |s|^2}$, where $E_\psi = \int_{-\infty}^{\infty} \frac{|\hat{\psi}(k)|^2}{|k|}\,dk$. The energy density is normalized such that its integral equals the sum of squared deviations from the least squares fit. For glider observations, we disregard energy content at wavelengths shorter than 6 km, the approximate Nyquist wavelength for glider observations every 3 km. The numerical simulation shows a decrease in energy content around 30-km wavelength due to smoothness constraints, so we only consider results from the simulation at scales larger than 30 km.

### 5.2.4 Passive Tracer Adjoint

To investigate the sources of waters in layers defined by spice variability, we employ the passive tracer adjoint [*Fukumori et al.*, 2004; *Chhak and Di Lorenzo*, 2007; *Gao et al.*, 2011; *Song et al.*, 2011] in our state estimate. By integrating the passive tracer sensitivity backwards in time using the adjoint to the MITgcm [*Heimbach et al.*, 2005], we obtain the sensitivity of tracer concentration in a specified target region to tracer concentration at at all previous locations and times in the model domain (see Appendix 5.A). It is important to note that the passive tracer adjoint is not an inverse and does not allow us to track individual water parcels; it is impossible to “unmix” waters by inverting the numerical model since it is impossible to determine how to uniquely partition a water parcel into its constituents after mixing has taken place [*Fukumori et al.*, 2004]. In the adjoint model, advection runs backwards, but diffusion works as in a forward integration (see section 5.A.1 of the appendix).

For each passive tracer, we create an objective function that represents tracer concentration averaged over the final six days of the simulation. The objective function $J$ is given by

$$J = \int_{t_i}^{t_f} G[C(t), t]\, dt, \tag{5.2}$$

where the function

$$G[C(t), t] = H\left[(t - (t_f - T)\right] \iiint_V w(x, y, z) C(x, y, z, t)\, dx\, dy\, dz, \tag{5.3}$$

defines the target region. In (5.3), $H$ is the Heaviside step function, $t_f$ is the final time of the simulation, $T$ is six days, $C(x, y, z, t)$ is the model tracer concentration in arbitrary units, $V$ is the model domain, and $w(x, y, z)$ is a prescribed weight function that prescribes the horizontal and vertical extent of the target region. The tracer sensitivity is $\partial J/\partial C(x, y, z, t)$ and evolves backwards in time according to the adjoint to the advection-diffusion equation (see section 5.A.2 of the appendix).

When normalized by the total sensitivity over $t_f - T$ to $t_f$, the adjoint tracer sensitivity is the fraction of water in the target region at the end of the simulation that was located at $(x, y, z, t)$; all sensitivities presented are normalized in this manner. In other words, changing the concentration by $\delta C$ at $(x, y, z, t)$ will change $J$, the tracer in the target region during $t_f - T$ to $t_f$, by $\frac{\partial J}{\partial C}\delta C$. Since the tracer is passive, this can only be possible if the water at $(x, y, z, t)$ is advected or mixed into the target region [*Fukumori et al.*, 2004]. The adjoint calculation does not specify when during $t_f - T$ to $t_f$ water from $(x, y, z, t)$ reached the target region, nor does it specify where in the target region those waters are located during $t_f - T$ to $t_f$. To verify that the normalized adjoint tracer sensitivity gives the fraction of water in the target region at the end of the simulation that came from a specified location, *Fukumori et al.* [2004] used the MITgcm to show that the amount of passive tracer released from a source region that reached a specified target region in a one year forward integration equaled the sensitivity in the same source region of an adjoint passive tracer with the same target region.

## 5.3 Results and Discussion

### 5.3.1 Large-Scale Structure

Mean salinity and density as a function of depth (Figure 5.4a–c) show the persistent, large-scale thermohaline structure in the CCS. Low salinity above the pycnocline is the signature of the equatorward flowing California Current [*Lynn and Simpson*, 1987] with lowest salinity further offshore to the south. Near-surface salinity is greatest near the coast on Lines 66.7 and 80.0 and over the SRR on Line 90.0 due to upwelling of saltier thermocline waters [*Davis*, 2010]. Salinity increases with depth within and below the pycnocline. Deeper than 200 m, isohalines and isopycnals do not align; salinity increases along isopycnals toward the coast. This across-shore spice gradient is attributed to northward transport of subtropical waters by persistent poleward currents (Figure 5.4g–i) [*Todd et al.*, 2011a].

Mean salinity along isopycnals (Figure 5.4d–f) has larger horizontal gradients along certain isopycnals. Above the densest outcropping isopycnal (the region we will refer to as the restratifying layer), large spice gradients near the coast on Lines 66.7 and 80.0 and over the SRR on Line 90.0 are, as above, the result of upwelling. Around the 26.0 kg $\mathrm{m}^{-3}$ isopycnal on all three lines, across-shore spice gradients are nearly zero. Below 26.5 kg $\mathrm{m}^{-3}$, spice gradients increase again with largest gradients collocated with the mean poleward currents (Figure 5.4g–i) on each survey line.

The presence of persistent, large-scale spice gradients provides the background gradient necessary for stirring and mixing to produce thermohaline structure at smaller scales [*Klein and Hua*, 1990; *Ferrari and Rudnick*, 2000]. The narrow poleward currents [*Todd et al.*, 2011a] adjacent to similarly strong equatorward flows (Figure 5.4g–i) create a horizontally sheared flow field that can stir the large-scale gradients to smaller scales. Subsequent stirring by eddies and other mesoscale features can then produce smaller-scale structure.

Simulated mean salinity, density, and alongshore currents (Figure 5.5) over the 2.6 years of the state estimate capture the observed mean features well. Most importantly for this analysis, the simulation produces mean across-shore spice gradients that are largest in the restratifying layer and between the 26.5 kg $\mathrm{m}^{-3}$ and 27.0 kg $\mathrm{m}^{-3}$ isopycnals with a layer of small mean spice gradients around the 26.0 kg $\mathrm{m}^{-3}$. On an alongshore transect through the state estimate (Figure 5.1), mean properties show the alongshore structure that is not well resolved by the glider observations (Figure 5.6). The low salinity signature of the California Current is found in the upper 100 m and within the restratifying layer all along the transect with salinity decreasing toward the north. Below the pycnocline and restratifying layer, mean alongshore spice gradients (Figure 5.6b) are smaller than the corresponding across-shore gradients (Figure 5.5d–f).

### 5.3.2 Meso- and Submesoscale Structure

To show the mean thermohaline structure at smaller scales, we first average the wavelet transforms of observed along-isopycnal salinity across wavelengths of 30–200 km (which we will refer to as mesoscales) and wavelengths of 6–30 km (which we refer to as submesoscales). We then average across the repeated transects to obtain the mean across-shore and vertical structure of spice variance at those scales (Figure 5.7). Spice variance at mesoscales is greater than at submesoscales, consistent with $k^{-2}$ spectra of along-isopycnal salinities (not shown). This decomposition reveals three distinct along-isopycnal layers within the upper 500 m of the water column observed by the gliders that are similar to the layers of spice variance reported by *Cole and Rudnick* [2011] north of the Hawaiian Islands.

Spice variance is highest within the seasonally restratifying portion of the water column (above the deepest mixed layer base) at both mesoscales and submesoscales and along each survey line. This high spice variance is consistent with spice variance being set at the surface [*Cole et al.*, 2010]. In the across-shore direction, greatest spice variance within the restratifying layer is found 100-200 km offshore on Lines 66.7 and 80.0, where gradients of mean salinity are largest. On Line 90.0, largest spice variance witin the restratifying layer is found just offshore of the SRR and 400-500 km from shore near the minimum in mean salinity (Figure 5.4f); spice variance decreases within the SCB in this layer, particularly at submesoscales (Figure 5.7f).

Below the seasonally restratifying layer, spice variance decreases with increasing depth to a local minimum near the 26.3 kg m$^{-3}$ isopycnal where spice variance is ore than an order of magnitude lower than in the restratifying layer (Figure 5.7). This minimum in meso- and submesoscale spice variance corresponds to the region with smallest mean large-scale spice gradient (Figure 5.4d–f). Variance increases slightly toward shore in this layer along Lines 66.7 and 80.0. On Line 90, meso- and submesoscale spice variance increases significantly in this layer within the SCB, in contrast to the restratifying layer above (Figure 5.7).

At densities of 26.6–26.7 kg m$^{-3}$, spice variance exhibits a local maximum on all three survey lines and at all observed scales. Spice variance in this layer is typically 3–5 times greater than in the minimum variance layer above but lower than in the restratifying layer. The maximum is apparent at all observed locations, but is generally strongest near the coast on each survey line. The density of this maximum in spice variance corresponds to the isopycnals with largest mean salinity gradients below the thermocline.

The state estimate also shows layers defined by spice variance at mesoscales (Figure 5.8). Along Lines 66.7, 80.0, and 90.0 (Figure 5.8a–c), the state estimate has greatest spice variance in the restratifying layer and decreasing spice variance below 26.0 kg m$^{-3}$. A local minimum in spice variance near 26.2 kg m$^{-3}$ is more apparent along Line 90.0 than Line 80.0, and no local minimum is clear along Line 66.7. A local maximum in spice variance appears along Lines 80.0 and 90.0 near the 26.6 kg m$^{-3}$ isopycnal, as in the observations. On Line 66.7, there is no clear local maximum near 26.6 kg m$^{-3}$, but spice variance at that density is highest near the coast as in the observations. The state estimate also produces layers of spice variance in areas not surveyed by the gliders and with little or no other in situ observations. Along CalCOFI Lines 73.3 (off San Simeon, California), 86.7 (off Los Angeles, California), and 93.3 (off San Diego, California), the simulation produces greatest spice variance in the restratifying layer, a local minimum in spice variance below the restratifying layer, and a local maximum in spice variance below 26.5 kg m$^{-3}$ (not shown). The state estimate has a remarkable ability to accurately capture the geography of mesoscale spice variance by only adjusting initial conditions, boundary conditions, and forcing.

Spice variance (Figure 5.8d) on the alongshore transect through the model domain (Figure 5.1) shows how the layers observed on each glider line are connected over the 525 km between Lines 66.7 and 90.0. As for the across-shore transects, spice variance is greatest in the restratifying layer all along the 1400-km alongshore transect. The layer of minimum spice variance is most prominent south of Line 90.0 and becomes difficult to identify between Lines 80.0 and 66.7, consistent with observations. The deeper layer of increased spice variance near the 26.7 kg $m^{-3}$ isopycnal can be traced from the southern boundary of the domain to near Line 66.7. Despite large-scale along-isopycnal salinity gradients being smaller in the alongshore direction (Figure 5.6b) than in the across-shore direction (Figure 5.5d–f), mesoscale spice variance is of comparable size in the alongshore direction, possibly indicating that anisotropic large-scale gradients are ultimately stirred to produce isotropic mesocale and submesoscale thermohaline structure.

### 5.3.3 Origin of Thermohaline Layers

The layers of thermohaline variance may form due to differences in source waters in each layer or as a result of differences in stirring on each layer. Variations in source waters on each layer would include the presence of different water masses in each layer, which would be related to the observed large-scale thermohaline gradients (Figure 5.4d–f), as well as smaller-scale spice variance set wherever source waters are subducted [*Cole and Rudnick*, 2011]. For similar background large-scale spice gradients on two layers, stronger stirring on one layer could produce greater spice variance on that layer. Adjoint passive tracer calculations (section 5.2.4) in the numerical state estimate allow us to investigate both of these mechanism and to show, as was inferred by *Cole and Rudnick* [2011] for layers off Hawaii, that differences in source waters are the primary mechanism for establishing the layers of thermohaline variability in the CCS.

We define objective functions (5.2) for eight tracers. To define the target region for each tracer, we prescribe weight functions, $w$, such that the vertical integral of the weight function is a Gaussian with a decorrelation scale of 50 km centered at either CalCOFI station 90.80 (384 km offshore on Line 90.0, and the intersection with the alongshore transect of Figure 5.6) or CalCOFI station 90.45 (126 km offshore on Line 90.0). The weight functions are nonzero in one of four density ranges corresponding to a layer of high or low spice variance (Table 5.1) and are uniformly weighted over those ranges. The Gaussian shapes on the upper axis of Figure 5.8c represent the vertical integral of $w$ for tracers inshore and offshore of the SCB. Thick lines along the vertical axes of Figure 5.8c represent the four density ranges. We limit our analysis to vertical integrals of tracer sensitivities, which we will denote as $\tilde{C}(x, y, t)$ since they may be thought of a past distributions of tracers.

Unrealistic negative adjoint tracer sensitivities appear as a result of numerical errors. Negative passive tracer sensitivities are unrealistic since they suggest that the presence of tracer in a particular location at a past time causes a decrease in concentration of that tracer in the target region at the end of the simulation. These negative sensitivity arise near sharp gradients of tracer. Though our weight functions in (5.2) are Gaussian in the horizontal, straining by the velocity field produces sharp gradients of tracer as the adjoint model is integrated backwards in time. As is clear in Figures 5.9 and 5.10, which have symmetric, cube-root color scales, the negative values of vertically integrated sensitivities are much smaller than the positive values. We make no attempt to correct for the negative sensitivities in our analysis.

Maps of vertically integrated tracer sensitivity, $\tilde{C}(x, y, t)$, at selected times show the history of the chosen tracers. Figure 5.9 shows the distributions of the four tracers that end up offshore of the SCB six months, one year, and 18 months before the end of the simulation. Tracer 1-off (Figure 5.9a–c), which represents the seasonally restratifying layer, is advected into the region primarily along the coast from the north, with some waters moving from 39°N to the target region within little more than six months. Waters in the low spice variance layer represented by tracer 2-off (Figure 5.9d–f) are advected into the region more slowly and from further offshore than the waters above; little of tracer 2-off is present along the coast north of Point Conception. Tracer 3-off (Figure 5.9g–i), which represents waters in the high spice variance layer below the thermocline, comes into the region from the west and south with little tracer coming from north of Point Conception. The deeper, low spice variance waters of tracer 4-off arrive in the target region slowly from the south and within the SCB (Figure 5.9j–l).

Tracers found within the SCB at the end of the simulation have long term histories that are similar to those of corresponding tracers that end up offshore of the SCB. Waters in the restratifying layer arrive in the SCB from the north along the coast (Figure 5.10a–c). Tracers on deeper isopycnals (tracers 2-in, 3-in, and 4-in) enter the SCB primarily from the south due to the presence of the SRR (Figure 5.10d–l). The distributions of tracers 2-in and 3-in eighteen months before the end of the simulation (Figure 5.10f,i) resemble the distributions of tracers 2-off and 3-off, respectively, (Figure 5.9e,h) one year before the end of the simulation, suggesting a timescale of about 6 months for waters to enter the SCB along those isopycnals. Waters along the deeper isopycnals represented by tracer 4-in are found along the coast for at least 18 months prior to the end of the simulation (Figure 5.10j–l).

Integrating the tracer distributions at each time over the cropped model domain gives the fraction of each tracer in the domain as a function of time (Figure 5.11a). For the final six months of the simulation, all tracers are entirely within the cropped domain. Over the 2.6 year simulation, the shallowest tracers (tracers 1-off and 1-in) come most from outside of the cropped domain, while progressively deeper tracers are more completely contained within the domain throughout the simulation. Tracers 1-off and 1-in, the shallowest tracers, are the last tracers to be fully contained in the cropped domain, reflecting the influence of the surface-intensified California Current. Tracer 2-in is entirely within the cropped domain several months earlier than its offshore counterpart, tracer 2-off, reflecting the additional time required for waters to recirculate into the SCB [e.g., *Lynn and Simpson*, 1987]. Tracers 3-in and 4-in are found completely within the cropped domain slightly later than tracers 3-off and 4-off, and are slightly less completely within the domain at the beginning of the simulation than their offshore counterparts. This is likely a result of tracers 3-in and 4-in being advected northward more rapidly by the poleward currents (Figure 5.5g–i) due to their target regions being closer to the coast.

From the vertically integrated distributions of the tracers at each time step (e.g., Figures 5.9 and 5.10), we calculate the center of mass, angle of the principal axes, and the variances along principal axes. The location of the center of mass, $(\bar{x}(t), \bar{y}(t))$, is given by

$$\begin{aligned} \bar{x}(t) &= \frac{\iint_{V'} x\tilde{C}(x,y,t)\,dx\,dy}{\iint_{V'} \tilde{C}(x,y,t)\,dx\,dy}, \\ \bar{y}(t) &= \frac{\iint_{V'} y\tilde{C}(x,y,t)\,dx\,dy}{\iint_{V'} \tilde{C}(x,y,t)\,dx\,dy}, \end{aligned} \tag{5.4}$$

where $V'$ is the cropped model domain. We then calculate the angle of the principal axes, $\alpha(t)$, as

$$\alpha(t) = \frac{1}{2}\arctan\left(\frac{2\iint_{V'} x'y'\tilde{C}(x,y,t)\,dx\,dy}{\iint_{V'} (x'^2 - y'^2)\tilde{C}(x,y,t)\,dx\,dy}\right), \tag{5.5}$$

where $x' = x - \bar{x}(t)$ and $y' = y - \bar{y}(t)$ are distances from the center of mass at each time calculated on an $f$-plane centered at $(\bar{x}, \bar{y})$. Variances along the principal axes are then given by

$$\begin{aligned} \sigma_x^2(t) &= \frac{\iint_{V'} x''^2\tilde{C}(x,y,t)\,dx\,dy}{\iint_{V'} \tilde{C}(x,y,t)\,dx\,dy}, \\ \sigma_y^2(t) &= \frac{\iint_{V'} y''^2\tilde{C}(x,y,t)\,dx\,dy}{\iint_{V'} \tilde{C}(x,y,t)\,dx\,dy}, \end{aligned} \tag{5.6}$$

where distances from the center of mass along the principal axes, $(x'', y'')$ are

$$\begin{pmatrix} x'' \\ y'' \end{pmatrix} = \begin{pmatrix} \cos\alpha & \sin\alpha \\ -\sin\alpha & \cos\alpha \end{pmatrix} \begin{pmatrix} x' \\ y' \end{pmatrix}. \tag{5.7}$$

We calculate the center of mass, angle of principal axes, and variances only when 90% or more of the tracer is within the cropped model domain (Figure 5.11a).

The centers of mass of each tracer distribution (Figure 5.12) trace out the mean paths taken by waters that end up offshore and inshore of the SCB at the end of the simulation. As inferred from the snapshots of tracer distributions (Figure

5.9), waters in the restratifying layer (tracer 1-off) come into the region offshore of the SCB from the north along the coast, and waters in the layer of minimum spice variance (tracer 2-off) come from somewhat more to the west. The center of mass of tracer 3-off moves primarily offshore reflecting advection from the northwest and southeast (Figure 5.9g–i). Tracer 4-off reaches the target area offshore of the SCB from the most southerly location, but still shows some eastward motion in the early months of the simulation. The center of mass of tracer 1-in reaches the target region generally from the north but enters the SCB slightly to the south of its ultimate location. The centers of mass of progressively deeper tracers reach the target region in the SCB along trajectories that include increasingly long northward segments; the center of mass of tracer 4-in reaches the target region along a path that parallels the coast for more than 2 years. The SRR (Figure 5.1) serves as an increasingly solid barrier with increasing depth so that deeper tracers must enter the SCB primarily from the south.

The orientation of the principal axes (Figure 5.11b) and variances along principal axes (Figure 5.11c–d) indicate how the past tracer distributions are spread about the center of mass at each time. Figure 5.13 shows ellipses representing the standard deviations along principal axes and centered at the center of mass as a function of time. With the exception of tracer 4-off, each tracer has a major axis that is oriented southeastward for most of its history (Figure 5.11b). Most of these tracers have major axes oriented about 25–45 degrees clockwise from east, roughly aligning with the orientation of the coast (Figure 5.13). The major axis of tracer 4-off is oriented nearly perpendicular to the coast throughout the simulation (Figure 5.13g). Variance along the major axis is typically much larger than variance along the minor axis, indicating significant anisotropy in the past tracer distributions (Figure 5.11c–d). In the final months of the simulation, the orientation of the major axis for each tracer becomes poorly defined as the specified isotropic Gaussian distribution is obtained.

As a measure of stirring and its dispersion of tracer, we calculate the growth rate of tracer variance [*Davis*, 1991]. We define an apparent diffusivity, $\kappa$, as

$$\kappa = -\frac{1}{4}\frac{d}{dt}\left(\tilde{\sigma}_x^2(t) + \tilde{\sigma}_y^2(t)\right), \tag{5.8}$$

where $\tilde{\sigma}_x^2(t)$ and $\tilde{\sigma}_y^2(t)$ are linear least-squares fits to $\sigma_x^2(t)$ and $\sigma_y^2(t)$, and the minus sign accounts for the reversal of time in the adjoint model. Since the orientation of the principal axes changes with time, we calculate apparent diffusivity based only on the total variance, though this does not account for the anisotropy of the past tracer distributions. The resulting apparent diffusivities are given in Table 5.1. Apparent diffusivities decrease with depth for tracers ending up both inshore and offshore of the SCB. The apparent diffusivities from tracers 1-off and 1-in of $1.2 \times 10^3$ m$^2$ s$^{-1}$ and $1.1 \times 10^3$ m$^2$ s$^{-1}$, respectively, are comparable to the apparent alongshore diffusivities reported from surface drifters off central California by *Davis* [1985b] and the isopycnal eddy diffusivity calculated from tracer released in the pycnocline of the North Atlantic [*Ledwell et al.*, 1998]. Apparent diffusivities are all much larger than the horizontal diffusivities of 1 m$^2$ s$^{-1}$ used in the configuration of the numerical simulation. The dispersion of tracer in the model is significantly enhanced through straining by the velocity field. The monotonic decay of $\kappa$ with depth suggests that variations in strength of stirring with depth do not account for the observed layers of high and low spice variance; the presence of persistent large-scale thermohaline gradients that can be stirred is essential to the formation of the layers.

## 5.4 Conclusions

We have used a combination of autonomous glider observations and a numerical state estimate to characterize upper ocean thermohaline structure in the CCS. With their high spatial resolution and continuous occupation of defined survey lines, glider observations resolve thermohaline structure at mesoscales and submesoscales and show the presence of discrete layers distinguished by spice variance. The state estimate reproduces these features, and, through passive tracer adjoint calculations, allows us to show that the layers have differing histories that lead to their unique thermohaline properties.

Layers defined by spice variance are observed and modeled throughout the CCS (Figures 5.7 and 5.8). Highest spice variance at mesoscales and submesoscales occurs in the seasonally restratifying layer where waters have recently been in contact with the atmosphere. Around the 26.2 kg $m^{-3}$ isopycnal, a local minimum in spice variance is found; the minimum is most prominent in the southern portion of the study region and offshore of the SCB. Near the 26.6 kg $m^{-3}$ isopycnal, we find a local maximum in spice variance. The layers of high and low spice variance are found along isopycnals with large and small mean, large-scale spice gradients, respectively, suggesting that persistent, large-scale thermohaline gradients are stirred by the velocity field to produce smaller scale thermohaline structure. Layers defined by their spice variance were previously reported by *Cole and Rudnick* [2011] in the central north Pacific, so we expect that similar features will be found throughout the ocean as the necessary observations become available.

We use adjoint passive tracers in our numerical state estimate to show that the layers defined by spice variance have differing histories. Adjoint passive tracer calculations allow us to determine the past distributions of waters that end up in specified target regions (Figures 5.9 and 5.10). Waters in the restratifying layer come into the from the north along the coast and move from 39°N to the target areas south of 34°N within as little as six months. Source waters for the minimum spice variance layer below the thermocline are somewhat further offshore than the waters above. In the layer of elevated spice variance near 26.6 kg $m^{-3}$, waters come from the west and south, and little water comes from north of Point Conception. Below this, waters move into the region slowly from the south. Tracers that end up in the SCB are influenced by the SRR which creates an increasingly solid barrier to across-shore transport with increasing depth; deeper tracers arrive in the SCB from the south along the coast, regardless of their ultimate source (Figure 5.12). Apparent diffusivities based on the variance of past tracer distributions show that stirring decreases monotonically with increasing depth, so changes in stirring with depth are not sufficient to account for the observed layering of spice variance.

As a naturally occurring passive tracer [*Veronis*, 1972; *Cole and Rudnick*, 2011], spice is a useful and readily observable variable for inferring the history of waters. In this analysis, observations of spice reveal distinct layers between the mixed layer and 500 m depth throughout the CCS. However, we have only considered mean distribution of spice variance with no accounting of possible seasonal or longer term variability. The observational dataset used here currently spans four years, so seasonal cycles are becoming reasonably well-resolved (Figure 5.2), and some interannual variability is apparent [e.g., *Todd et al.*, 2011b]. Investigation of seasonal and interannual variability in spice could reveal changes in circulation as well as stirring and mixing occurring on those timescales that could have important influences on the productivity of the rich ecosystem of the CCS.

*Acknowledgments.* Spray glider observations were supported by the Instrument Development Group at the Scripps Institution of Oceanography and the Southern California Coastal Ocean Observing System (SCCOOS). Francisco Chavez (MBARI) assisted with glider observations along Line 66.7. We gratefully acknowledge funding from the Gordon and Betty Moore Foundation, the Coastal Ocean Currents Monitoring Project (COCMP), and NOAA. Modeling and glider observations on Lines 66.7 and 90.0 are part of the Consortium on the Ocean's Role in Climate (CORC) program.

## Appendix 5.A Passive Tracer Senstivity

Here we derive the evolution of the passive tracer sensitivity in the continuous framework. The adjoint to the advection diffusion equation that governs passive tracer evolution is derived in section 5.A.1, and section 5.A.2 derives the tracer sensitivity and shows that it obeys the adjoint to the advection diffusion equation.

### 5.A.1 Derivation of the Adjoint Advection Diffusion Equation

The concentration of a passive tracer, $C(x, y, z, t)$, evolves according to an advection-diffusion equation

$$\left(\frac{\partial}{\partial t} + \vec{u} \cdot \nabla - \kappa \nabla^2\right) C = 0. \tag{5.9}$$

We consider an arbitrary variation $\delta C$ to the tracer concentration. Since the advection-diffusion operator in (5.9) is linear, the variation $\delta C$ is also governed by an advection-diffusion equation

$$\left(\frac{\partial}{\partial t} + \vec{u}\cdot\nabla - \kappa\nabla^2\right)\delta C = 0. \tag{5.10}$$

We consider the inner product of (5.10) with the adjoint variable $g(x, y, z, t)$. The adjoint variable is the solution to the adjoint differential equation that we are deriving. The form of $g(x, y, z, t)$ is found in section 5.A.2. We take the inner product of two fields to be the product of the two fields integrated over the domain, so we have

$$\int_{t_i}^{t_f}\int_0^X\int_0^Y\int_{-Z}^0 g\left(\frac{\partial}{\partial t} + \vec{u}\cdot\nabla - \kappa\nabla^2\right)\delta C\,dz\,dy\,dx\,dt = 0, \tag{5.11}$$

where $[t_i, t_f] \times [0, X] \times [0, Y] \times [-Z, 0]$ is the model domain.

Green's identity [see *Lanczos*, 1961] states that for any linear differential operator, $\mathcal{L}$, we can find another uniquely determined operator, $\mathcal{L}^\dagger$, such that, for any pair of function $f$ and $g$ that are sufficiently differentiable and satisfy appropriate boundary conditions, the following relation is satisfied:

$$\int g\mathcal{L}f\,dx = \int f\mathcal{L}^\dagger g\,dx. \tag{5.12}$$

when the definite integrals are extended over the entire domain. $\mathcal{L}^\dagger$ is the adjoint operator associated with $\mathcal{L}$, and $g$ is the adjoint variable introduced previously. Applying Green's identity to (5.11), we have

$$\begin{aligned}
&\int_{t_i}^{t_f}\int_0^X\int_0^Y\int_{-Z}^0 g\left(\frac{\partial}{\partial t} + \vec{u}\cdot\nabla - \kappa\nabla^2\right)\delta C\,dz\,dy\,dx\,dt \\
&= \int_{t_i}^{t_f}\int_0^X\int_0^Y\int_{-Z}^0 \delta C\left(\frac{\partial}{\partial t} + \vec{u}\cdot\nabla - \kappa\nabla^2\right)^\dagger g\,dz\,dy\,dx\,dt \\
&= 0.
\end{aligned} \tag{5.13}$$

We proceed by integrating each term on the left hand side of (5.13) by parts to obtain the form of the adjoint to the advection-diffusion operator.

For the term with $\frac{\partial}{\partial t}$, we have

$$\begin{aligned}
&\int_{t_i}^{t_f}\int_0^X\int_0^Y\int_{-Z}^0 g\frac{\partial}{\partial t}\delta C\,dz\,dy\,dx\,dt \\
&\quad= \int_0^X\int_0^Y\int_{-Z}^0\int_{t_i}^{t_f} g\frac{\partial}{\partial t}\delta C\,dt\,dz\,dy\,dx \\
&\quad= \int_0^X\int_0^Y\int_{-Z}^0 \left[g\delta C|_{t_i}^{t_f} - \int_{t_i}^{t_f}\delta C\frac{\partial}{\partial t}g\,dt\right]dz\,dy\,dx \\
&\quad= \int_{t_i}^{t_f}\int_0^X\int_0^Y\int_{-Z}^0 \delta C\left(-\frac{\partial}{\partial t}\right)g\,dz\,dy\,dx\,dt, \qquad (5.14)
\end{aligned}$$

where the boundary term from the integration by parts vanishes if $\delta C|_{t=t_i} = g|_{t=t_f} = 0$.

For the part of the advective term with $\frac{\partial}{\partial x}$, we have

$$\begin{aligned}
&\int_{t_i}^{t_f}\int_0^X\int_0^Y\int_{-Z}^0 gu\frac{\partial}{\partial x}\delta C\,dz\,dy\,dx\,dt \\
&\quad= \int_{t_i}^{t_f}\int_0^Y\int_{-Z}^0\int_0^X gu\frac{\partial}{\partial x}\delta C\,dx\,dz\,dy\,dt \\
&\quad= \int_{t_i}^{t_f}\int_0^Y\int_{-Z}^0 \left[gu\delta C|_0^X - \int_0^X \delta C\frac{\partial}{\partial x}(gu)\,dx\right]dz\,dy\,dt \\
&\quad= \int_{t_i}^{t_f}\int_0^Y\int_{-Z}^0 \left[gu\delta C|_0^X - \int_0^X \delta Cu\frac{\partial}{\partial x}g\,dx - \int_0^X \delta Cg\frac{\partial}{\partial x}u\,dx\right]dz\,dy\,dt \\
&\quad= \int_{t_i}^{t_f}\int_0^X\int_0^Y\int_{-Z}^0 \left[\delta C\left(-u\frac{\partial}{\partial x}\right)g - \delta Cg\frac{\partial}{\partial x}u\right]dz\,dy\,dx\,dt, \qquad (5.15)
\end{aligned}$$

where the boundary term from the integration by parts vanishes if $g|_{x=0} = g|_{x=X} = 0$. The portions of the advective term in (5.13) with $\frac{\partial}{\partial y}$ and $\frac{\partial}{\partial z}$ give analogous results. The second term in the integrand of (5.15) becomes part of a term with $\nabla\cdot\vec{u}$, which vanishes for incompressible fluids.

For the diffusive term with $\frac{\partial^2}{\partial x^2}$, we apply integration by parts twice to get

$$\begin{aligned}
&\int_{t_i}^{t_f}\int_0^X\int_0^Y\int_{-Z}^0 g\left(-\kappa\frac{\partial^2}{\partial x^2}\right)\delta C\,dz\,dy\,dx\,dt \\
&= \int_{t_i}^{t_f}\int_0^Y\int_{-Z}^0\int_0^X g\left(-\kappa\frac{\partial^2}{\partial x^2}\right)\delta C\,dx\,dz\,dy\,dt \\
&= \int_{t_i}^{t_f}\int_0^Y\int_{-Z}^0\left[-g\kappa\frac{\partial}{\partial x}\delta C\bigg|_0^X + \int_0^X\frac{\partial g}{\partial x}\kappa\frac{\partial}{\partial x}\delta C\,dx\right]dz\,dy\,dt \\
&= \int_{t_i}^{t_f}\int_0^Y\int_{-Z}^0\left[-g\kappa\frac{\partial}{\partial x}\delta C\bigg|_0^X + \kappa\delta C\frac{\partial g}{\partial x}\bigg|_0^X - \int_0^X\frac{\partial^2 g}{\partial x^2}\kappa\delta C\,dx\right]dz\,dy\,dt \\
&= \int_{t_i}^{t_f}\int_0^X\int_0^Y\int_{-Z}^0 \delta C\left(-\kappa\frac{\partial^2}{\partial x^2}\right)g\,dz\,dy\,dx\,dt, \qquad (5.16)
\end{aligned}$$

where the boundary terms vanish if we additionally have $\frac{\partial g}{\partial x}\big|_{x=0} = \frac{\partial g}{\partial x}\big|_{x=X} = 0$. The portions of the diffusive term in (5.13) with $\frac{\partial^2}{\partial y^2}$ and $\frac{\partial^2}{\partial z^2}$ yield similar results.

Collecting terms in (5.14–5.16) and their counterparts that are not shown and substituting into (5.13), we have

$$\begin{aligned}
&\int_{t_i}^{t_f}\int_0^X\int_0^Y\int_{-Z}^0 \delta C\left(-\frac{\partial}{\partial t} - \vec{u}\cdot\nabla - \kappa\nabla^2\right)g\,dz\,dy\,dx\,dt \\
&\quad = \int_{t_i}^{t_f}\int_0^X\int_0^Y\int_{-Z}^0 \delta C\left(\frac{\partial}{\partial t} + \vec{u}\cdot\nabla - \kappa\nabla^2\right)^{\dagger} g\,dz\,dy\,dx\,dt. \qquad (5.17)
\end{aligned}$$

Since $\delta C$ is arbitrary, the equality in (5.17) holds only if the adjoint to the advection-diffusion operator is given by $-\frac{\partial}{\partial t} - \vec{u}\cdot\nabla - \kappa\nabla^2$. It follows that the adjoint variable $g$ evolves according to

$$-\frac{\partial g}{\partial t} = \vec{u}\cdot\nabla g + \kappa\nabla^2 g, \qquad (5.18)$$

subject to $g|_{t=t_f} = 0$, $g|_\Omega = 0$, and $\hat{n}\cdot\nabla g|_\Omega = 0$, where $\Omega$ is the boundary of the domain and $\hat{n}$ is the unit vector normal to the boundary. The adjoint variable evolves backwards in time according to a velocity field that is oppositely directed relative to the forward equation, but diffusion continues to destroy gradients.

### 5.A.2 Passive Tracer Sensitivity

We now derive the sensitivity of passive tracer in a target region at the end of the simulation to tracer distributions at earlier times, and show that the passive tracer sensitivity is the adjoint variable $g$ in section 5.A.1. Our derivation in the continuous framework closely follows the derivation by *Talagrand and Courtier* [1987] for variational assimilation. *Fukumori et al.* [2004] derive the passive tracer sensitivity in finite difference form.

We may write the advection-diffusion equation (5.9) as $\frac{\partial C}{\partial t} = \mathcal{L}[C(t)]$, where $\mathcal{L} \equiv -\vec{u} \cdot \nabla + \kappa \nabla^2$ is now specified to be the advection-diffustion operator. We let $\langle \, , \rangle$ denote the inner product between two functions defined as the integral over the spatial domain of the product of the two functions. A variation $\delta C(t)$ to the tracer concentration at time $t$ results in a variation $\delta C(\tau)$ at each time $\tau > t$ to the tracer concentration. The resulting variation $\delta J$ to the objective function (5.2) is

$$\delta J = \int_t^{t_f} \left\langle \frac{\partial G}{\partial C}(\tau), \delta C(\tau) \right\rangle d\tau, \tag{5.19}$$

where $\frac{\partial G}{\partial C}$ is the derivative of $G[C(t), t]$ with respect to $C(t)$ with $x$, $y$, $z$, and $t$ held constant. As in section 5.A.1, the variation $\delta C(\tau)$ is governed by the advection-diffusion equation (5.10). Solutions for $\delta C(\tau)$ can be written in terms of $\delta C(t)$ as

$$\delta C(\tau) = R(t, \tau) \delta C(t), \tag{5.20}$$

where $R(\tau, t)$ is the resolvent of $\mathcal{L}$ from time $t$ to time $\tau$ [see *Talagrand and Courtier*, 1987].

Substituting (5.20) into (5.19) and applying Green's identity (5.12) to the resulting inner product gives

$$\delta J = \int_t^{t_f} \left\langle [R(t, \tau)]^\dagger \frac{\partial G}{\partial C}(\tau), \delta C(t) \right\rangle d\tau, \tag{5.21}$$

The application of Green's identity has removed the $\tau$-dependent operator from $\delta C(t)$, which may now be written outside of the integral to give

$$\delta J = \left\langle \int_t^{t_f} [R(t, \tau)]^\dagger \frac{\partial G}{\partial C}(\tau) \, d\tau, \delta C(t) \right\rangle, \tag{5.22}$$

from which we recognize that the sensitivity of the objective function with respect to tracer concentration at time $t$ is

$$\frac{\partial J}{\partial C(t)} = \int_t^{t_f} [R(t, \tau)]^\dagger \frac{\partial G}{\partial C}(\tau) \, d\tau. \tag{5.23}$$

Now we recall the adjoint (5.18) to the advection-diffusion equation that was derived in section 5.A.1, and we write it as

$$-\frac{\partial g}{\partial t} = \mathcal{L}^\dagger[g(t)], \tag{5.24}$$

where $g(t)$ is the adjoint varaible and $\mathcal{L}^\dagger$ is the adjoint of the operator $\mathcal{L}$, the form of which was derived in section 5.A.1. *Talagrand and Courtier* [1987] prove that the resolvent of the adjoint equation from time $t_2$ to time $t_1$ is the adjoint of the resolvent of the forward equation from time $t_1$ to time $t_2$. Therefore we can write (5.23) as

$$\frac{\partial J}{\partial C(t)} = \int_t^{t_f} R^\dagger(\tau, t)\frac{\partial G}{\partial C}(\tau)\, d\tau, \tag{5.25}$$

where $R^\dagger(\tau, t)$ is the resolvent of the adjoint operator $\mathcal{L}^\dagger$ backwards in time from $\tau$ to $t$.

Now consider the inhomogeneous adjoint equation

$$-\frac{\partial g}{\partial t} = \mathcal{L}^\dagger[g(t)] + \frac{\partial G}{\partial C}(t), \tag{5.26}$$

where the partial derivative of the function $G$ that defines the objective function provides a forcing to the adjoint advection-diffusion equation. The solution to (5.24) subject to $g(t_f) = 0$ is

$$g(t) = \int_t^{t_f} R^\dagger(\tau, t)\frac{\partial G}{\partial C}(\tau)\, d\tau. \tag{5.27}$$

We verify this solution by substitution and using the properties of the resolvent $R^\dagger$ that $R^\dagger(t,t) = I$ where $I$ is the identity operator and $\frac{\partial}{\partial t}R^\dagger(t,t') = \mathcal{L}^\dagger R^\dagger(t,t')$ [*Talagrand and Courtier*, 1987]. Substituting (5.27) into the left-hand-side of (5.26) gives

$$\begin{aligned}
-\frac{\partial g}{\partial t} &= -\frac{\partial}{\partial t}\int_t^{t_f} R^\dagger(\tau, t)\frac{\partial G}{\partial C}(\tau)\, d\tau \\
&= \int_t^{t_f} \mathcal{L}^\dagger R^\dagger(\tau, t)\frac{\partial G}{\partial C}(\tau)\, d\tau + R^\dagger(t,t)\frac{\partial G}{\partial C}(t) \\
&= \mathcal{L}^\dagger \underbrace{\int_t^{t_f} R^\dagger(\tau, t)\frac{\partial G}{\partial C}(\tau)\, d\tau}_{=g(t)} + \frac{\partial G}{\partial C}(t) \\
&= \mathcal{L}^\dagger[g(t)] + \frac{\partial G}{\partial C}(t). 
\end{aligned} \tag{5.28}$$

Since the expressions for $\frac{\partial J}{\partial C(t)}$ (5.25) and $g(t)$ (5.27) are the same, it follows that $\frac{\partial J}{\partial C(t)}$ is the adjoint variable $g(t)$. The passive tracer sensitivity is governed by the adjoint to the advection diffusion equation, and the sensitivity of $J$ to prior tracer concentration is found by integrating the partial derivative of the function $G$ backwards in time using the adjoint equation.

**Table 5.1**: Initialization Regions, Names, and Apparent Diffusivities for Passive Tracers[a]

| Density Range | Spice | Name | | $\kappa$ ($m^2$ $s^{-1}$) | |
|---|---|---|---|---|---|
| (kg $m^{-3}$) | Variance | offshore | inshore | offshore | inshore |
| 24.9–25.2 | high | 1-off | 1-in | $12 \times 10^2$ | $11 \times 10^2$ |
| 26.25–26.35 | low | 2-off | 2-in | $9.8 \times 10^2$ | $7.6 \times 10^2$ |
| 26.6–26.7 | high | 3-off | 3-in | $6.4 \times 10^2$ | $2.8 \times 10^2$ |
| 26.9–27.0 | low | 4-off | 4-in | $2.6 \times 10^2$ | $1.6 \times 10^2$ |

[a] Apparent diffusivities, $\kappa$, calculated by least-squares fitting to time series of total variance of tracer distributions.

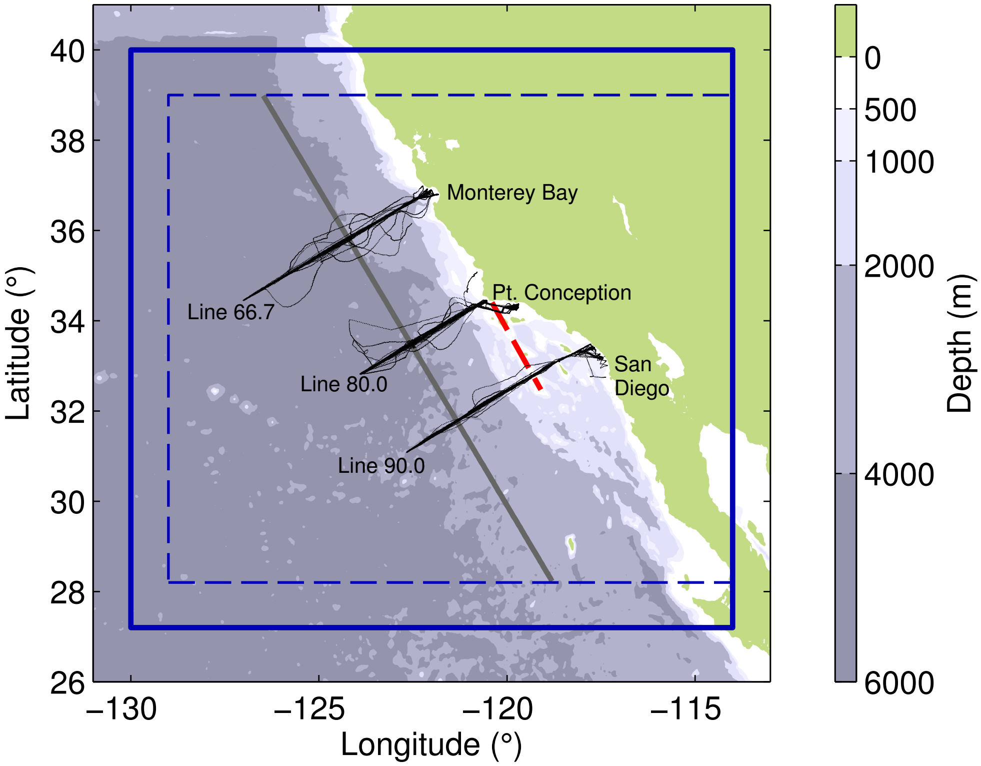

**Figure 5.1**: Tracks of all glider deployments along CalCOFI Lines 66.7, 80.0, and 90.0 (black) with bathymetry in color. The blue box denotes the full domain of the numerical simulation, and the dashed blue box denotes the cropped portion of the model domain used for analysis. The grey line shows the alongshore transect examined in the simulation. The dashed red line denotes the Santa Rosa Ridge, which is the offshore boundary of the Southern California Bight.

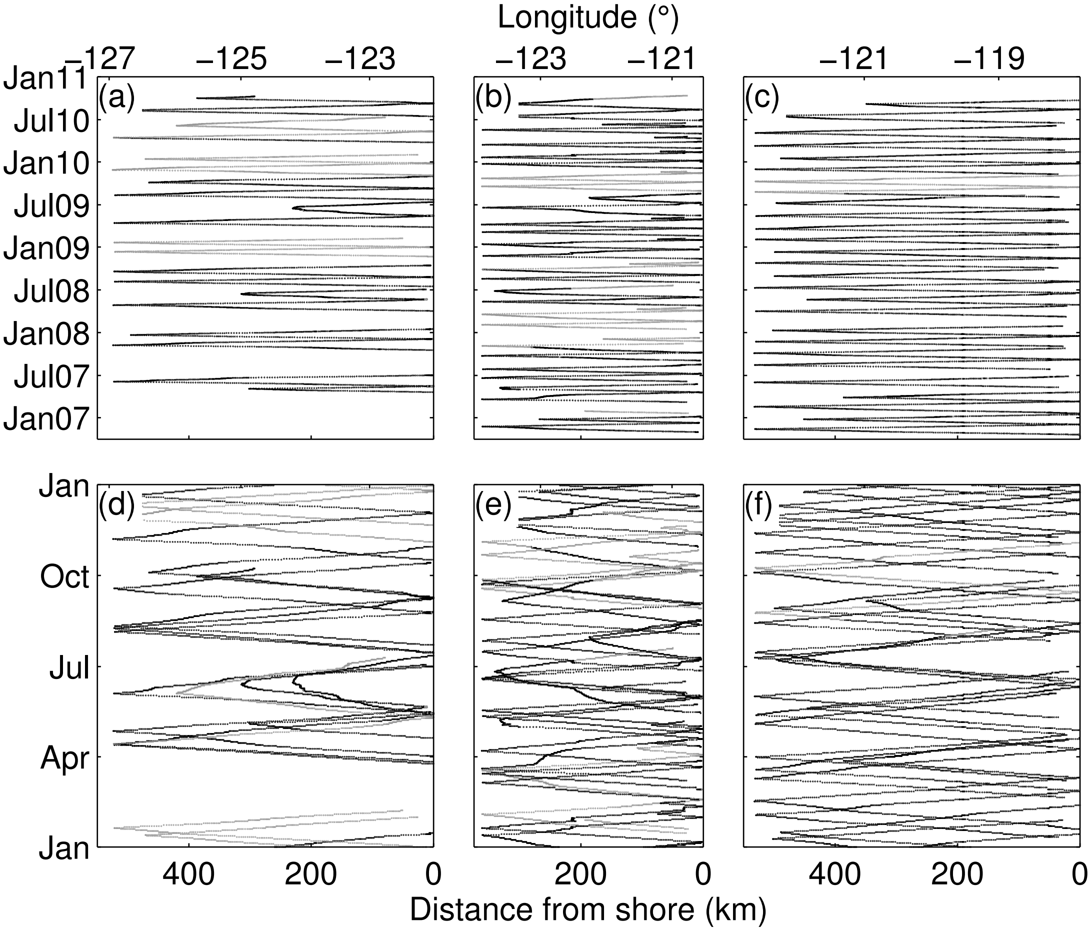

**Figure 5.2**: Across-shore and temporal sampling patterns along CalCOFI Lines (a,d) 66.7, (b,e) 80.0, and (c,f) 90.0. In (d-f), the sampling pattern is plotted versus time of year to highlight coverage at seasonal scales. Each point denotes the location of a glider profile. Black points indicate profiles with valid ADP-derived current estimates; profiles without ADP-derived current estimates are grey. Tick marks on the upper axis of each panel indicate longitude while tick marks on the lower axes indicate distance from shore.

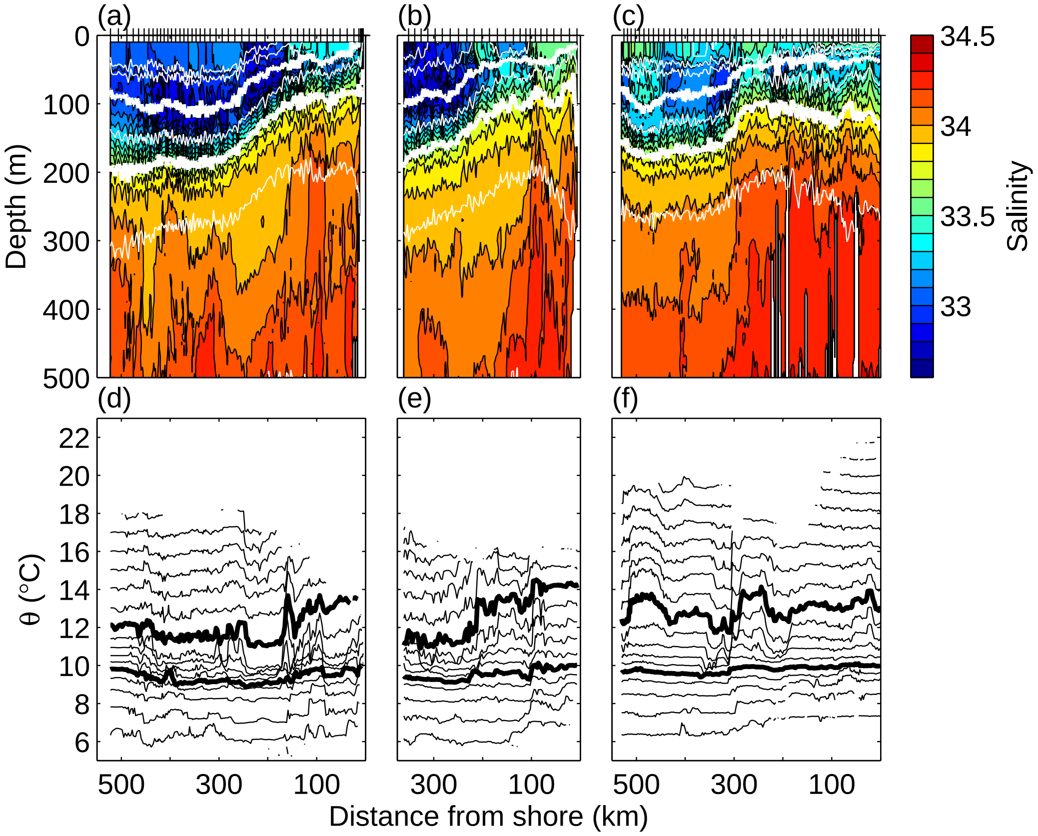

**Figure 5.3**: Example transects of (a-c) salinity (colors) and density (white contours) and (d-f) potential temperature along isopycnals. (a,d) Line 66.7. (b,e) Line 80.0. (c,f) Line 90.0. The 25.0 and 26.0 kg m$^{-3}$ isopycnals are bold. Tick marks on the upper-most axes denote the locations of glider profiles; only every fifth profile location is shown for clarity.

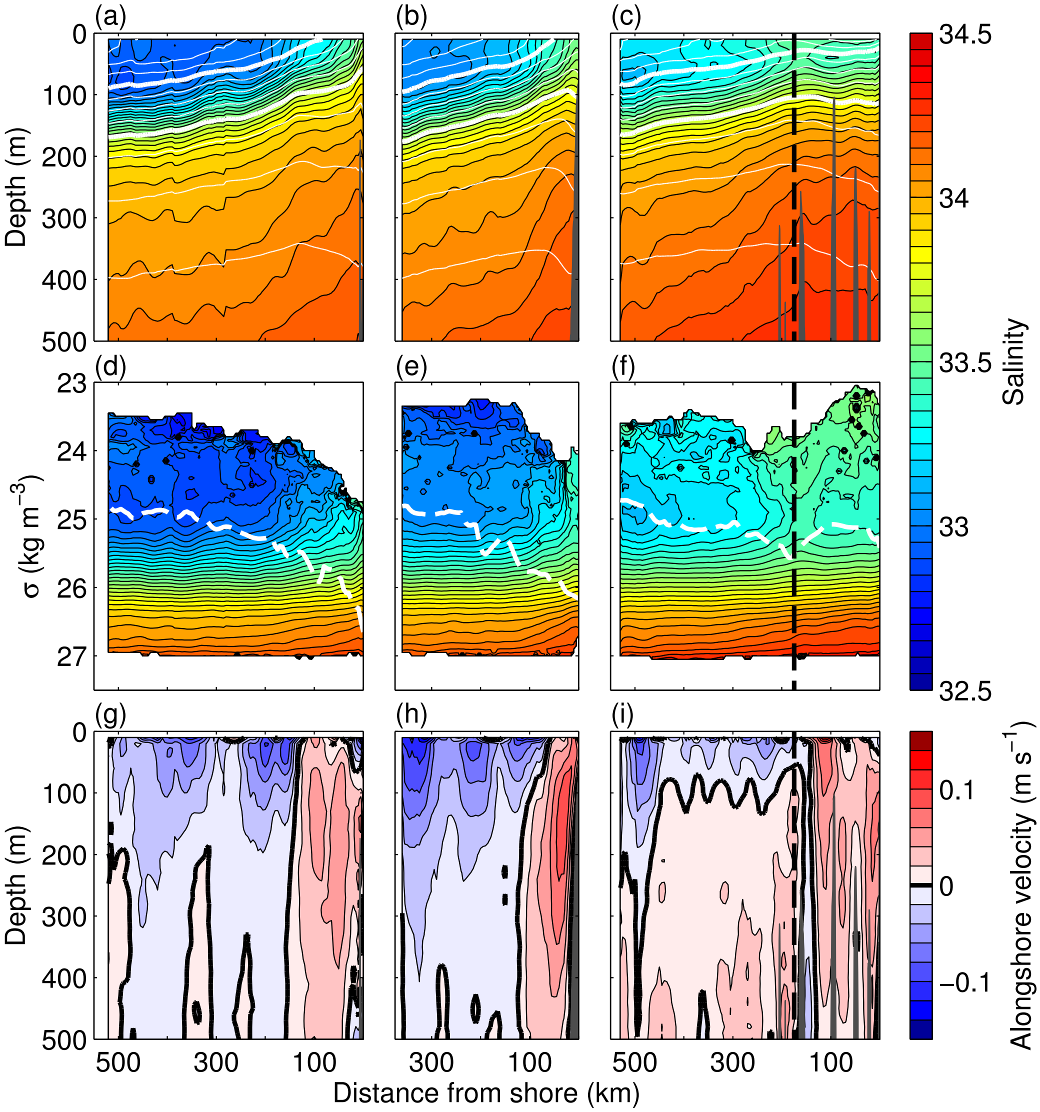

**Figure 5.4**: Mean (a-c) salinity (color) and density (white contours) on depth surfaces, (d-f) mean salinity on isopycnals, and (g-i) mean alongshore velocity from (a,d,g) Line 66.7, (b,e,h) Line 80.0, and (c,f,i) Line 90.0. In (a-c), density contours are drawn every 0.25 kg m$^{-3}$ with the 25.0 and 26.0 kg m$^{-3}$ isopycnals bold. The dashed white lines in (d-f) indicate the densest outcropping isopycnal. Positive alongshore velocities are poleward. Bathymetry along the survey lines is shaded in (a-c) and (g-i). The dashed black lines in (c,f,i) indicate the SRR.

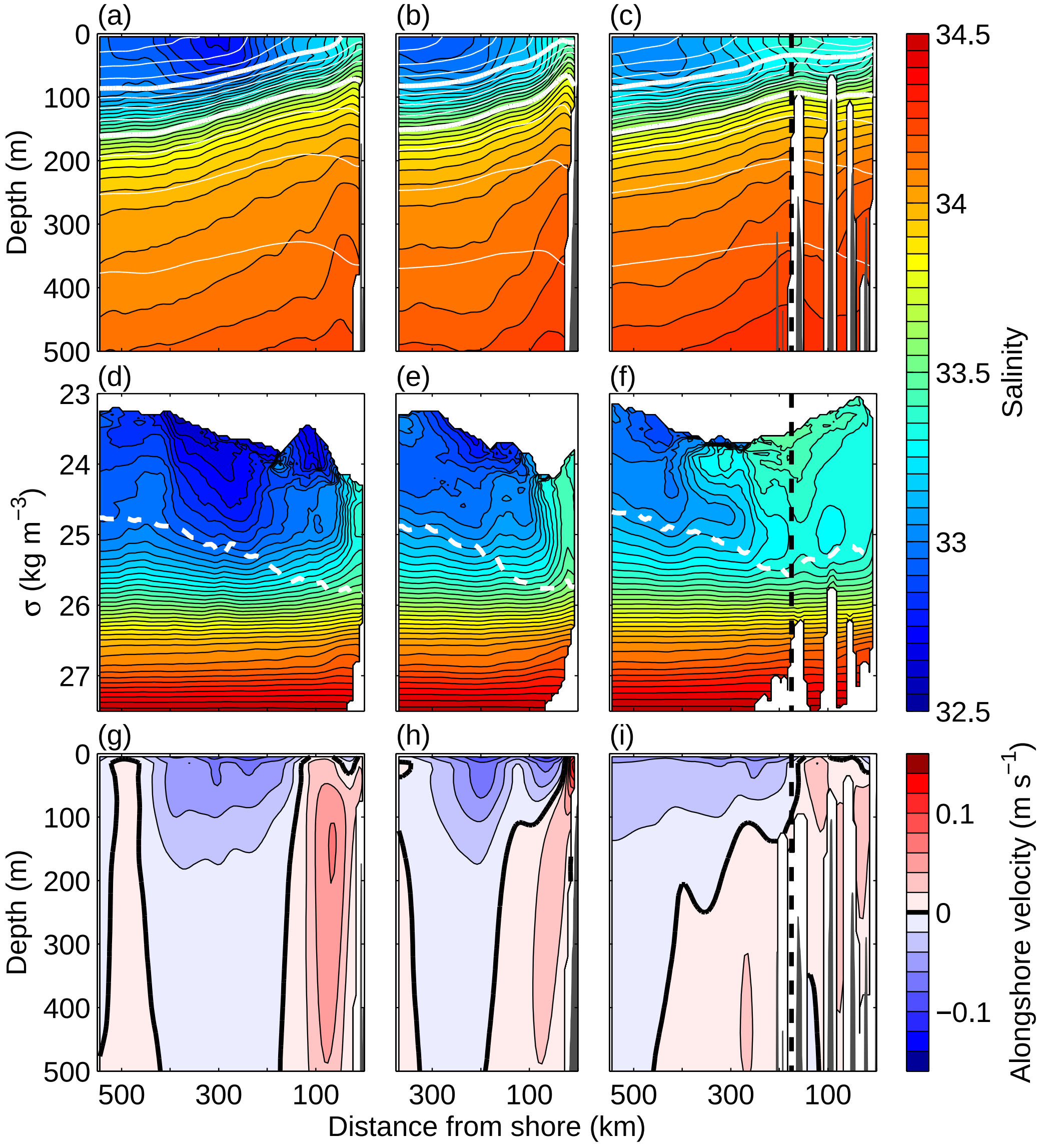

**Figure 5.5**: As in Figure 5.4, but for means of the numerical simulation from 1 January 2007 to 30 July 2009.

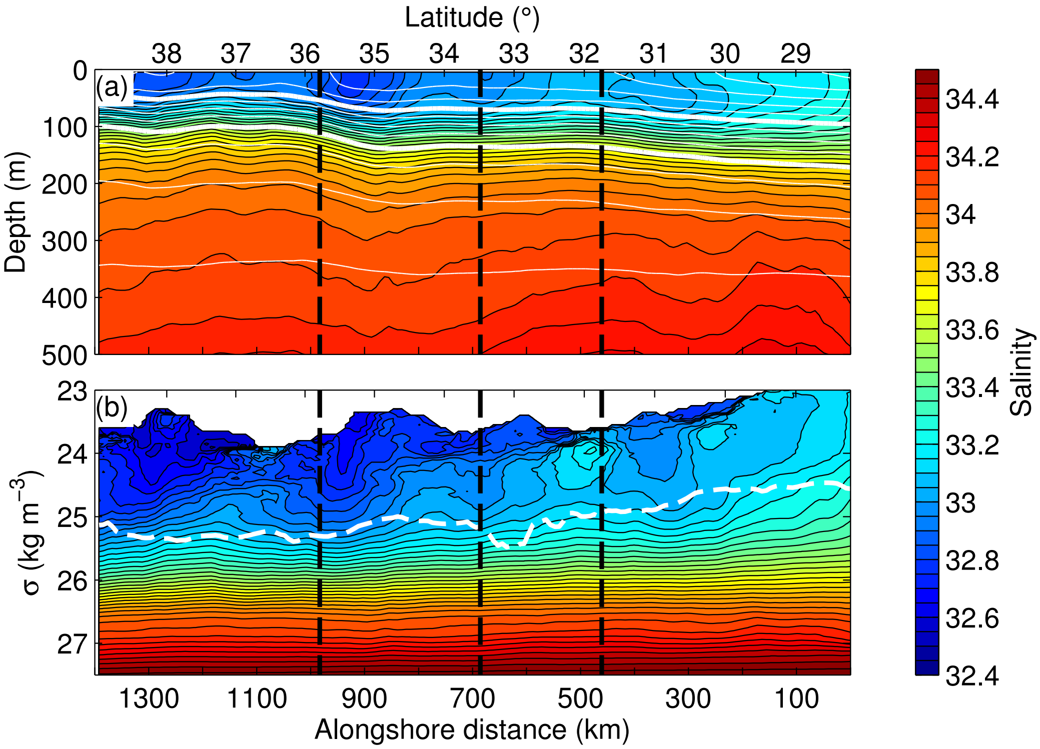

**Figure 5.6**: Mean salinity as a function of depth (a) and potential density (b) on the alongshore transect through the numerical simulation (Figure 5.1). Alongshore distance increases from south to north. White contours in (a) show mean density with contours drawn every 0.25 kg m$^{-3}$ and the 25.0 and 26.0 kg m$^{-3}$ isopycnals bold. The dashed white line in (b) indicates the densest outcropping isopycnal. Dashed black lines denote the intersections with Lines 66.7, 80.0, and 90.0 at station 80 along each line.

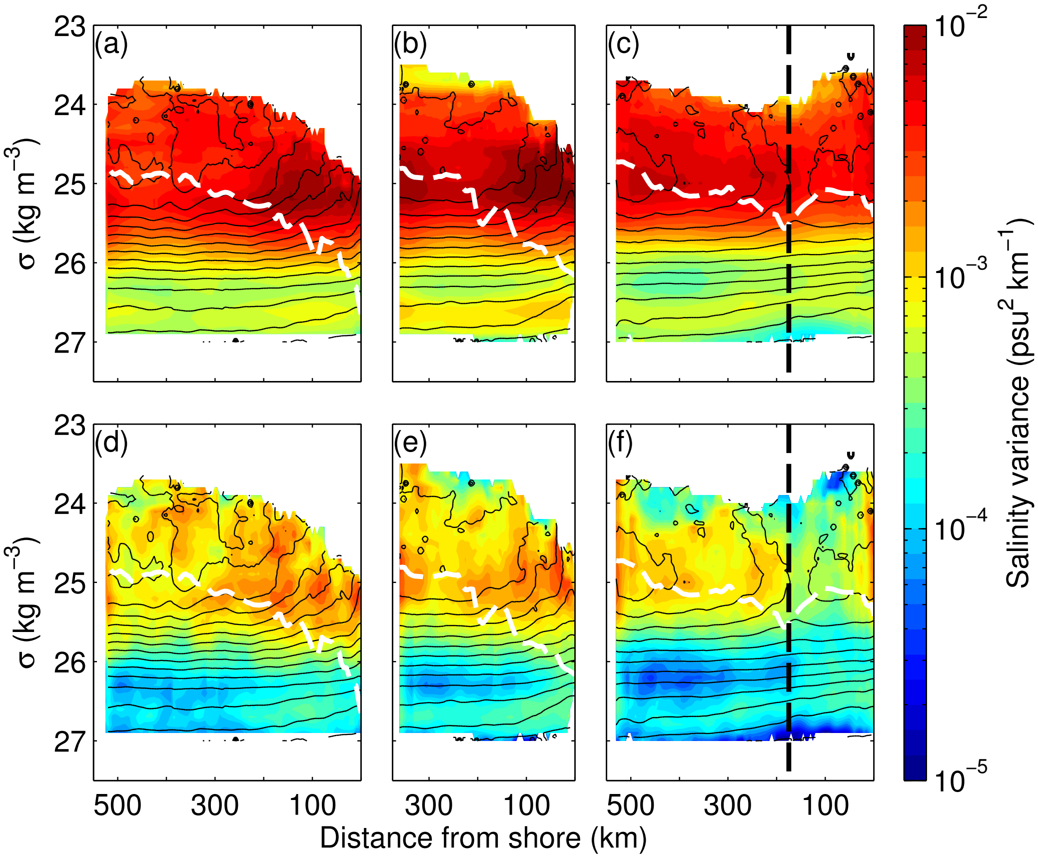

**Figure 5.7**: (a-c) Mesoscale (30–200 km wavelength) and (d-f) submesoscale (6–30 km wavelength) salinity variance as a function of density and across-shore distance on (a,d) Line 66.7, (b,e) Line 80.0, and (c,f) Line 90.0. Black contours show mean salinity with a contour interval of 0.1. The dashed white lines indicate the densest outcropping isopycnal as in Figure 5.4d-f. The dashed black lines in (c,f) indicate the location of the SRR.

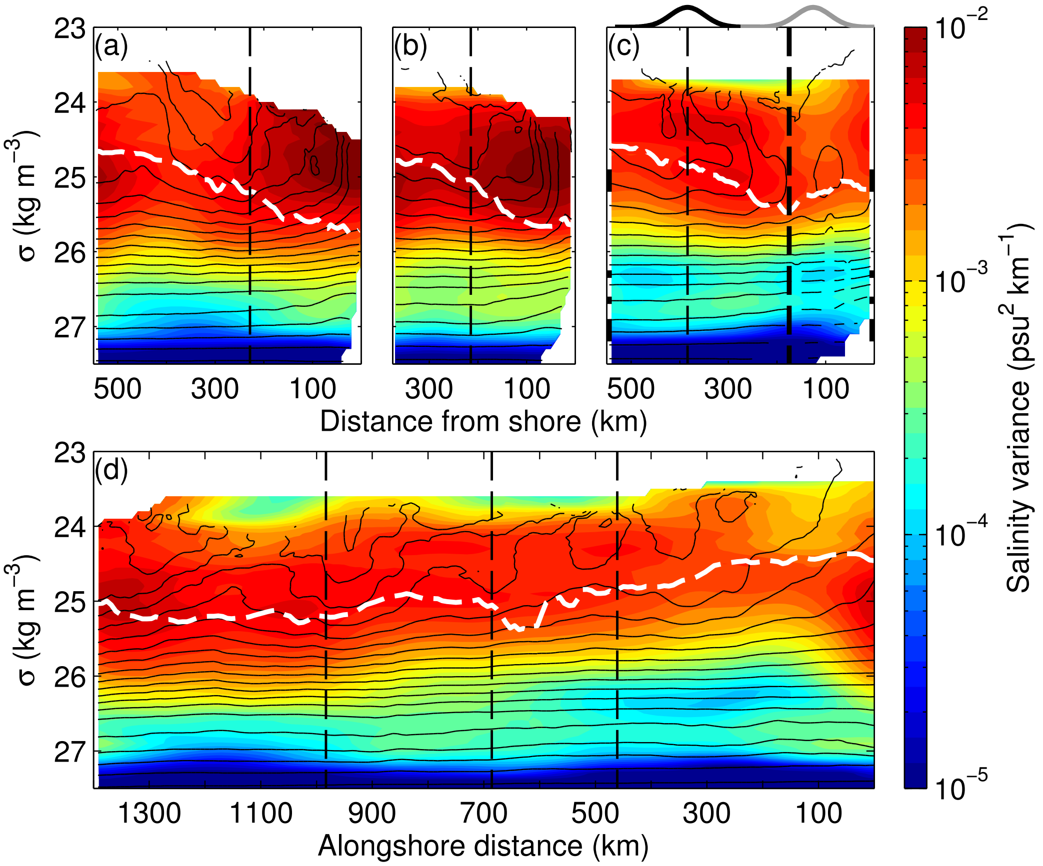

**Figure 5.8**: Mesoscale salinity variance as a function of density in the numerical simulation. (a-c) Lines 66.7, 80.0, and 90.0, respectively, for comparison to Figure 5.7a-c. (d) Salinity variance on the alongshore transect shown in Figures 5.1 and 5.6 with alongshore distance increasing toward the north. The dashed white lines indicate the densest outcropping isopycnals. The thin dashed lines in each panel indicate the intersections of Lines 66.7, 80.0, and 90.0 with the alongshore section. The heavy dashed line in (c) indicates the Santa Rosa Ridge. Only mesoscale variance is shown because the model does not resolve submesoscales well. In (c), the Gaussian shapes on the top axis indicate the profile of the vertically integrated weight functions, $w$, for tracers with target regions offshore of the SCB (black) and within the SCB (grey), and the heavy marks along the vertical axes indicate the four density ranges used to define $w$ (Table 5.1).

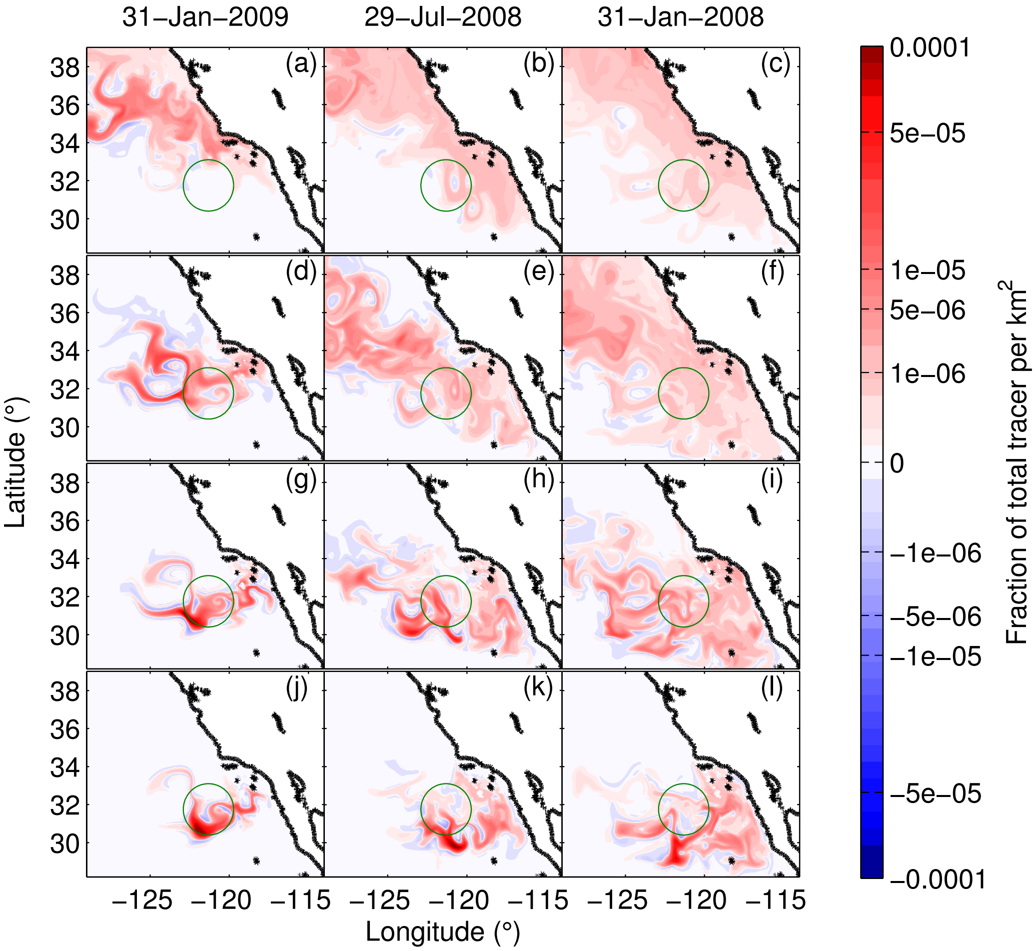

**Figure 5.9**: Vertically integrated tracer distribution (a,d,g,j) six months, (b,e,h,k) one year, and (c,f,i,l) eighteen months before end of simulation for tracers with target regions offshore of the SRR on Line 90.0. Each row represents a particular tracer, organized from shallowest to deepest. Total quantity is normalized by the amount on 24 July 2009. Green circles indicate the target region.

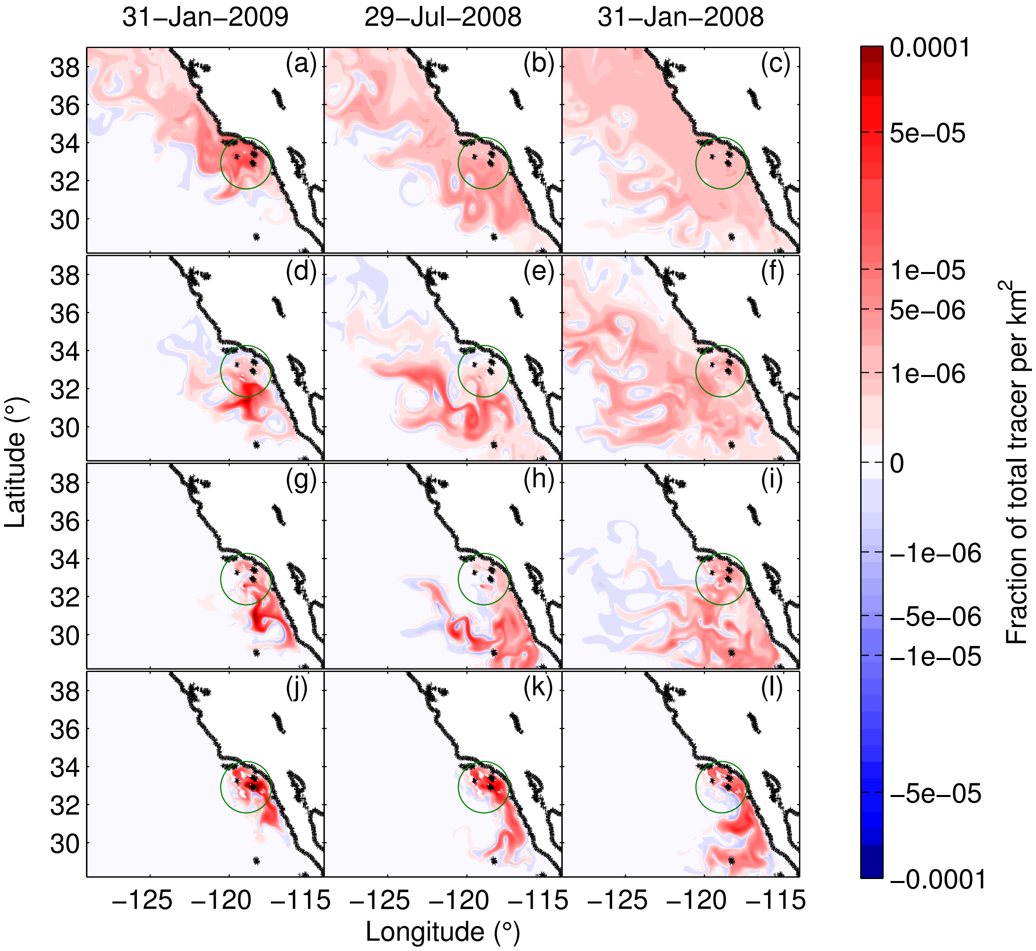

**Figure 5.10**: Vertically integrated tracer distribution (a,d,g,j) six months, (b,e,h,k) one year, and (c,f,i,l) eighteen months before end of simulation for tracers with target regions inshore of the SRR on Line 90.0. Each row represents a particular tracer, organized from shallowest to deepest. Total quantity is normalized by the amount on 24 July 2009. Green circles indicate the target region.

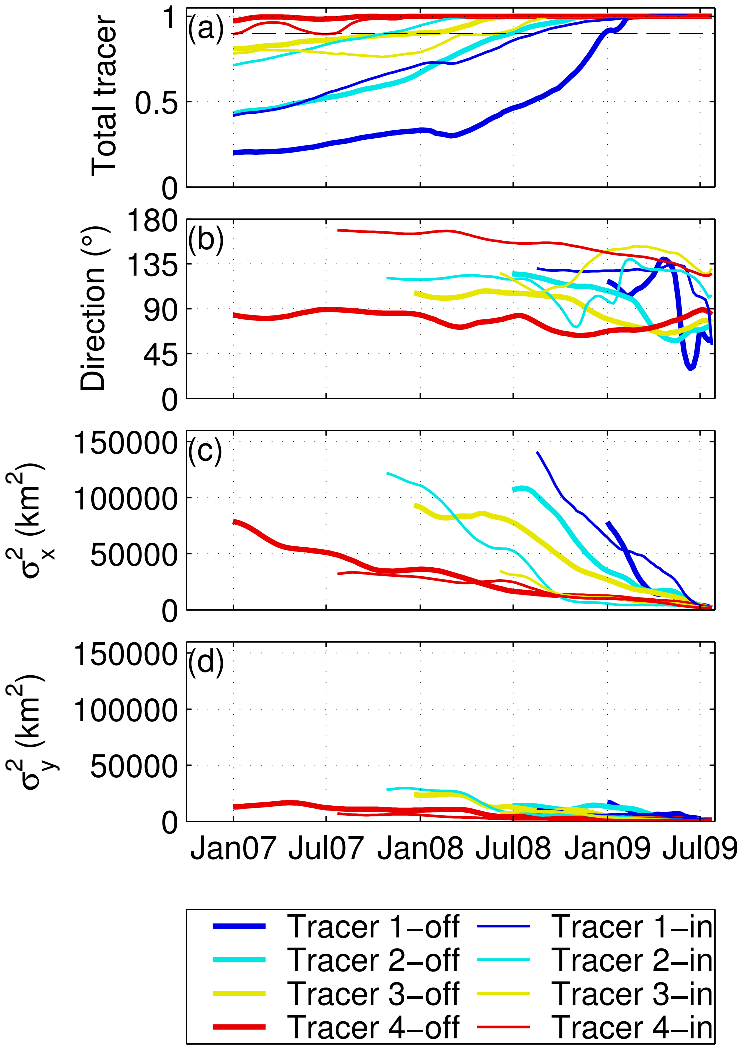

**Figure 5.11**: Time series of tracer properties. (a) Fractional quantity of tracer within the cropped model domain. Total quantity is normalized by the amount on 24 July 2009. The dashed black line indicates the threshold for calculate center of mass, angle of principal axes, and standard deviations along principal axes. (b) Orientation of principal axes of tracer distributions clockwise from north. (c,d) Variances of tracer distributions along the principal axes.

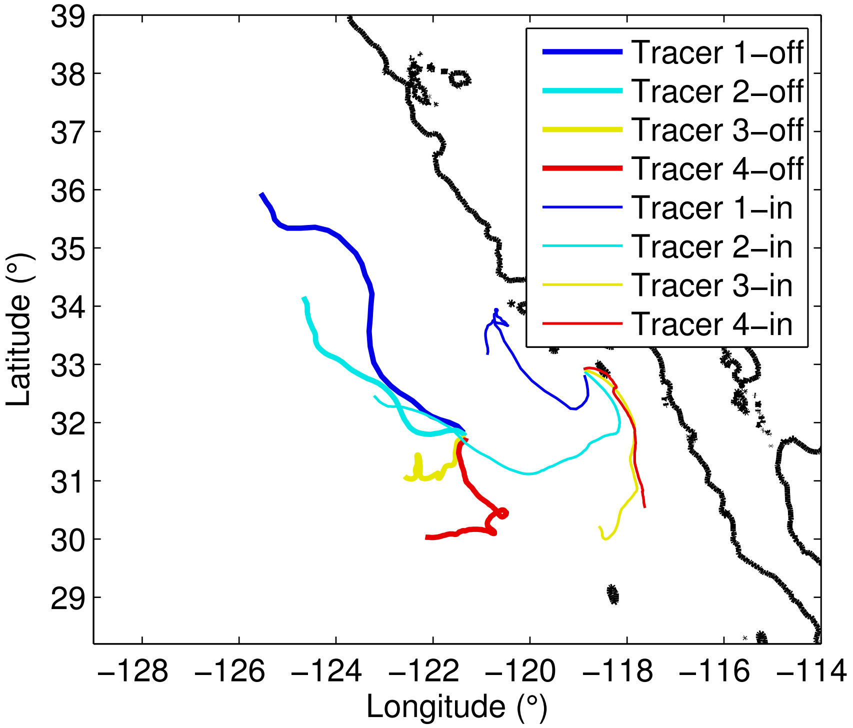

**Figure 5.12**: Location of center of mass of each tracer. Tracers with target regions offshore of the SRR are shown with thick lines; tracers with target regions within within the SCB are shown with dashed lines. Colors correspond to tracers along different isopycnal levels. Location of the center of mass only shown when the amount of tracer in the cropped domain is at least 90% of the amount at the next to last time step (Figure 5.11a).

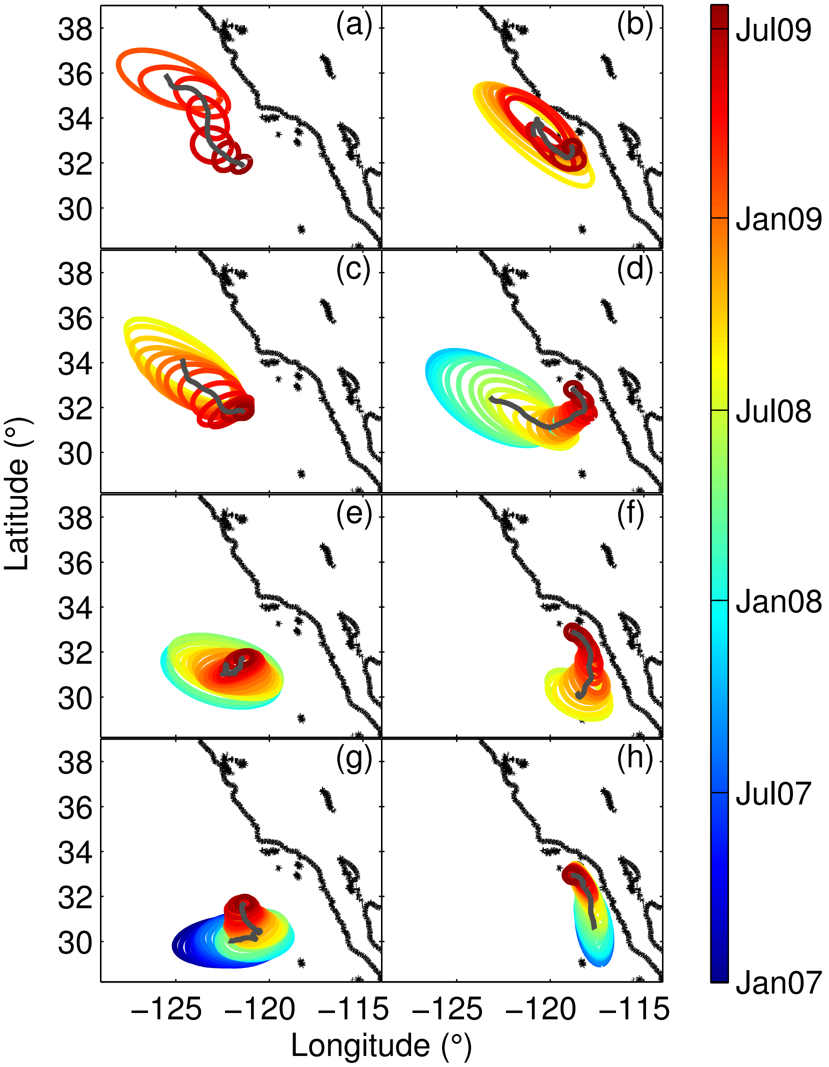

**Figure 5.13**: Variance ellipses of each tracer as a function of time. (a,c,e,g) Tracers with target regions offshore of the SCB, from shallowest to deepest. (b,d,f,h) Tracers with target regions inshore of the SCB, from shallowest to deepest. Ellipses are centered at the center of mass and shown for tracer distributions every 30 days. The dark grey lines show the location of the center of mass as in Figure 5.12. Ellipses are shown only when the amount of tracer in the cropped domain is at least 90% of the amount at the next to last time step (Figure 5.11a).

# References

Antonov, J. I., R. A. Locarnini, T. P. Boyer, A. V. Mishonov, and H. E. Garcia (2006), *World Ocean Atlas 2005, vol. 2, Salinity*, *NOAA Atlas NESDIS*, vol. 62, edited by S. Levitus et al., p. 182, NOAA, Silver Spring, Md.

Auad, G., A. Parés-Sierra, and G. K. Vallis (1991), Circulation and Energetics of a Model of the California Current System, *J. Phys. Oceanogr.*, *21*, 1534–1552.

Bakun, A., and C. S. Nelson (1991), The Seasonal Cycle of Wind-Stress Curl in Subtropical Eastern Boundary Current Regions, *J. Phys. Oceanogr.*, *21*, 1815–1834.

Boehm, A. B., B. F. Sanders, and C. D. Winant (2002), Cross-Shelf Transport at Huntington Beach. Implications for the Fate of Sewage Discharged through an Offshore Ocean Outfall, *Environ. Sci. Technol.*, *36*, 1899–1906, doi: 10.1021/es0111986.

Bograd, S. J., T. K. Chereskin, and D. Roemmich (2001), Transport of mass, heat, salt, and nutrients in the southern California Current System–Annual cycle and interannual variability, *J. Geophys. Res.*, *106*(C5), 9255–9275, doi: 10.1029/1999JC000165.

Botsford, L. W., C. A. Lawrence, E. P. Dever, A. Hastings, and J. Largier (2006), Effects of variable winds on biological productivity on continental shelves in coastal upwelling systems, *Deep Sea Res. Part II*, *53*, 3116–3140, doi:10.1016/j.dsr2.2006.07.011.

Bray, N. A., A. Keyes, and W. M. L. Morawitz (1999), The California Current system in the Southern California Bight and the Santa Barbara channel, *J. Geophys. Res.*, *104*(C4), 7695–7714, doi:10.1029/1998JC900038.

Bretherton, F. P., R. E. Davis, and C. B. Fandry (1976), A technique for objective analysis and design of oceanographic experiments applied to MODE-73, *Deep-Sea Res.*, *23*, 559–582.

Brinton, E., and A. Townsend (2003), Decadal variability in abundances of the dominant euphausiid species in southern sectors of the California Current, *Deep-Sea Res.*, *50*(14-16), 2449–2472, doi:10.1016/S0967-0645(03)00126-7.

Caldeira, R. M. A., P. Marchesiello, N. P. Nezlin, P. M. DiGiacomo, and J. C. McWilliams (2005), Island wakes in the Southern California Bight, *J. Geophys. Res.*, *110*, C11012, doi:10.1029/2004JC002675.

Castelao, R., S. Glenn, and O. Schofield (2010), Temperature, salinity, and density variability in the central Middle Atlantic Bight, *J. Geophys. Res.*, *115*, C10005, doi:10.1029/2009JC006082.

Chavez, F. P., J. T. Pennington, C. G. Castro, J. P. Ryan, R. P. Michisaki, B. Schlining, P. Walz, K. R. Buck, A. McFadyen, and C. A. Collins (2002), Biological and chemical consequences of the 1997-1998 El Niño in central California waters, *Prog. Oceanogr.*, *54*, 205–232.

Chelton, D. B. (1984), Seasonal Variability of Alongshore Geostrophic Velocity Off Central California, *J. Geophys. Res.*, *89*(C3), 3473–3486.

Chelton, D. B., and R. E. Davis (1982), Monthly Mean Sea-Level Variability Along the West Coast of North America, *J. Phys. Oceanogr.*, *12*, 757–784.

Chelton, D. B., and M. G. Schlax (1996), Global Observations of Oceanic Rossby Waves, *Science*, *272*, 234–238.

Chelton, D. B., M. G. Schlax, R. M. Samelson, and R. A. de Szoeke (2007), Global observations of large oceanic eddies, *Geophys. Res. Lett.*, *34*, L15606, doi:10.1029/2007GL030812.

Chelton, D. B., M. G. Schlax, and R. M. Samelson (2011), Global Observations of Nonlinear Mesoscale Eddies, *Prog. Oceanogr.*, doi:10.1016/j.pocean.2011.01.002, in press.

Chereskin, T. K., and M. Trunnell (1996), Correlation scales, objective mapping, and absolute geostrophic flow in the California Current, *J. Geophys. Res.*, *101*(C10), 22,619–22,629, doi:10.1029/96JC02004.

Chhak, K., and E. Di Lorenzo (2007), Decadal variations in the California Current upwelling cells, *Geophys. Res. Lett.*, *34*, L14604, doi:10.1029/2007GL030203.

Cole, S. T., and D. L. Rudnick (2011), Spatial and temporal modulation of thermohaline structure, *J. Geophys. Res.*, submitted.

Cole, S. T., D. L. Rudnick, and J. A. Colosi (2010), Seasonal evolution of upper-ocean horizontal structure and the remnant mixed layer, *J. Geophys. Res.*, *115*, C04012, doi:doi:10.1029/2009JC005654.

Davis, R. E. (1985a), Drifter Observations of Coastal Surface Currents During CODE: The Method and Descriptive View, *J. Geophys. Res.*, *90*(C3), 4741–4755.

Davis, R. E. (1985b), Drifter Observations of Coastal Surface Currents During CODE: The Statistical and Dynamical Views, *J. Geophys. Res.*, *90*(C3), 4756–4772.

Davis, R. E. (1991), Lagrangian ocean studies, *Annu. Rev. Fluid Mech.*, *23*, 43–64.

Davis, R. E. (2010), On the coastal-upwelling overturning cell, *J. Mar. Res.*, *68*, 369–385.

Davis, R. E., C. C. Eriksen, and C. P. Jones (2002), Autonomous Bouyancy-Driven Underwater Gliders, in *Technology and Applications of Autonomous Underwater Vehicles*, edited by G. Griffiths, pp. 37–58, Taylor and Francis, Philadelphia, Pa.

Davis, R. E., M. D. Ohman, D. L. Rudnick, J. T. Sherman, and B. A. Hodges (2008), Glider surveillence of physics and biology in the southern California Current System, *Limnol. Oceanogr.*, *53*(5, part 2), 2151–2168, doi: 10.4319/lo.2008.53.5_part_2.2151.

Debnath, L. (2007), On linear and nonlinear Rossby waves in an ocean, *J. Math. Anal. Appl.*, *333*, 164–190, doi:10.1016/j.jmaa.2006.11.014.

Dever, E. P., and C. D. Winant (2002), The evolution and depth structure of shelf and slope temperatures and velocities during the 1997-1998 El Niño near Point Conception, California, *Prog. Oceanogr.*, *54*, 77–103.

Di Lorenzo, E. (2003), Seasonal dynamics of the surface circulation in the Southern California Current System, *Deep Sea Res. Part II*, *50*, 2371–2388.

DiGiacomo, P. M., and B. Holt (2001), Satellite observations of small coastal ocean eddies in the Southern California Bight, *J. Geophys. Res.*, *106*(C10), 22,521–22,543.

Dong, C., and J. C. McWilliams (2007), A numerical study of island wakes in the Southern California Bight, *Cont. Shelf Res.*, *27*(9), 1233–1248, doi: 10.1016/j.csr.2007.01.016.

Emery, W. J., and K. Hamilton (1985), Atmospheric Forcing of Interannual Variability in the Northeast Pacific Ocean: Connections With El Niño, *J. Geophys. Res.*, *90*(C1), 857–868.

Enfield, D. B., and J. S. Allen (1980), On the Structure and Dynamics of Monthly Mean Sea Level Anomalies along the Pacific Coast of North and South America, *J. Phys. Oceanogr.*, *10*, 557–578.

Eppley, R. W., E. H. Renger, and W. G. Harrison (1979), Nitrate and Phytoplankton Production in Southern California Coastal Waters, *Limnol. Oceanogr.*, *24*(3), 483–494.

Eriksen, C. C., T. J. Osse, R. D. Light, T. Wen, T. W. Lehman, P. L. Sabin, J. W. Ballard, and A. M. Chiodi (2001), Seaglider: A Long-Range Autonomous Underwater Vehicle for Oceanographic Research, *IEEE J. Oceanic Eng.*, *26*(4), 424–436.

Errico, R. M. (1997), What Is an Adjoint Model?, *Bulletin of the American Meteorological Society*, *78*(11), 2577–2591.

Ferrari, R., and D. L. Rudnick (2000), Thermohaline variability in the upper ocean, *J. Geophys. Res.*, *105*(C7), 16,857–16,883.

Forget, G. (2010), Mapping Ocean Observations in a Dynamical Framework: A 2004–2006 Ocean Atlas, *J. Phys. Oceanogr.*, *40*, 1201–1221, doi: 10.1175/2009JPO4043.1.

Fukumori, I., T. Lee, B. Cheng, and D. Menemenlis (2004), The Origin, Pathway, and Destination of Niño-3 Water Estimated by a Simulated Passive Tracer and Its Adjoint, *J. Phys. Oceanogr.*, *34*, 582–604.

Gao, S., T. Qu, and I. Fukumori (2011), Effects of mixing on the subduction of South Pacific waters identified by a simulated passive tracer and its adjoint, *Dynam. Atmos. Oceans*, *51*, 45–54, doi:10.1016/j.dynatmoce.2010.10.002.

Garfield, N., C. A. Collins, R. G. Paquette, and E. Carter (1999), Lagrangian Exploration of the California Undercurrent, 1992–95, *J. Phys. Oceanogr.*, *29*(4), 560–583, doi:10.1175/1520-0485(1999)029<0560:LEOTCU>2.0.CO;2.

Gay, P. S., and T. K. Chereskin (2009), Mean structure and seasonal variability of the poleward undercurrent off southern California, *J. Geophys. Res.*, *114*, C02007, doi:10.1029/2008JC004886.

Gill, A. E. (1982), *Atmosphere-Ocean Dynamics*, *Int. Geophys. Ser.*, vol. 30, Academic Press, San Diego, Calif.

Gourdeau, L., W. S. Kessler, R. E. Davis, J. T. Sherman, C. Maes, and E. Kestenare (2008), Zonal Jets Entering the Coral Sea, *J. Phys. Oceanogr.*, *38*, 715–725, doi:10.1175/2007JPO3780.1.

Hamilton, P., B. H. Jones, J. Largier, M. A. Noble, L. Rosenfeld, and J. Xu (2004), Methodology, pp. 2–8, U. S. Geol. Surv., Reston, Va.

Heimbach, P., C. Hill, and R. Giering (2005), An efficient exact adjoint of the parallel MIT General Circulation Model, generated via automatic differentiation, *Future Gener. Comput. Syst.*, *21*, 1356–1371, doi:10.1016/j.future.2004.11.010.

Hickey, B. M. (1979), The California Current System–Hypotheses and facts, *Prog. Oceanogr.*, *8*, 191–279.

Hickey, B. M. (1992), Circulation over the Santa Monica-San Pedro Basin and Shelf, *Prog. Oceanogr.*, *30*(1-4), 37–115.

Hickey, B. M., E. L. Dobbins, and S. E. Allen (2003), Local and remote forcing of currents and temperature in the central Southern California Bight, *J. Geophys. Res.*, *108*(C3), 3081, doi:10.1029/2000JC000313.

Hodges, B. A., and D. L. Rudnick (2006), Horizontal variability in chlorophyll fluorescence and potential temperature, *Deep-Sea Research I*, *53*, 1460–1482.

Hodur, R. M. (1997), The Naval Research Laboratory's Coupled Ocean/Atmosphere Mesoscale Prediction System (COAMPS), *Mon. Weather Rev.*, *125*, 1414–1430.

Huyer, A., P. M. Kosro, S. J. Lentz, and R. C. Beardsley (1989), Poleward flow in the California Current system, in *Poleward Flows Along Eastern Ocean Boundaries*, *Coastal Estuarine Stud. Ser.*, vol. 34, edited by S. J. Neshyba et al., pp. 142–156, Springer, New York.

Jones, B. H., M. Noble, and T. Dickey (2002), Hydrographic and particle distributions over the Palos Verde Continental Shelf: Spatial, seasonal and daily variability, *Cont. Shelf Res.*, *22*, 945–965.

Kiefer, D. A. (1973), Fluorescence Properties of Natural Phytoplankton Populations, *Mar. Biol.*, *22*, 263–269.

Klein, P., and B. L. Hua (1990), The mesoscale variability of the sea surface temperature: An analytical and numerical model, *J. Mar. Res.*, *48*, 729–763.

Lanczos, C. (1961), *Linear Differential Operators*, Van Nostrand, New York, NY.

Lavaniegos, B. E., and M. D. Ohman (2007), Coherence of long-term variations of zooplankton in two sectors of the California Current System, *Prog. Oceanogr.*, *75*, 42–69, doi:10.1016/j.pocean.2007.07.002.

Lavaniegos, B. E., L. C. Jiménez-Pérez, and G. Gaxiola-Castro (2002), Plankton response to El Niño 1997-1998 and La Niña 1999 in the southern region of the California Current, *Prog. Oceanogr.*, *54*, 33–58.

Ledwell, J. R., A. J. Watson, and C. S. Law (1998), Mixing of a tracer in the pycnocline, *J. Geophys. Res.*, *103*, 21,499–21,529.

Lee, T., and M. J. McPhaden (2010), Increasing intensity of El Niño in the central-equatorial Pacific, *Geophys. Res. Lett.*, *37*, L14603, doi:10.1029/2010GL044007.

Lee, T., W. R. Hobbs, J. K. Willis, D. Halkides, I. Fukumori, E. M. Armstrong, A. K. Hayashi, W. T. Liu, W. Patzert, and O. Wang (2010), Record warming in the South Pacific and western Antarctica associated with the strong central-Pacific El Niño in 2009-10, *Geophys. Res. Lett.*, *37*, L19704, doi: 10.1029/2010GL044865.

Locarnini, R. A., A. V. Mishonov, J. I. Antonov, T. P. Boyer, and H. E. Garcia (2006), *World Ocean Atlas 2005, vol. 1, Temperature*, *NOAA Atlas NESDIS*, vol. 61, edited by S. Levitus et al., p. 182, NOAA, Silver Spring, Md.

Lynn, R. J., and S. J. Bograd (2002), Dynamic evolution of the 1998–1999 El Niño-La Niña cycle in the southern California Current System, *Prog. Oceanogr.*, *54*, 59–75.

Lynn, R. J., and J. J. Simpson (1987), The California Current System: The Seasonal Variability of its Physical Characteristics, *J. Geophys. Res.*, *92*, 12,947–12,966.

Lynn, R. J., and J. J. Simpson (1990), The Flow of the Undercurrent Over the Continental Borderland off Southern California, *J. Geophys. Res.*, *95*, 12,995–13,008.

Marshall, J., C. Hill, L. Perelman, and A. Adcroft (1997a), Hydrostatic, quasi-hydrostatic, and nonhydrostatic ocean modeling, *J. Geophys. Res.*, *101*, 5733–5752.

Marshall, J., A. Adcroft, C. Hill, L. Perelman, and C. Heisey (1997b), A finite-volume, incompressible Navier Stokes model for studies of the ocean on parallel computers, *J. Geophys. Res.*, *102*, 5753–5766.

McGillicuddy, D. J., A. R. Robinson, D. A. Siegel, H. W. Jannasch, R. Johnson, T. D. Dickey, J. McNeil, A. F. Michaels, and A. H. Knap (1998), Influence of mesoscale eddies on new production in the Sargasso Sea, *Nature*, *394*(6690), 263–266.

McPhaden, M. J. (1999), Genesis and Evolution of the 1997-1998 El Niño, *Science*, *283*, 950–954, doi:10.1126/science.283.5404.950.

Meyers, S. D., A. Melsom, G. T. Mitchum, and J. J. O'Brien (1998), Detection of the fast Kelvin Wave teleconnection due to El Niño-Southern Oscillation, *J. Geophys. Res.*, *103*(C12), 27,655–27,663.

Moore, A. M., H. G. Arango, E. D. Lorenzo, A. J. Miller, and B. D. Cornuelle (2009), An Adjoint Sensitivity Analysis of the Southern California Current Circulation and Ecosystem, *J. Phys. Oceanogr.*, *39*, 702–720, doi: 10.1175/2008JPO3740.1.

Munk, W. (1981), Internal Waves and Small-Scale Processes, in *Evolution of Physical Oceanography–Scientific Surveys in Honor of Henry Stommel*, edited by B. Warren and C. Wunsch, chap. 9, pp. 264–291, Mass. Inst. of Technol., Boston.

Neshyba, S. J., C. N. K. Mooers, R. L. Smith, and R. T. Barber (Eds.) (1989), *Poleward Flows Along Eastern Ocean Boundaries*, *Coastal Estuarine Stud. Ser.*, vol. 34, Springer, New York.

OCSD (2007), 2005-2006 Ocean monitoring annual report, Orange County Sanitation Dist., Fountain Valley, Calif.

Owen, R. W. (1980), Eddies of the California Current System: Physical and Ecological Characteristics, in *The California Islands: Proceedings of a Multidisciplinary Symposium*, edited by D. Power, pp. 237–263, Santa Barbara Mus. of Nat. Hist., Santa Barbara, Calif.

Perry, M. J., B. S. Sackmann, C. C. Eriksen, and C. M. Lee (2008), Seaglider observations of blooms and subsurface chlorophyll maxima off the Washington coast, *Limnol. Oceanogr.*, *53*(5, part 2), 2169–2179, doi: 10.4319/lo.2008.53.5_part_2.2169.

Philander, S. G. H. (1983), El Niño Southern Oscillation phenomena, *Nature*, *302*, 295–301.

Pierce, S. D., R. L. Smith, P. M. Kosro, J. A. Barth, and C. D. Wilson (2000), Continuity of the poleward undercurrent along the eastern boundary of the mid-latitude north Pacific, *Deep Sea Res. Part II*, *47*, 811–829, doi:10.1016/S0967-0645(99)00128-9.

Pollard, R., and J. Read (1989), A Method for Calibrating Shipmounted Acoustic Doppler Profilers and the Limitations of Gyro Compasses, *J. Atmos. Ocean. Technol.*, *6*, 859–865.

Pope, S. B. (2000), *Turbulent Flows*, Cambridge Univ. Press, New York.

Ramp, S. R., J. L. McClean, C. A. Collins, A. J. Semtner, and K. A. S. Hays (1997), Observations and modeling of the 1991-1992 El Niño signal off central California, *J. Geophys. Res.*, *102*(C3), 5553–5582, doi:10.1029/96JC03050.

Roberts, P. J. W. (1999), Modeling Mamala Bay outfall plumes. I: Near field, *J. of Hydraul. Eng. ASCE*, *125*(6), 564–573.

Roemmich, D. (1989), Mean transport of mass, heat, salt and nutrients in southern California coastal waters: implications for primary production and nutrient cycling, *Deep-Sea Res.*, *36*, 1359–1378.

Roemmich, D., and J. McGowan (1995), Climatic warming and the decline of zooplankton in the California Current, *Science*, *267*(5202), 1324–1326.

Rudnick, D. L., and S. T. Cole (2011), On sampling the ocean using underwater gliders, *J. Geophys. Res.*, submitted.

Rudnick, D. L., and R. Ferrari (1999), Compensation of horizontal temperature and salinity gradients in the ocean mixed layer, *Science*, *283*(5401), 526–529.

Rudnick, D. L., R. E. Davis, C. C. Eriksen, D. M. Fratantoni, and M. J. Perry (2004), Underwater gliders for ocean research, *Mar. Technol. Soc. J.*, *38*, 73–84.

Rykaczewski, R. R., and D. M. Checkley (2008), Influence of ocean winds on the pelagic ecosystem in upwelling regions, *Proceedings of the National Academy of Sciences of the United States of America*, *105*(6), 1965–1970, rykaczewski, Ryan R. Checkley, David M., Jr.

Schwing, F. B., T. Murphree, L. deWitt, and P. M. Green (2002), The evolution of oceanic and atmospheric anomalies in the northeast Pacific during the El Niño and La Niña events of 1995-2001, *Prog. Oceanogr.*, *54*, 459–491.

Schwing, F. B., N. A. Bond, S. J. Bograd, T. Mitchell, M. A. Alexander, and N. Mantua (2006), Delayed coastal upwelling along the US West Coast in 2005: A historical perspective, *Geophys. Res. Lett.*, *33*(22), 5.

Sherman, J., R. E. Davis, W. B. Owens, and J. Valdes (2001), The autonomous underwater glider “Spray”, *IEEE J. Oceanic Eng.*, *26*(4), 437–446.

Simpson, J. J. (1984), El Niño-induced onshore transport in the California Current during 1982-1983, *Geophys. Res. Lett.*, *11*(3), 233–236.

Song, H., A. J. Miller, B. D. Cornuelle, and E. Di Lorenzo (2011), Changes in upwelling and its water sources in the California Current System driven by different wind forcing, *Dynam. Atmos. Oceans*, in press.

Strub, P. T., and C. James (2000), Altimeter-derived variability of surface velocities in the California Current System: 2. Seasonal circulation and eddy statistics, *Deep Sea Res. Part II*, *47*(5-6), 831–870.

Strub, P. T., and C. James (2002), The 1997-1998 oceanic El Niño signal along the southeast and northeast Pacific boundaries–an altimetric view, *Prog. Oceanogr.*, *54*, 439–458.

Sverdrup, H. U., and R. H. Fleming (1941), The waters off the coast of southern California, March to July 1937, *Scripps Inst. Oceanogr. Bull.*, *4*, 261–378.

Talagrand, O., and P. Courtier (1987), Variational assimilation of meteorological observations with the adjoint vorticity equation. I: Theory, *Q. J. R. Meteorol. Soc.*, *113*, 1311–1328.

Todd, R. E., D. L. Rudnick, and R. E. Davis (2009), Monitoring the greater San Pedro Bay region using autonomous underwater gliders during fall of 2006, *J. Geophys. Res.*, *114*, C06001, doi:10.1029/2008JC005086.

Todd, R. E., D. L. Rudnick, M. R. Mazloff, R. E. Davis, and B. D. Cornuelle (2011a), Poleward flows in the southern California Current System: Glider observations and numerical simulation, *J. Geophys. Res.*, *116*, C02026, doi: 10.1029/2010JC006536.

Todd, R. E., D. L. Rudnick, R. E. Davis, and M. D. Ohman (2011b), Underwater gliders reveal rapid arrival of El Niño effects off California's coast, *Geophys. Res. Lett.*, *38*, L03609, doi:10.1029/2010GL046376.

Torrence, C., and G. P. Compo (1998), A practical guide to wavelet analysis, *Bull. Am. Meteorol. Soc.*, *79*, 61–78.

Veneziani, M., C. Edwards, and A. Moore (2009), A central California coastal ocean modeling study: 2. Adjoint sensitivities to local and remote forcing mechanisms, *J. Geophys. Res.*, *114*, C04020, doi:10.1029/2008JC004775.

Veronis, G. (1972), On Properties of Seawater Defined by Temperature, Salinity, and Pressure, *J. Mar. Res.*, *30*(2), 227–255.

Visbeck, M. (2002), Deep velocity profiling using lowered acoustic Doppler current profilers: Bottom track and inverse solutions, *J. Atmos. Ocean. Technol.*, *19*(5), 794–807.

White, W. B., C.-K. Tai, and J. DiMento (1990), Annual Rossby Wave Characteristics in the California Current Region from the GEOSAT Exact Repeat Mission, *J. Phys. Oceanogr.*, *20*, 1297–1311.

Wooster, W. S., and J. H. Jones (1970), California Undercurrent Off Northern California, *J. Mar. Res.*, *28*(2), 235–250.

Wu, Y. C., L. Washburn, and B. H. Jones (1994), Buoyant Plume Dispersion in a Coastal Environment - Evolving Plume Structure and Dynamics, *Cont. Shelf Res.*, *14*(9), 1001–1023.

Wunsch, C. (2006), *Discrete Inverse and State Estimation Problems With Geophysical Fluid Applications*, 371 pp., Cambridge Univ. Press, Cambridge, U.K.

Wunsch, C., and P. Heimbach (2007), Practical global oceanic state estimation, *Phys. D*, *230*, 197–208, doi:10.1016/j.physd.2006.09.040.